Lawrence Berkeley Laboratory
UNIVERSITY OF CALIFORNIA

Materials & Molecular Research Division

IMPROVED BETA"-ALUMINA ELECTROLYTES FOR
ADVANCED STORAGE BATTERIES
Final Report

L.C. De Jonghe

December 1983

Prepared for the U.S. Department of Energy under Contract DE-AC03-76SF00098

DISCLAIMER

IMPROVED BETA"-ALUMINA ELECTROLYTES FOR ADVANCED STORAGE BATTERIES

FINAL REPORT - DECEMBER 1983.

Prepared by

Lutgard C. De Jonghe
Principal Investigator

Materials and Molecular Research Division
Lawrence Berkeley Laobratorty
University of California
Berkeley, CA 94720

This work was supported by the Electric Power Research Institute under contract RP 252-3, and by the Assistant Secretary for Conservation and Renewables, Office of Advanced Conservation Department of Energy under contract No DE-AC03-76SF00098.

ABSTRACT

The investigations seek to clarify the origin of electrolytic degradation of sodium-beta" alumina solid electrolytes when used in sodium/sulfur cells. Degradation is often observed on the sulfur as well as on the sodium side of the used electrolytes, although for some extensively used electrolytes no signs of any degradation could be detected.

In most cases, large grains could be found to be associated with the initiation of Mode I failure, and controlled experiments showed that grain boundaries of such large grains were mechanically weak. Additionally, acoustic emission monitoring during current flow indicated that Mode I cracking could also progress by slow crack growth. This slow, subcritical crack growth is most important in the very early stages of growth of small cracks.

Acoustic emission experiments on electrolytes toughened with a zirconia dispersion indicated that significant increases could be obtained in the threshold current densities at which Mode I degradation initiated.

CONTENTS

ILLUSTRATIONS

Section 1

INTRODUCTION

BACKGROUND AND OBJECTIVES

Sodium-beta" alumina solid electrolytes, for a number of years, have been successfully used as ion selective membranes in advanced sodium-sulfur storage batteries. The life-times of the batteries are such that commercialization in the near future can be contemplated seriously. There remains, however, some problem in the statistical distribution of failure times. A variety of factors can adversely affect the battery performance and lead to premature termination of the cells. Typically, termination of a cell involves a seal failure, an unacceptable rise in cell resistance, or catastrophic fracture of the solid electrolyte. The work discussed in this report aims at clarifying the factors that may contribute to shortening the useful electrolyte life.

Two types of ceramic electrolyte failure may occur. The first type involves a rapid, catastrophic crack propagation. This type of failure, Mode I (1-4), is due to the pressure caused by the flow of sodium through a small, capillary pre-existing surface flaw. One of the objectives of the present work is to identify which microstructural features may act as initiation sites for Mode I failure. This type of failure has been studied by several authors, and, while there remain some minor differences on the details of the modeling, there is agreement that the critical current density for failure initiation is proportional to the critical stress intensity factor, a materials property that expresses how difficult it is to propagate a crack, raised to some power. According to the models, this power has a value of 4(4), so that the fracture

toughness of the electrolyte has a very profound effect on its durability. In this contract period some investigations were therefore initiated examining the critical current density thresholds for failure initiation of zirconia dispersion strengthened ceramics.

Evidence was also sought of possible slow crack propagation mechanisms. A range of electrolytes used in prolonged sodium/sulfur cell testing has been carefully examined for microstructural evidence of slow degradation. Impurities in the electrodes can also contribute to unsatisfactory cell performance. The role of impurities such as water, potassium, and calcium was therefore studied by electrochemical mehtods to assess their effect on the electrochemical behavior of the molten sodium/solid electrolyte interface.

Section 2

EXPERIMENTAL

MATERIALS

Electrolytes were prepared by Ceramatec, Inc, Salt Lake City, Utah. The grain sizes of these electrolytes had been controlled through various heat treatment and sintering schedules by Ceramatec. The composition of the electrolytes was: 8.85 wt% Na_2O, 0.75 wt% Li_2O, balance alumina. The electrolytes were either bars, disks, or tubes. The tubes were about 10 cm long, with a diameter of 1.1 cm and a wall thickness of 0.15 cm. The electrolytes were stored inside an argon atmosphere glove box (Vacuum Atmospheres, Los Angeles, California), in which the water and oxygen content was kept below 1 ppm.

The sodium used in the experiments was S-135, Certified ACS, from Fischer Scientific Company, Santa Clara, California.

Single crystals of sodium-beta alumina used here originated from Union Carbide, Linde Division, San Diego, California. These crytals were prepared some time ago by a Csochralski method, and frequently exhibited cleavage cracks. Most of these cracks could be healed by annealing the crystals at 1500°C in air, packed in protective coarse powder in a closed alumina crucible.

ACOUSTIC EMISSION DETECTION

Initiation or propagation of cracks through a solid is accompanied by the emission of stress waves. Such acoustic emissions can be detected by sensitive transducers

coupled to the specimen via acoustic wave guides. Electronic machinery then can record various signal characteristics such as peak amplitude, rise time, number of ring-down counts, or duration of the acoustic event. An AET 5000 system, manufactured by Acoustic Emission Technology, Sacramento, California, was used to monitor the acoustic activity of the electrolytes during current passage. Careful elimination of electrical and mechanical noise interference was necessary to avoid the counting of spurious acoustic events. The method looses its usefulness in situations where the sensor cannot be coupled directly to the sample, or where noise, such as from rubbing current leads or volume changes of electrodes, cannot be totally eliminated.

SODIUM/SODIUM CELLS FOR ACOUSTIC EMISSION STUDIES

Sodium/sodium cells for the acoustic emission studies were designed to be used in the glove box. Disk shaped specimens of electrolyte were joined to the bottom of open ended alumina tubes (AD998, Coors Porcelain Co., Golden, Colorado), with a sealing glass (SBW glass, Schott America, New York, NY). The cells were heated in the furnace, as shown in Fig. 1 to 350°C for 30 minutes to promote wetting of the electrolyte by the molten sodium. Then, the furnace was adjusted to the desired operating temperature. A Mo rod was inserted in the cell, initially making contact with the electrolyte. Na was then plated onto this electrode at very low current densities. Forming of the working electrode in this manner insured good wetting, and since most impurities are unable to pass through the electrolyte, contamination was prevented. Oxygen contamination could, however, not be excluded from the working electrode since the molten sodium was exposed to the glove box atmosphere. The sodium in the working electrode thus is to be considered saturated with oxygen (about 300 ppm at 300°C). The low current density working electrode plating procedure was monitored with the acoustic emission detection system, as described above, to ascertain that no electrolyte degradation initiation occured during the cell filling stage.

INTERFACE RESISTANCE MEASUREMENTS

Electrolyte/sodium interface resistance could be measured using a smaller alumina tube sealed to the electrolyte disk beside the other alumina tube. This second tube contained a molybdenum wire, and Na was plated onto the wire to form a reversible reference electrode. Because Na is the only mobile species, no concentration gradient will exist in beta" alumina. Therefore the only overpotentials present will be due to the resistances of the electrolyte bulk and surface.

The cell and a 1 ohm standard resistor were connected in series to a sine wave generator, General Radio type 1311-A. A digital voltmeter, Data Precision 3500, was used to measure the potential of the reference electrode, and it was also used to measure the current by measuring the voltage drop across the resistor. The ratio of reference electrode potential to current was constant for frequencies from 25 to 200 hz. Then the sine wave generator was replaced with a galvanostat, Princeton Applied Research model 371, and the reference electrode potential was measured as a function of current for direct current. The potential for alternating current was assumed to be due only to the bulk resistance, so the potential due to the electrode interface resistance was obtained by subtracting the reference electrode potential for an alternating current from that for a direct current of the same magnitude. Then the slope of a plot of potential vs. current gave the electrode interface resistance.

SODIUM/SODIUM CELLS FOR ELECTROCHEMICAL MEASUREMENTS

For the electrochemical measurements of impurity effects, a sodium/sodium cell was designed to operate outside the glove box The body of the cell was stainless steel. The cell is a classical three electrode electrochemical set-up with a working, a reference, and a counter electrode (5). The working electrode (WE) is a nickel rod. A nickel wire is attached at the end of this rod and wound in a spring-like fashion to ensure direct electrical contact with the electrolyte tube

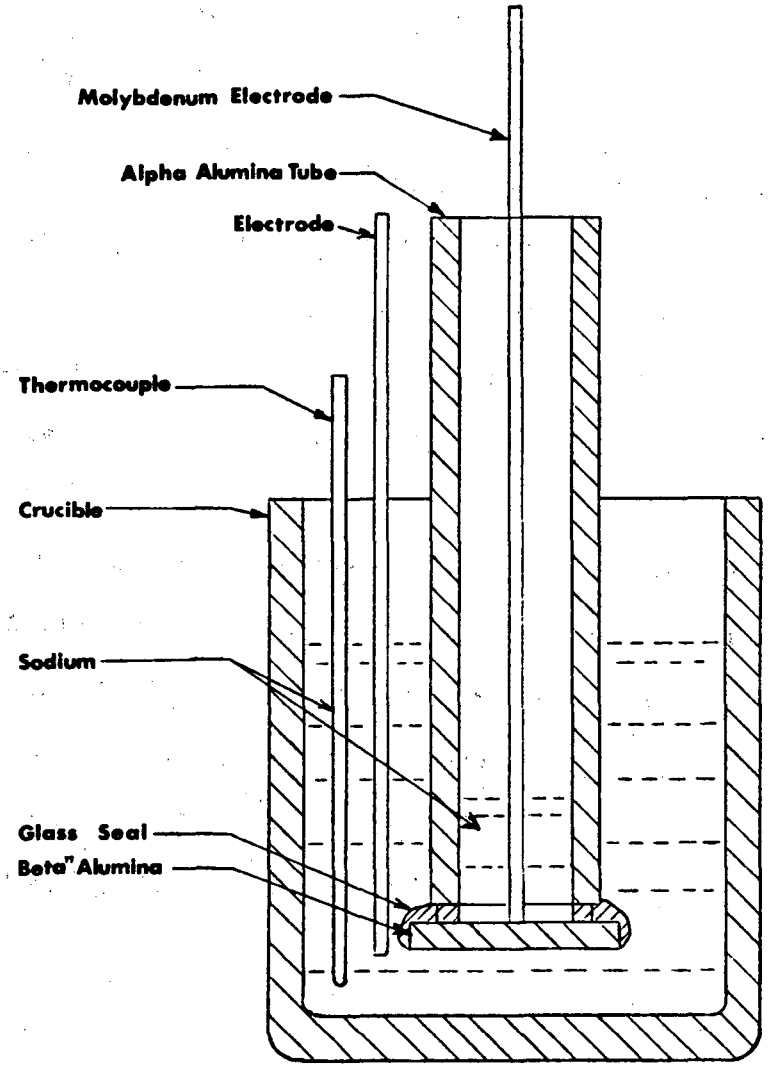

Figure 1. Sodium/Sodium Cell for Acoustic Emission Studies

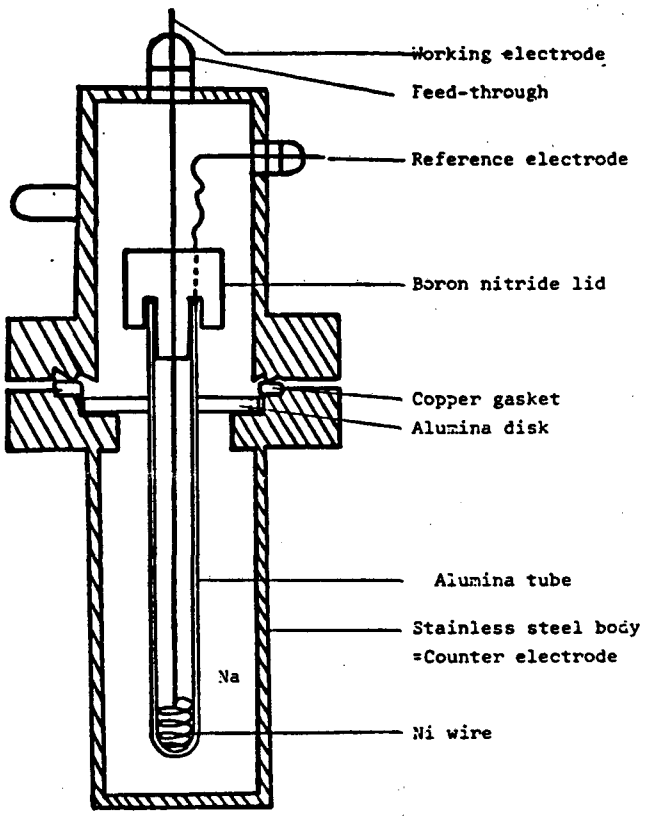

Figure 2. Sodium/Sodium Cell for Electrochemical Measurements

test. The design is shown in Fig. 2. The reference electrode (RE) is a thin nickel wire passing through a boron nitride lid and contacting the top of the electrolyte tube. The wire is sufficiently flexible so that the boron nitride lid is outside of the upper part of the cell during assembly, and slides along the nickel rod into position when the cell is closed. The counter electrode (CE) is the stainless steel body of the cell. The electrolyte tube is attached to an alumina collar with sealing glass.

The electrical connections for the RE and the WE are glass/kovar feedthroughs that are resistant to sodium attack. The cell is assembled in the glove box, with the cell kept at about 150°C to keep the sodium molten. Sodium is melted in the lower cell compartment that will constitute the CE. The electrolyte tube is then inserted into the lower cell part and the upper cell part is tightened onto the

lower part. After the nuts have been tightened the cell is removed from the glove box and the experiments are carried out in a box furnace in air. Cell testing experiments were carried out between 160 and 350° C.

At the start of the experiments the electrolyte tube is filled electrolytically with about 1.5 cm^3 of sodium. Some current is also drawn through the reference electrode to build up a small droplet of sodium there that will constitute the RE.

For electrochemical tests involving impurities, the impurity in question would be added inside the tube during cell assembly. Cell are disassembled hot in the glovebox after completion of the electrochemical tests.

ELECTROCHEMICAL MEASUREMENT METHODS

Current versus voltage curves can characterize the electrochemical behaviour of the electrode/electrolyte interface--in our case molten (Na^+/B"Al_2O_3. Deviations from ohmic behaviour indicates that one or several steps of the interface process (es) are kinetically limited, for example diffusion limitation of the electroactive species transported from the bulk to the interface. This gives rise to overvoltages or so-called interface polarization (6).

In all electrochemical measurements a difference of potential is imposed (respectively measured) in between the reference electrode (RE) and the working electrode (WE), and the corresponding current flowing between the (WE) and the counter electrode (CE) is measured (respectively, imposed). Three electrodes are needed because only a difference of potential can be measured and therefore a constant stable potential is necessary as a "reference potential". The potential of the (CE) is not suitable for a reference since current is flowing through it and an overvoltage may be generated if the (CE) interface is non-Ohmic. The (RE) is in our case the droplet of Na at the top of the tube. This (RE) is connected

to an electrometer of high impedance so that very little current is actually flowing in between the (WE) and the (RE).

The main purpose of the (RE) is to allow a differentiation between the two Na/B"Al_2O_3 interfaces, inside and outside the tube. The potential of the (WE) is monitored with respect to a (RE), and the potential of this (WE) is directly dependent on the sodium activity. The resistance which appears on the graph I/E is compossed of the (WE) interface resistance Na/B"Al_2O_3 and part of the bulk resistance of the electrolyte.

If the inside of the tube is then contaminated with one specific impurity, its effect on the interface process is investigated without any interference of the counter electrode side, and any non-Ohmic behavior may then be related to this specific impurity.

A substantial improvement in the sensitivity of the measurements was obtained with a four-point probe method: two probes measure the potential and two probes (current leads) carry and measure the current. The additional potential prohbe is a nickel wire welded directly onto the working electrode. This method eliminated possible contact resistances in external current or voltage connections due to oxidation of the contacts.

The deviations from purely ohmic behaviour were small in most cases. an electronic device was therefore included in the measurement circuit suppressing the ohmic part of the current so that in some cases the non-ohmic part could be separately amplified.

Section 3

EXPERIMENTAL RESULTS

EXAMINATION OF USED ELECTROLYTES: Na/S CELLS

Sulfur-side degradation

BBC

Electrolytes from Brown Boveri had a composition of 8.9wt% Na_2O, 2.25 wt% MgO, balance alumina, and were cycled at 350°C with current densities of 150 mA/cm^2 during discharge and 75 mA/cm^2 during charge. Figs. 3-6 are polished and stained cross sections of electrolytes used in Na/S cells for a one-way total charge transfer of 100 or 310 Ah/cm^2. In these electrolytes evidence of any sodium side degradation was absent, Fig. 3, although the 100 Ah/cm^2 cell was reported to have failed. Presumably the failure was not due to the electrolyte. For the lower charge transfers, no degradation at the sulfur side was in evidence either. However, at the longer times, after 310 Ah/cm^2, some evidence of sulfur side degradation is present, as shown in Fig. 5. Occasionally large grains can be found in these electrolytes. The degradation is consistently observed at the boundaries of such large grains as seen in Fig. 6, strongly suggesting that the sulfur side attack is of an intergranular nature. A crack forming on the sulfur side was found in electrolyte 3178 Fig. 7, although this cell had been cycled to 270 Ah/cm^2 without failure.

GE

Two types of electrolyte from the General Electric program were examined. The new material, RS-1, has lower resistance and reportedly showed less of an in-cell resistance rise than the older G8 electrolytes. GE cell B814L, made from RS-1 beta"-alumina, has been cycled for 759 Ah/cm^2, and the optical micrograph, fig. 8,

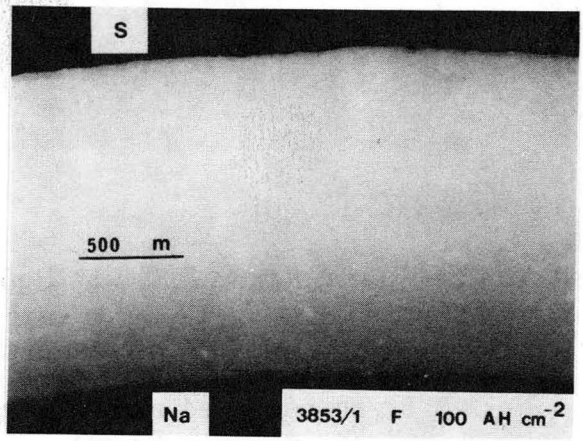

Figure 3. Polished and Stained Cross Section Of Cell 3853

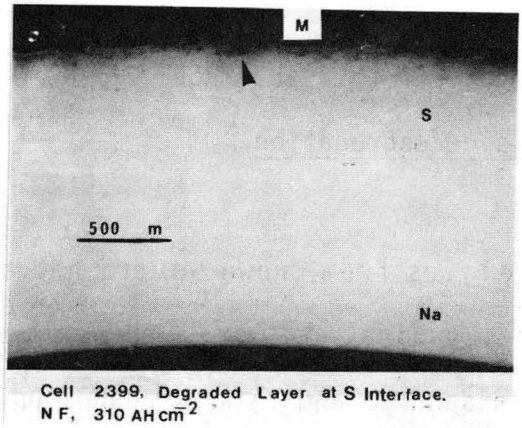

Figure 4. Polished and Stained Cross Section Of Cell 2399

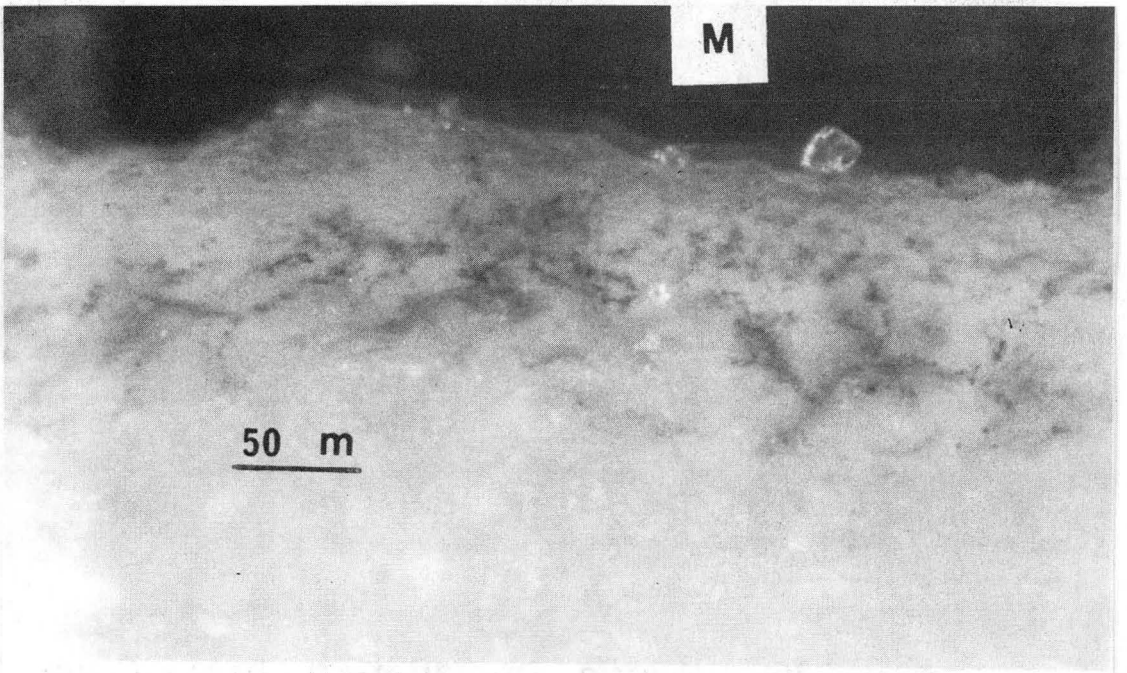

Cell 2399, S side Degradation
NF, 310 AH cm^{-2}

Figure 5. Polished and Stained Cross Section Showing Sulfur-Side Degradation, Cell 2399

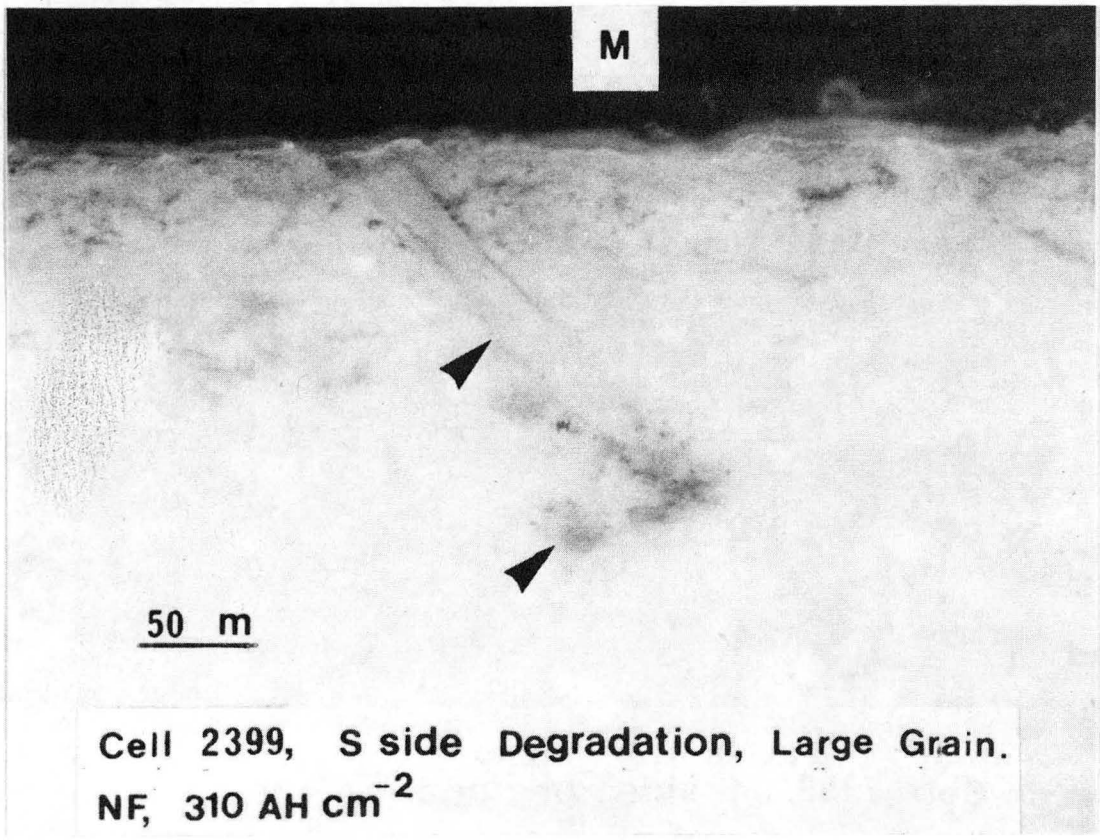

Figure 6. Polished and Stained Cross Section Showing Sulfur-Side Degradation Involving a Large Grain In Cell 2399

showed some modest attack on the sulfur-side of the electrolyte. In the scanning electron microscope, Fig. 9, a layer with a different microstructure could be observed. This layer had a fairly sharp boundary, as indicated by the arrows in Fig. 9, and appears to have increased porosity. Part of this porosity may be due to pulling out of grains during the polishing operation, where grainboundaries had been weakened by the positive electrode attack. The sharp boundary in Fig. 9 is not clearly a crack, although in the optical microscope it appears as a sharp, darkened line. A similar feature can be observed in the electrolyte in cell A614E, although here the dark line is further away from the sulfur side surface. This feature is shown in Fig. 10 and 11 in optical micrographs, and in Fig. 12 in a scanning electron micrograph. It is thought that these layers may well be the

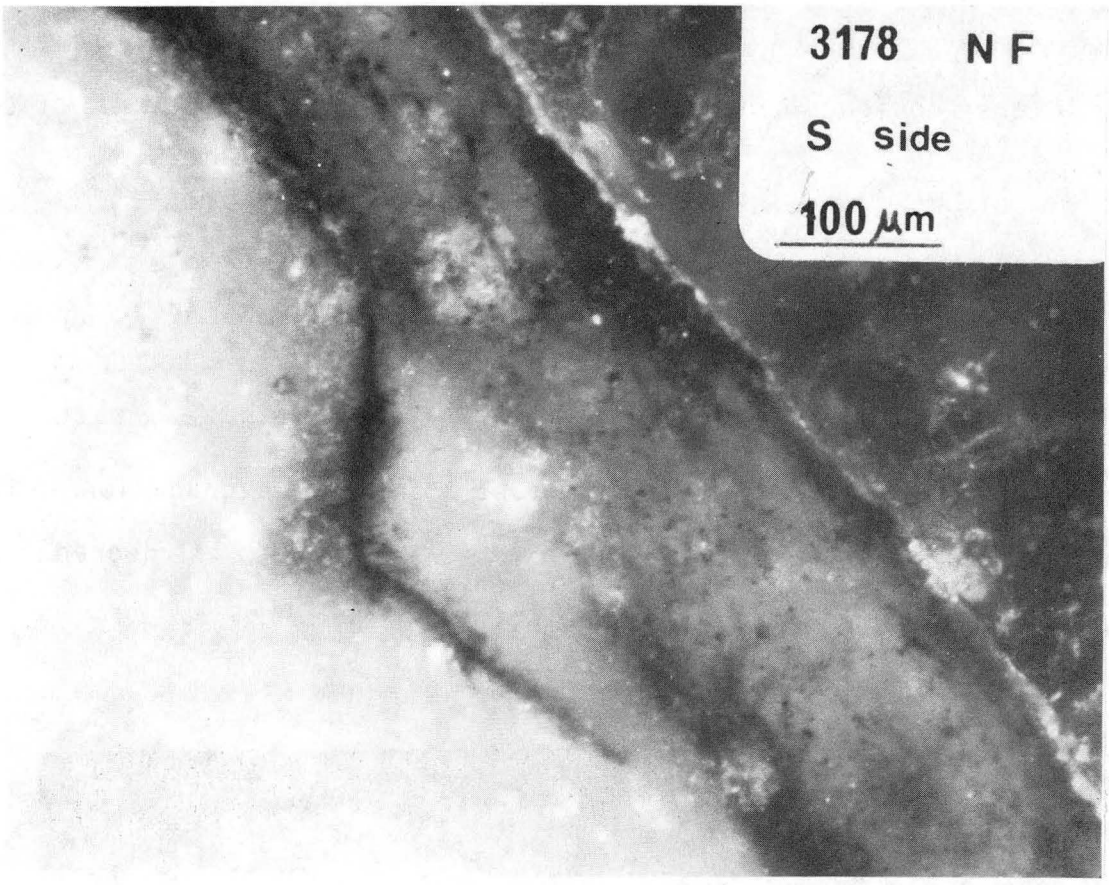

Figure 7. Polished and Stained Cross Secion Showing Sulfur-Side Crack in Cell 3178

result of the electrophoretic tube fabrication method, rather than the direct result of sulfur-side attack. The observations suggest that some minor changes in, e.g., composition such as brought about during certain fabrication steps may underlie the susceptibility of the ceramics to positive electrode attack.

BR

Electrolytes tested some time ago by British Rail had a composition of 8.9 wt% Na_2O, 0.7wt% Li_2O, balance alumina, and were more than 90% beta", with the rest beta alumina. These electrolyte tubes and been fabricated by isostatic pressing and were sintered in closed crucibles of high thermal capacity in an electric kiln. The microstructure of a polished and etched electrolyte is shown in Fig.

13. The grains are tabular and vary in size considerably. These electrolytes were cycled in cells to an average current density of 50 mA/cm^2, with current densities occasionally as high as 100mA/cm^2, in some discharge cycles. The cells were of the inverse design, where the sulfur electrode is on the inside of the electrolyte tube.

Fig. 14 is an optical micrograph showing sulfur side degradation in a British Rail cell cycled for 121 Ah/cm^2. A scanning electron micrograph of this degradation is shown in Fig. 15. It appears as if some intergranular corrosion has occured. In another electrolyte, cycled for 539 Ah/cm^2 more pronounced degradation on the sulfur side was found, Fig. 16. This time cracks were found in the degradation layer, as clearly revealed by the scanning electron micrograph, Fig. 17.

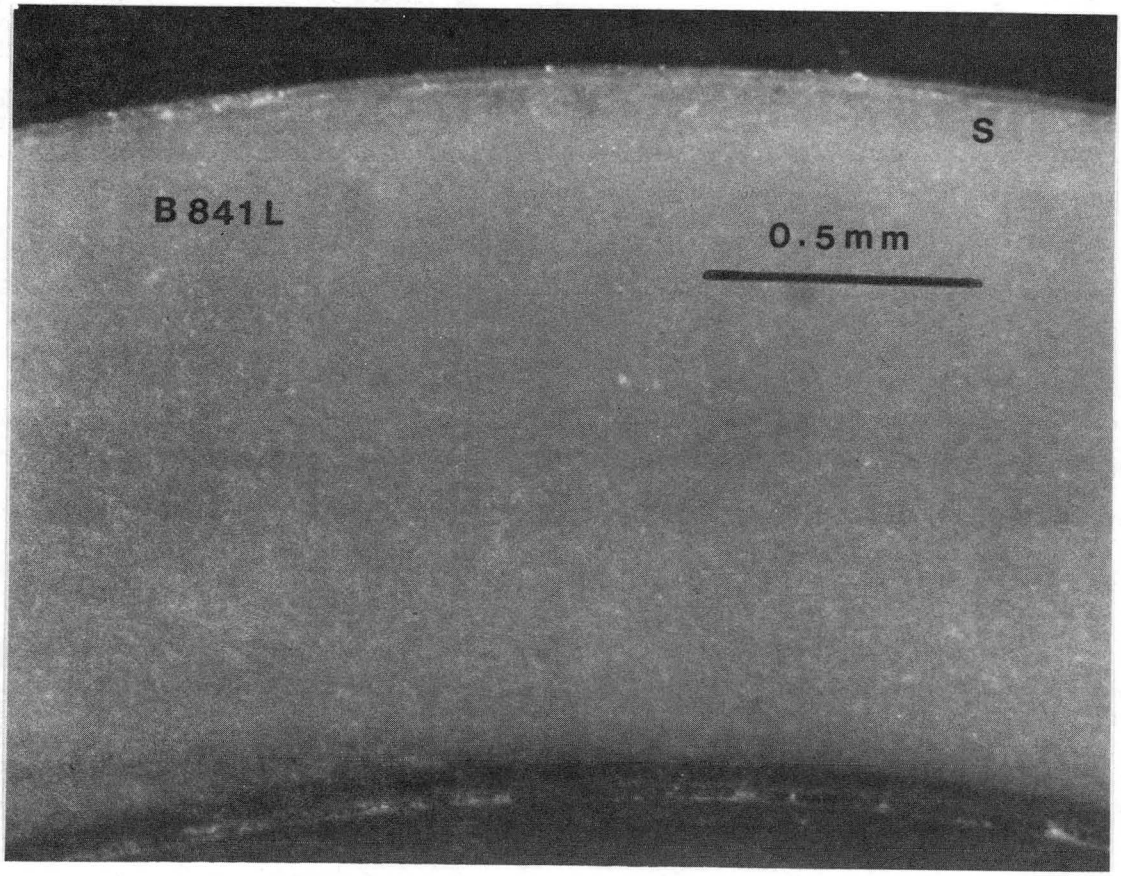

Figure 8. Polished and Stained Cross Section of Cell B814L

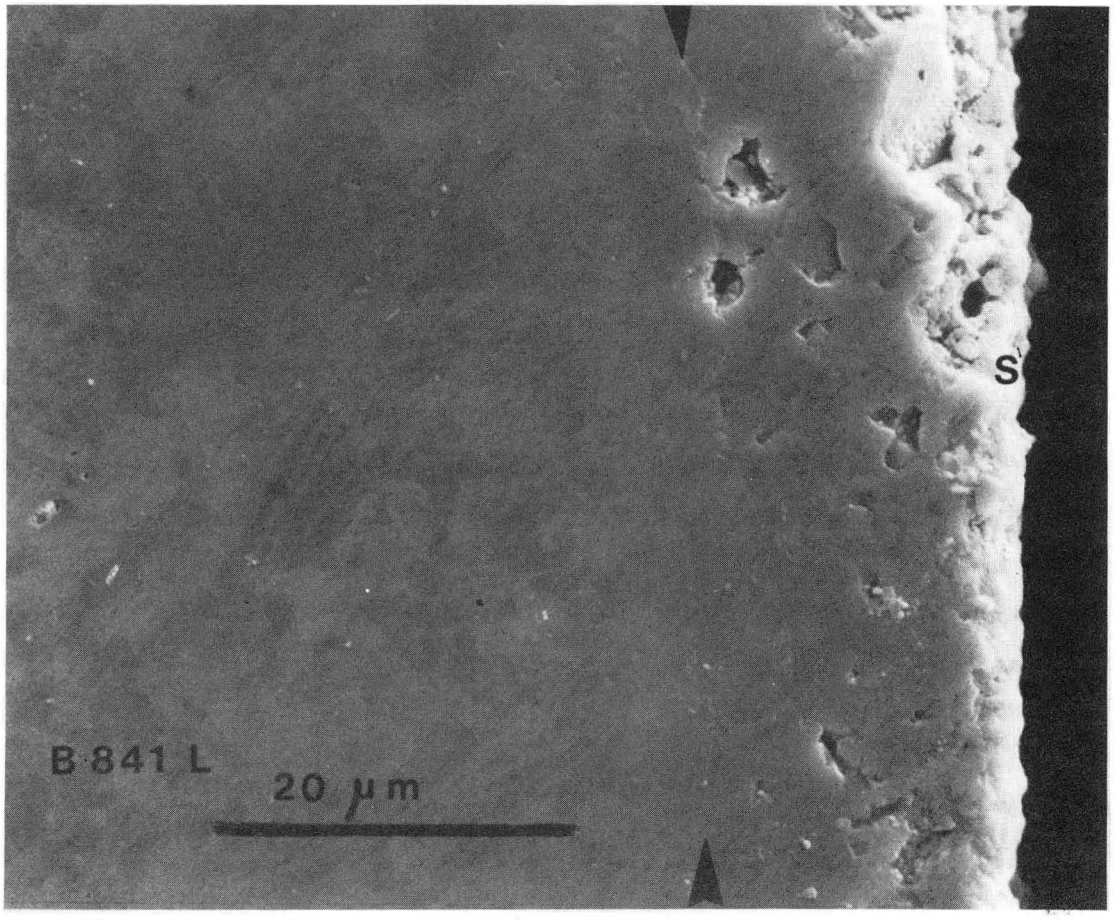

Figure 9. Scanning Electron Micrograph of Layer at Sulfur-Side of Cell B814L

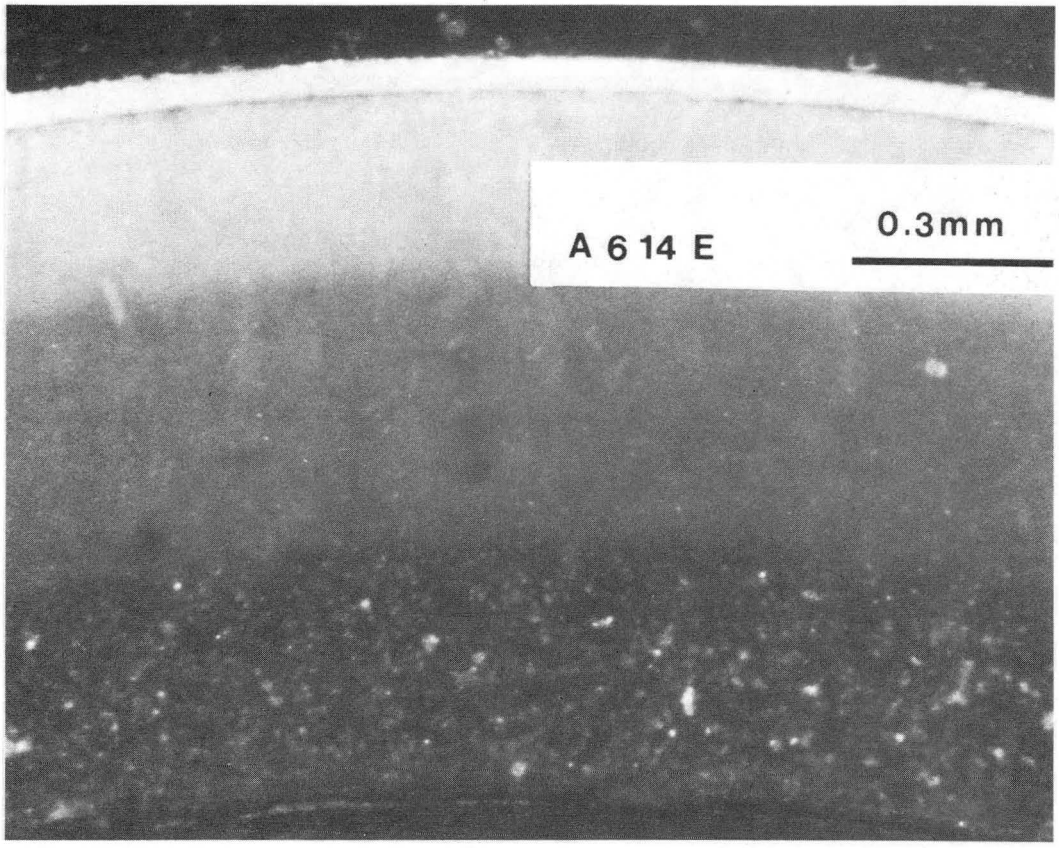

Figure 10. Polished and Stained Cross Section of Cell A614E

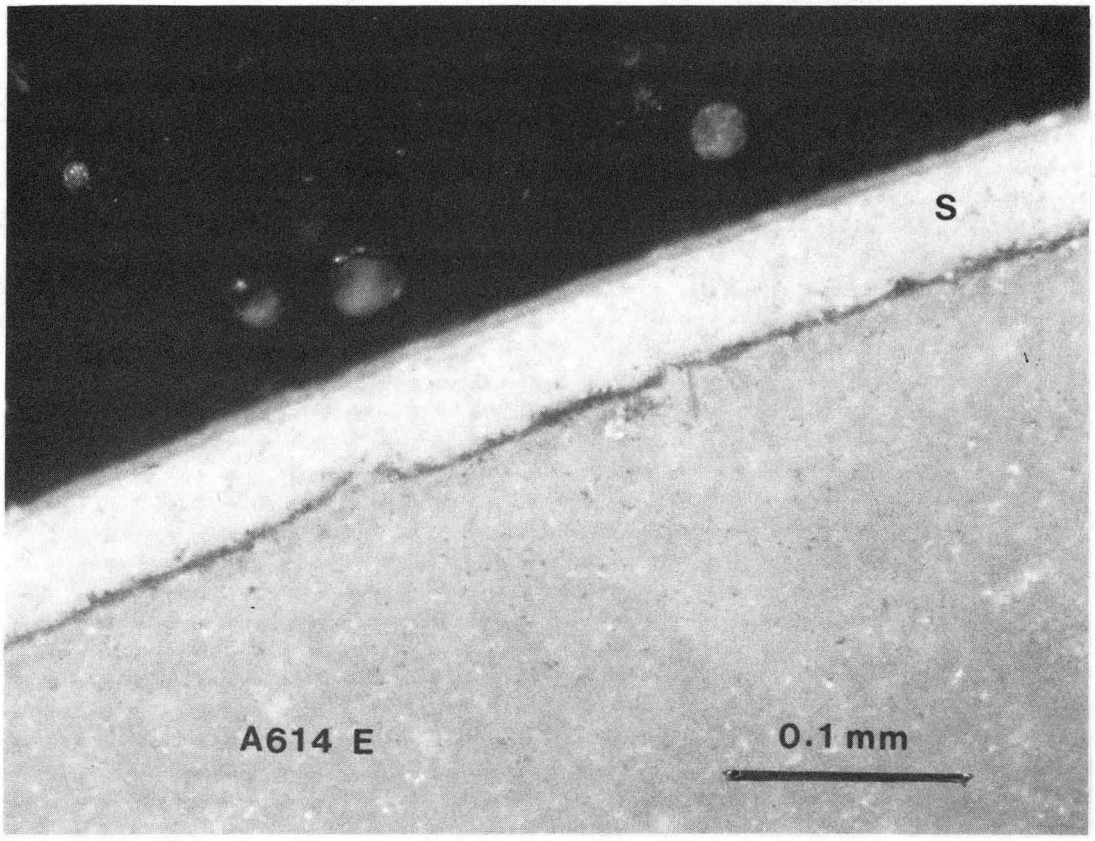

Figure 11. Polished and Stained Cross Section of Sulfur-Side Layer in Cell A614E

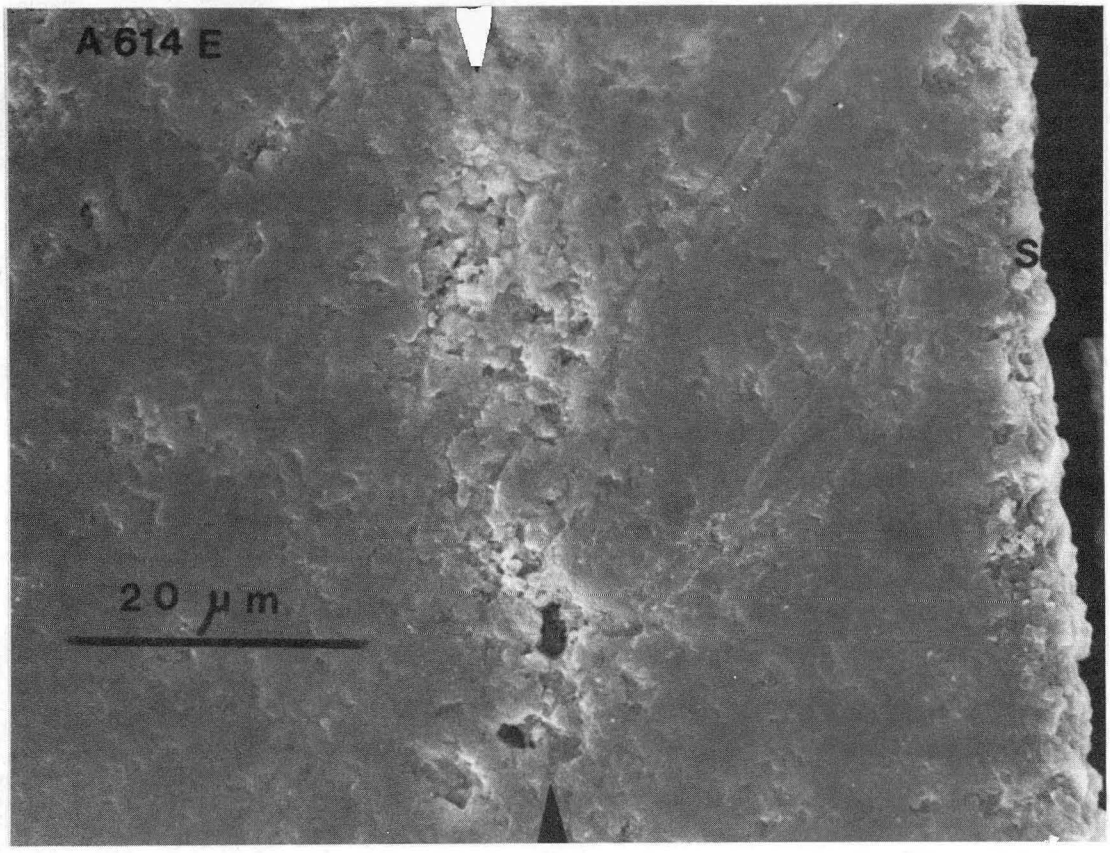

Figure 12. Scanning Electron Micrograph of Layer at Sulfur Side of Cell A614E

Ford

Two used electrolytes from the Ford Program were examined. These electrolytes had been on test for approximately one year, and had accumulated 592 and 602 Ah/cm^2. Fig. 18 shows the sulfur side of the electrolyte in cross section in an optical micrograph. No degradation is in evidence. This is longest cycled electrolyte examined so far in which sulfur side degradation is not in evidence. At somewhat longer cycling times, in cell D602, some sulfur side attack is again present. It is interesting to note that in certain areas this degradation has not occured, as shown in Fig. 19. A higher magnification optical micrograph of a degraded area is shown in Fig. 20. It can again be observed that degradation appears to have taken place preferentially along the grain boundaries of some large grains.

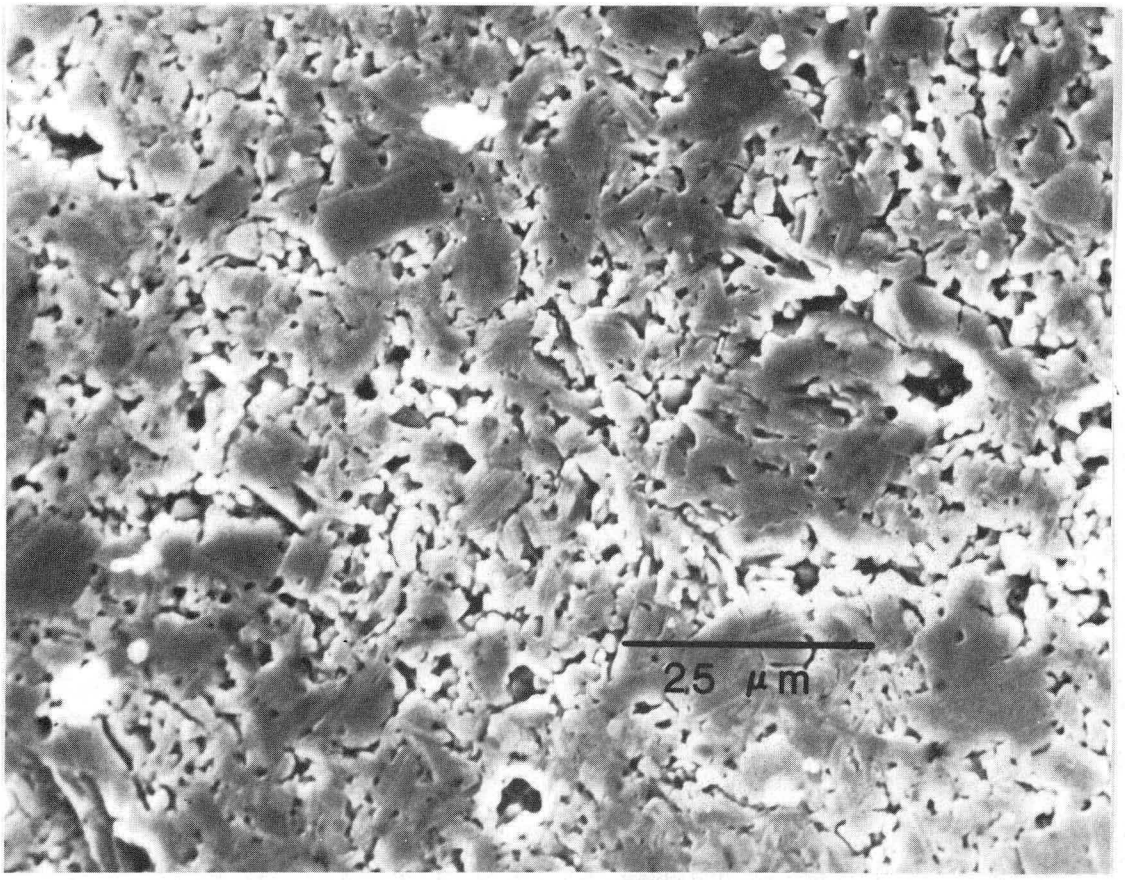

Figure 13. Polished and Etched Cross Section of British Railway Electrolyte

Sodium-side degradation

All electrolytes that have been investigated have a darkened layer at the Na interface that shows clearly after staining with silver nitrate solution. This darkened layer is due to a partial reduction of the electrolyte during exposure to molten Na. Prior to staining the darkening can be removed by heating to 800°C in air; the thickness of the layer is proportional to the square root of the time the material is exposed to Na (7). Prior to staining the layer is light grey, and staining in silver nitrate solution colors it dark brown.

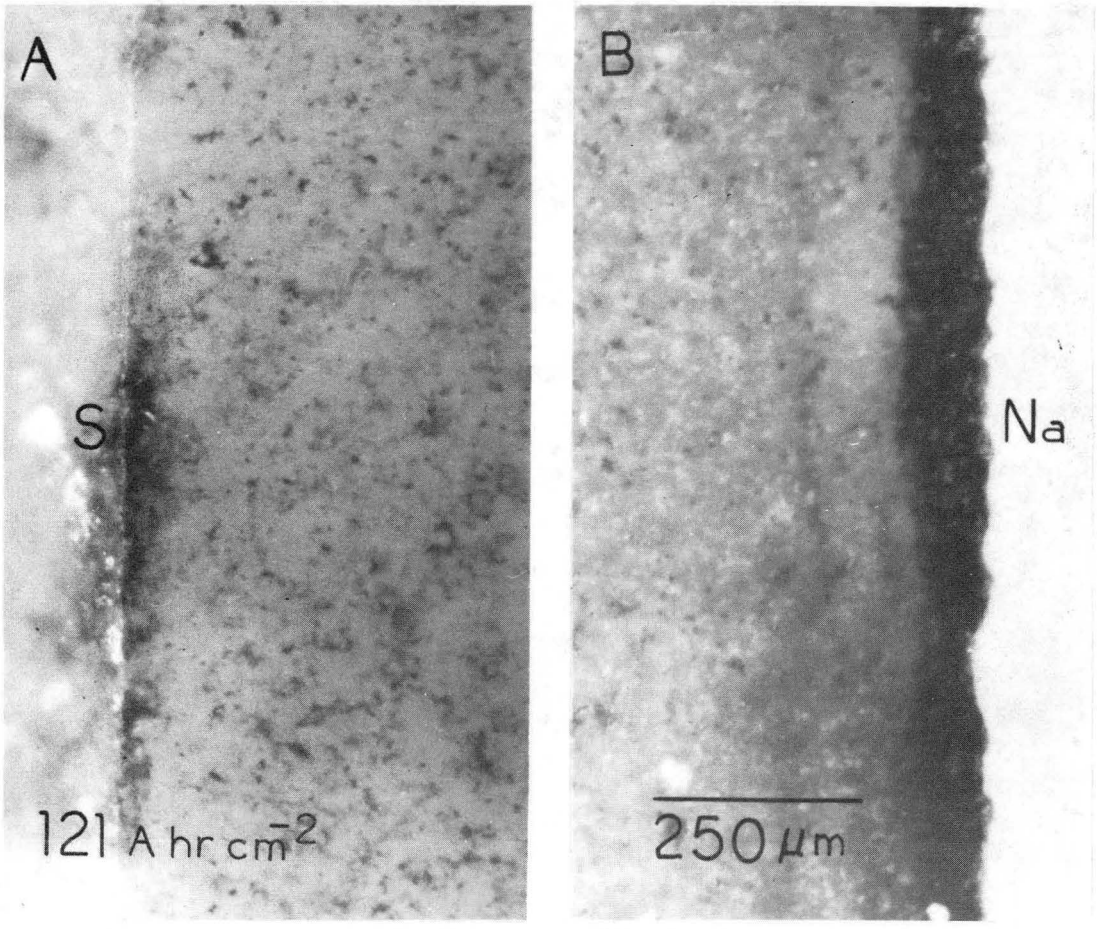

Figure 14. Polished and Stained Cross Section of British Railway Electrolyte Cycled for 121 Ah/cm^2

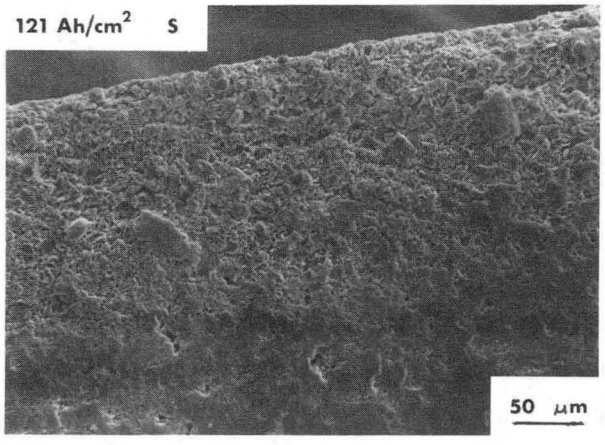

Figure 15. Scanning Electron Micrograph of Sulfur Side of Electrolyte First Shown in Figure 14

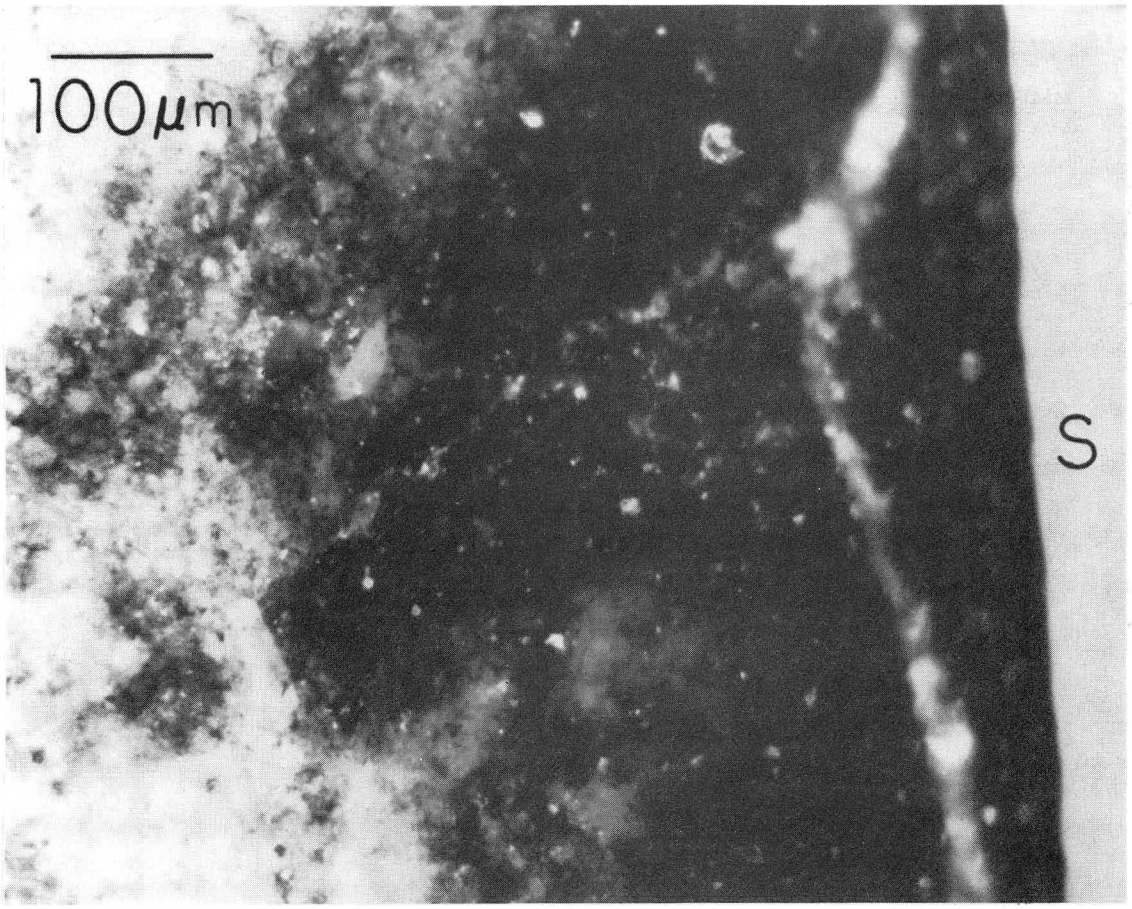

Figure 16. Polished and Stained Cross Section of British Railway Electrolyte Cycled for 539 Ah/cm^2

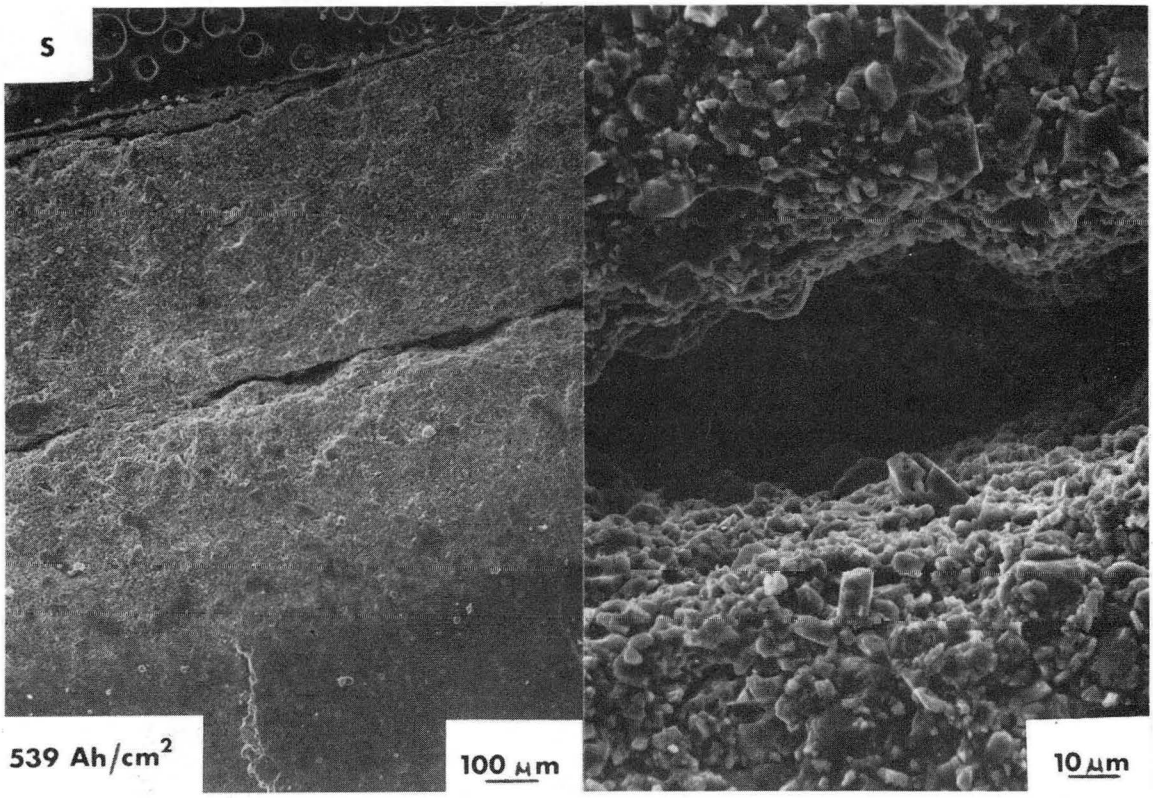

Figure 17. Scanning Electron Micrograph of Electrolyte First Shown in Figure 16

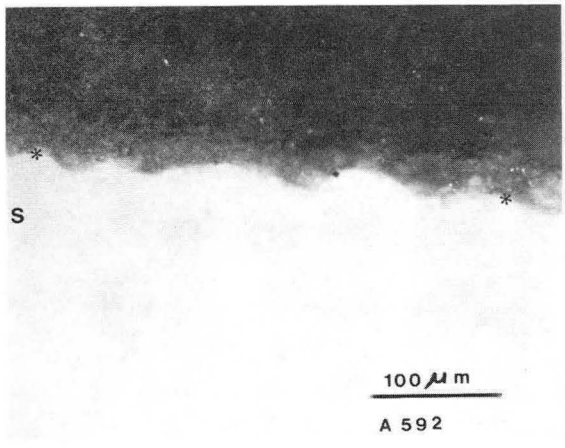

Figure 18. Ford Electrolyte Cycled for 592 Ah/cm² Showing No Degradation

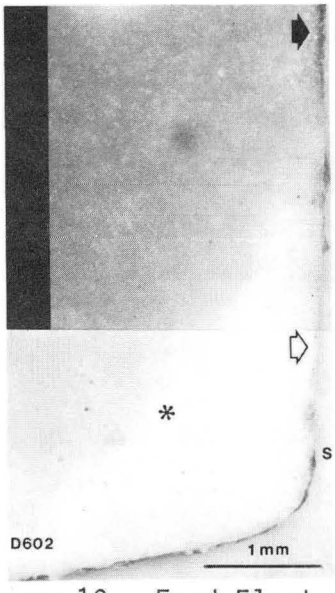

Figure 19. Ford Electrolyte Cycled for 602 Ah/cm² Showing Some Degradation

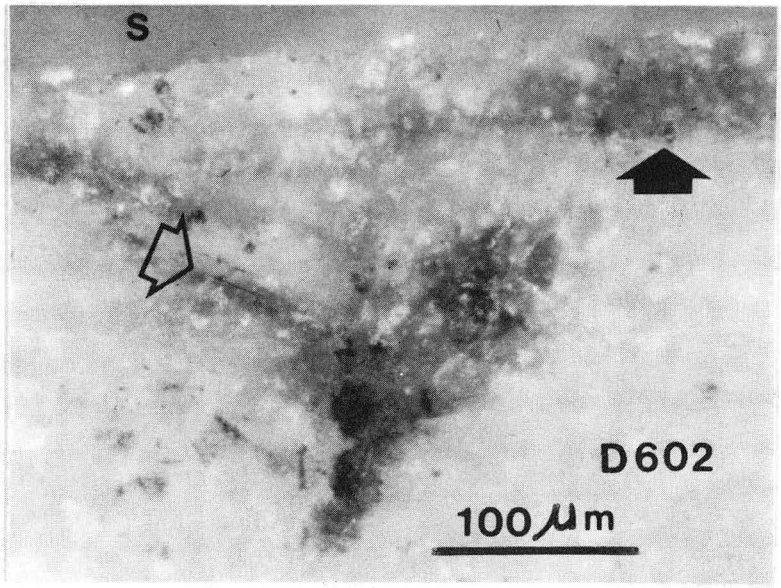

Figure 20. Higher Magnification of Sulfur Side Degradation in Cell First Shown In Figure 19

A second feature appearing in many used electrolytes is a thinner, "extra-darkened" layer at the sodium interface. This layer is not as thick as the darkened layer, and after staining it appears black in the optical microscope. In some cases, careful handling of the specimens is necessary to prevent spalling of this layer, and after polishing on a polishing cloth with diamond paste the layer appears porous due to pull outs. Specimens ground more gently and polished on aluminum or tin with diamond paste reveal in some cases a high density of microcracks at the grain boundaries in this region. During cycling either the grain boundaries may be severely weakened so that they crack during polishing, or microcracks may form in-cell. The usual darkened layer appears in specimens immersed in molten sodium even if no current is passed, but the "extra-dark", layer is only observed after passage of current for extended times. When microcracking is observed, the development of such a surface damage layer can be interpreted as a progressive type degradation that weakens the electrolyte from the sodium side.

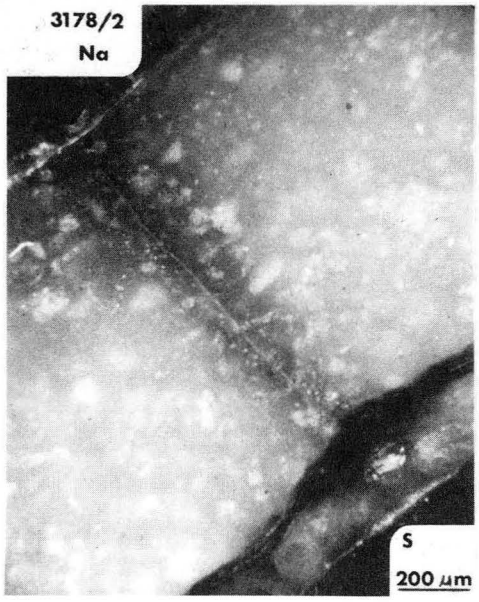

Figure 21. Polished and Stained Cross Section of Cell 3178 Showing a Mode I Crack

BBC

Brown Boveri cells 3853 and 2399 show little evidence of sodium-side degradation, and the only feature evident in Figures 3 and 4 is the usual darkened layer. Figure 21 shows a mode I crack penetrating through cell 3178, which was cycled for 270 Ah/cm^2. The light spots throughout the electrolyte are subsurface cracks. A gradual increase in resistance was reported for cell 3178, but not for the other cells. This group of cells showed little sign of any degraded layer, and were not examined in the SEM.

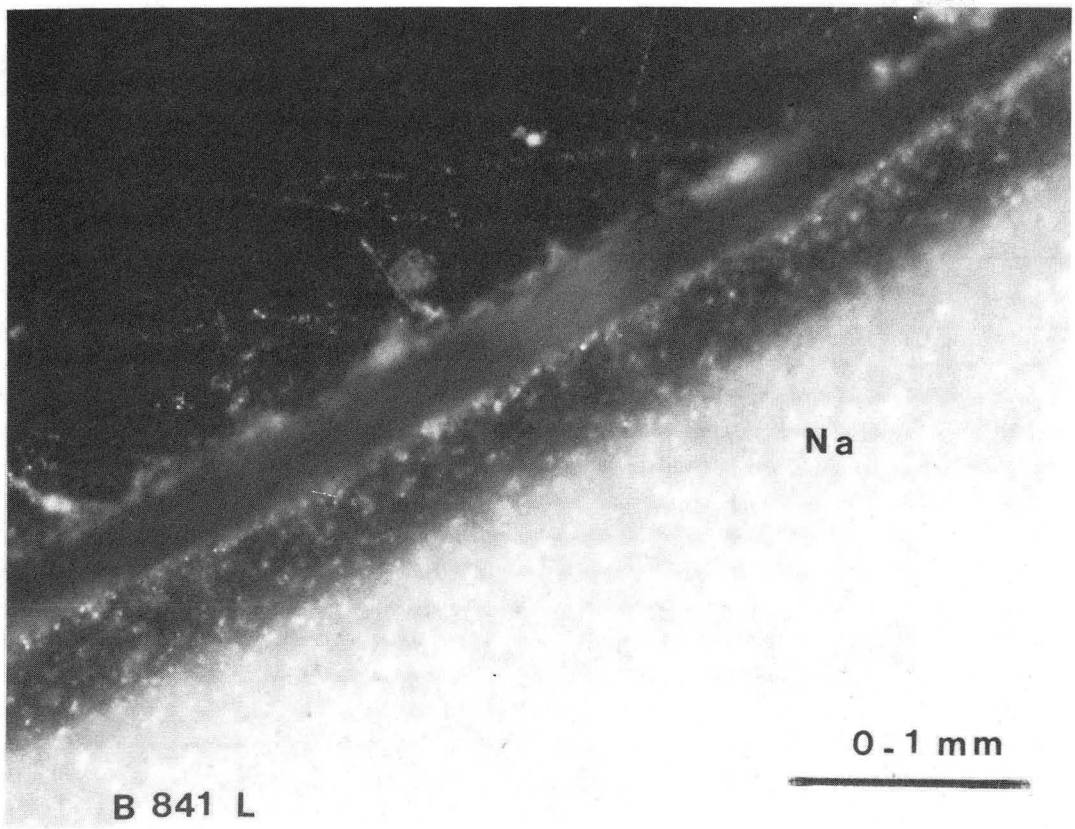

Figure 22. Polished and Stained Cross Section of Sodium Side of Cell B814L Showing "Extra-Darkened" Layer

GE

The General Electric cell B814L, cycled for 759 Ah/cm^2 (one way), is shown in cross section in Fig. 7. The electrolyte appears to be relatively uniformly stained throughout, but shows a thin "extra-darkened" band near the Na surface. Fig. 22. shows this layer more clearly. In this case, SEM did show only slight evidence of some damage in this region, Fig. 23. Also, during sawing of the electrolyte with a diamond blade, electrolytes A614E and B814L seemed mechanically stronger than most other used electrolytes examined so far, suggesting as well that not much degradation had occured.

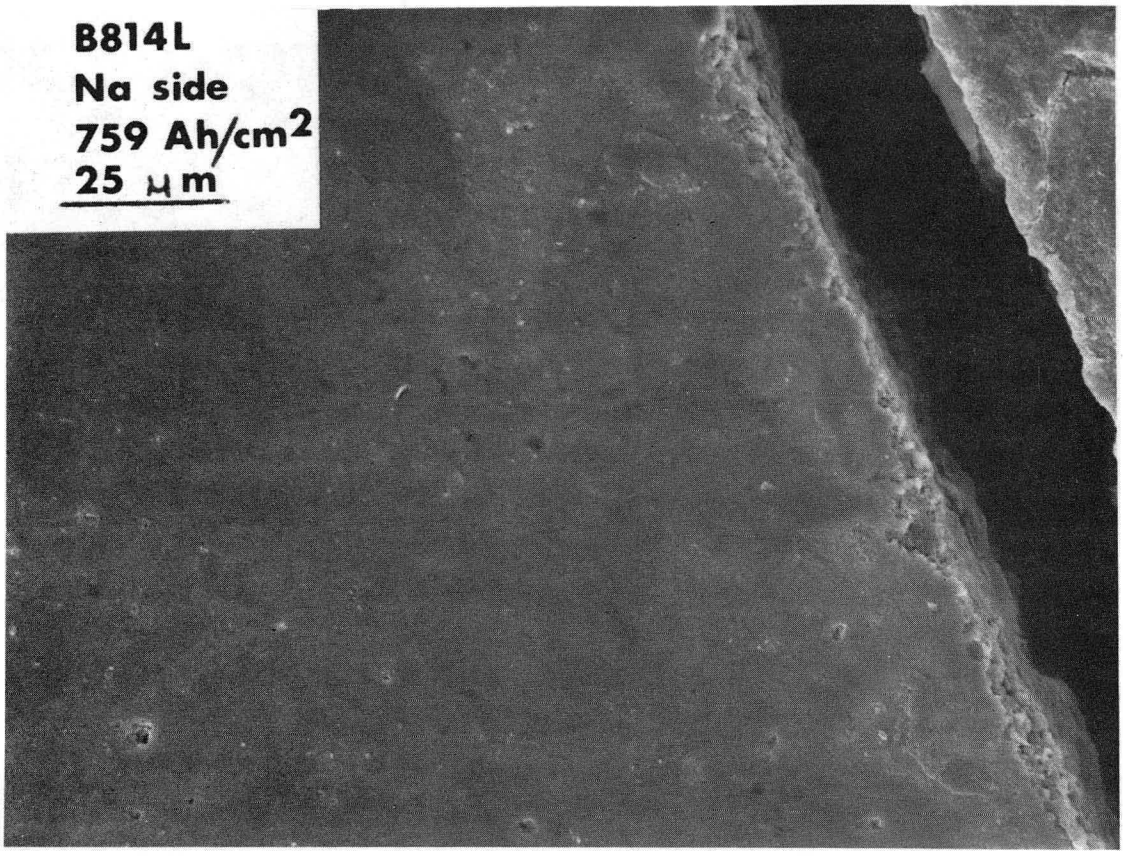

Figure 23. Scanning Electron Micrograph of Sodium Side of Cell B814L Showing Little Damage

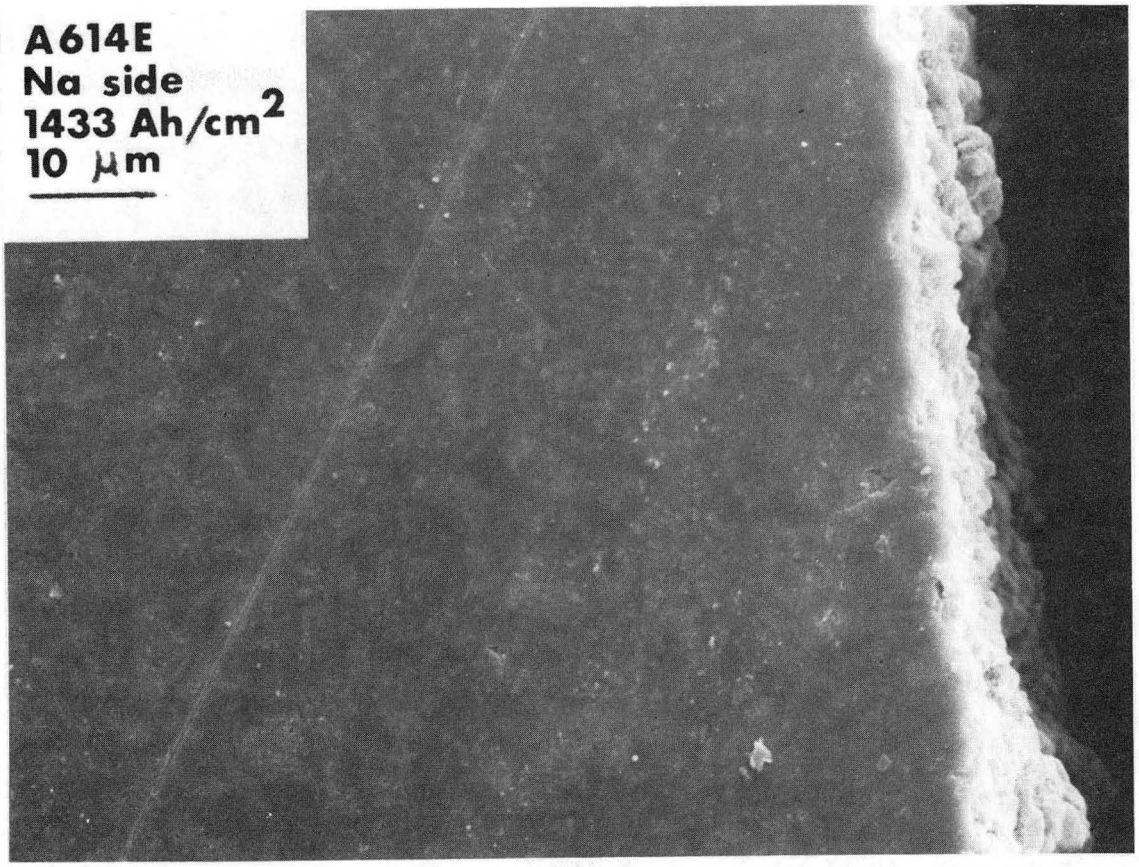

Figure 24. Scanning Electron Micrograph of Sodium Side of Cell A614E Showing Slight Damage

No sign of Mode I cracking was seen in either electrolyte. The optical micrograph of A614E, Figure 10 shows five layers. From the sodium side, first there is a thin blackened layer, and then an extremely dark layer with subsurface cracks, showing up as white spots. Next is a layer which is slightly less dark and shows little sign of any cracks. The next layer appears light in Figure 10, but it is also darkened, as can be seen in Figure 11 compared to the final layer between the sulfur interface and the crack parallel to it. This cell was cycled for 1433 Ah/cm^2. The SEM micrograph of cell A614E, Figure 24, again shows little damage.

BR

The British Railways specimen cycled for 121 Ah/cm^2 has a blackened layer at the sodium interface in Figure 14. Figure 25 shows this blackened layer at higher

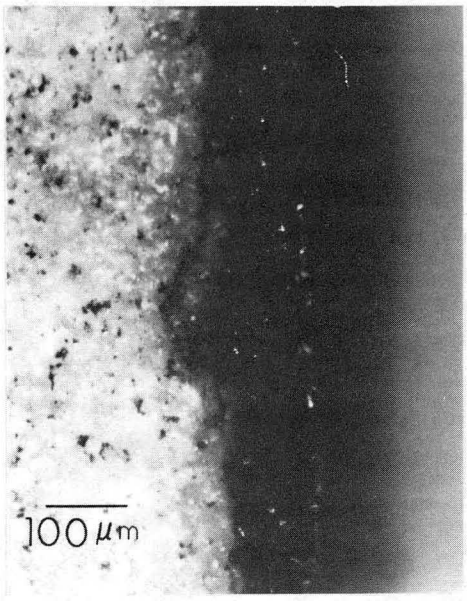

Figure 25. Polished and Stained Cross Section of Sodium Side of Cell First Shown in Figure 14

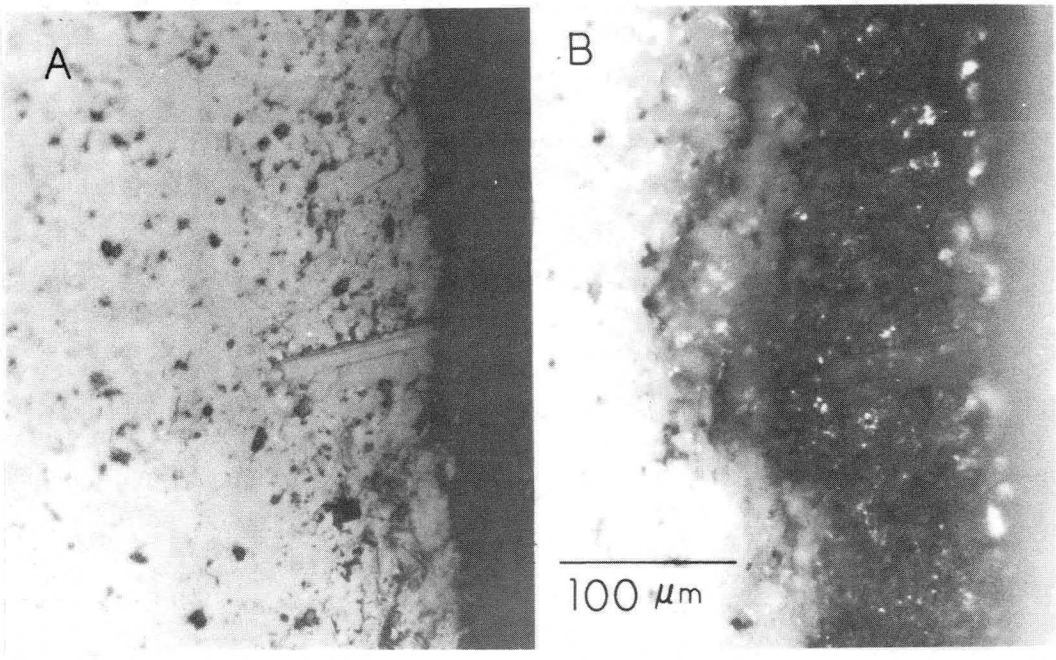

Figure 26. A and B Detail of Sodium Side Degradation of Figure 25
A. Large Grain Visible with Reflected Light
B. Degradation Visible With Polarized Light

magnification, and in a detail of this area, Figure 26, A and B, a region of enhanced degradation is seen to correspond to a large grain at the surface. In Figure 27 degradation proceeds along the boundaries of large grains in another detail of this region. In the SEM, Figure 28 this surface layer has many microcracks at the grain boundaries. Figure 16 shows a crack parallel to the surface by the darkened layer in a specimen tested for 539 Ah/cm^2. A specimen tested to 414 Ah/cm^2 shows a similar crack in Figure 29. Figure 30 shows the blackened region of this electrolyte in greater detail. A crack runs parallel to the interface, and only in a few places does it meet the sodium interface. It does not seem to be a typical mode I crack. An Auger study of the composition near the surface detected almost two atomic per cent calcium, as shown in Figure 31 along with a micrograph of the surface. The crack is again visible in this micrograph. There was also about one percent silicon in this specimen. These impurities, particularly the calcium, create a layer of lower ionic conductivity

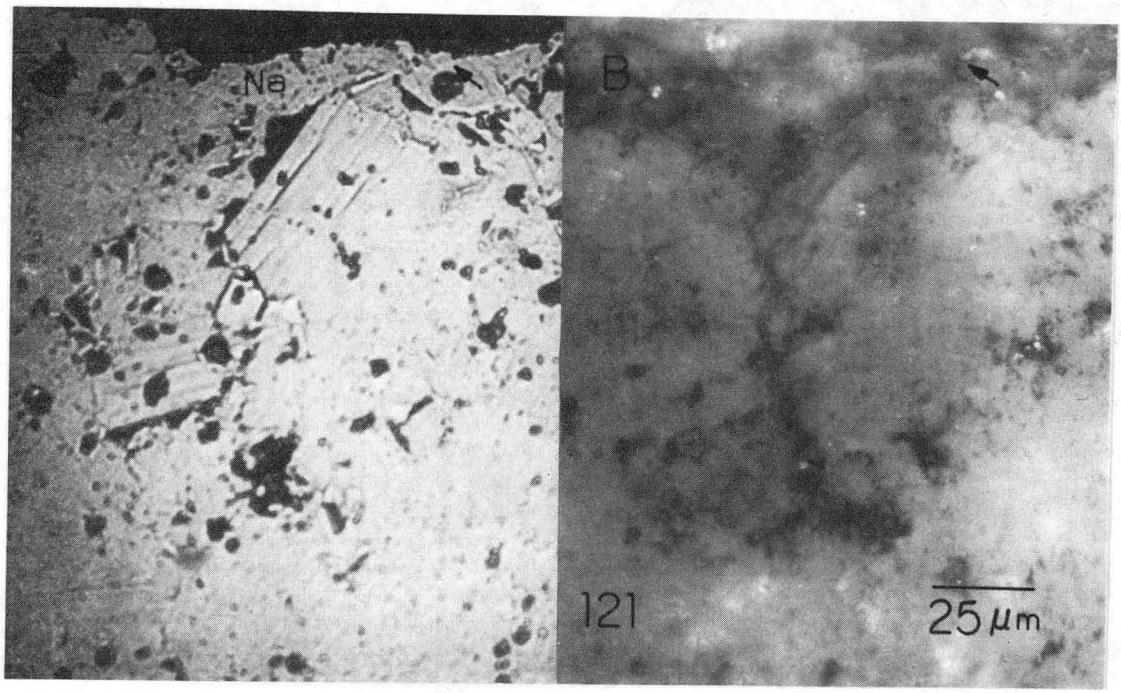

Figure 27. Detail of Sodium Side Degradation in Cell First Shown in Figure 14
A. Large Grains, Normal illumination
B. Cracks Following the Boundaries Of The Large Grains, Polarized Light

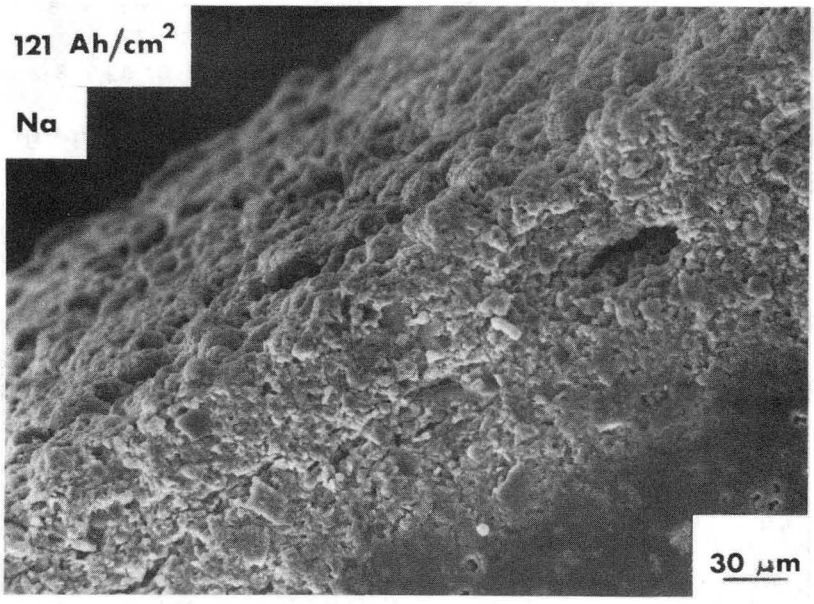

Figure 28. Scanning Electron Micrograph Of Sodium Side Degradation In Cell First Shown In Figure 14

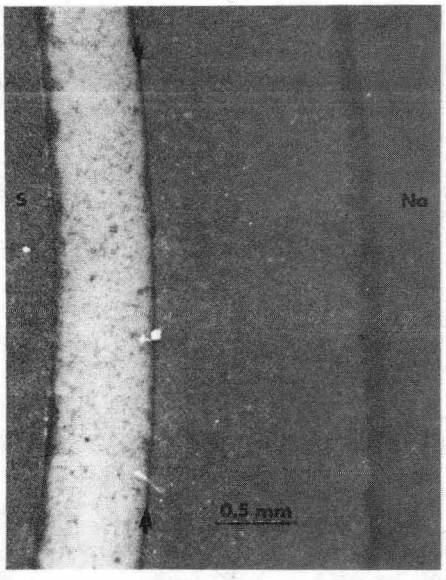

Figure 29. Polished and Stained Cross Section of Specimen Cycled For 414 Ah/cm² With Arrowed Crack Parallel To Interface

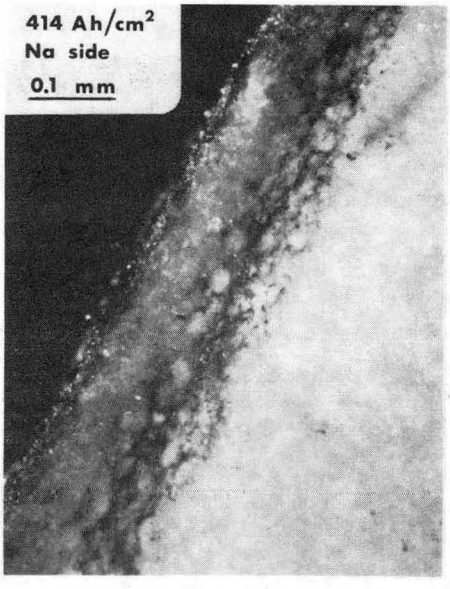

Figure 30. Polished and Stained Cross Section Of Sodium Side Degradation In Electrolyte First Shown In Figure 29

and contribute to mode II degradation as described above. The crack may be related to localized mode II cracking caused by the calcium in the surface of the electrolyte.

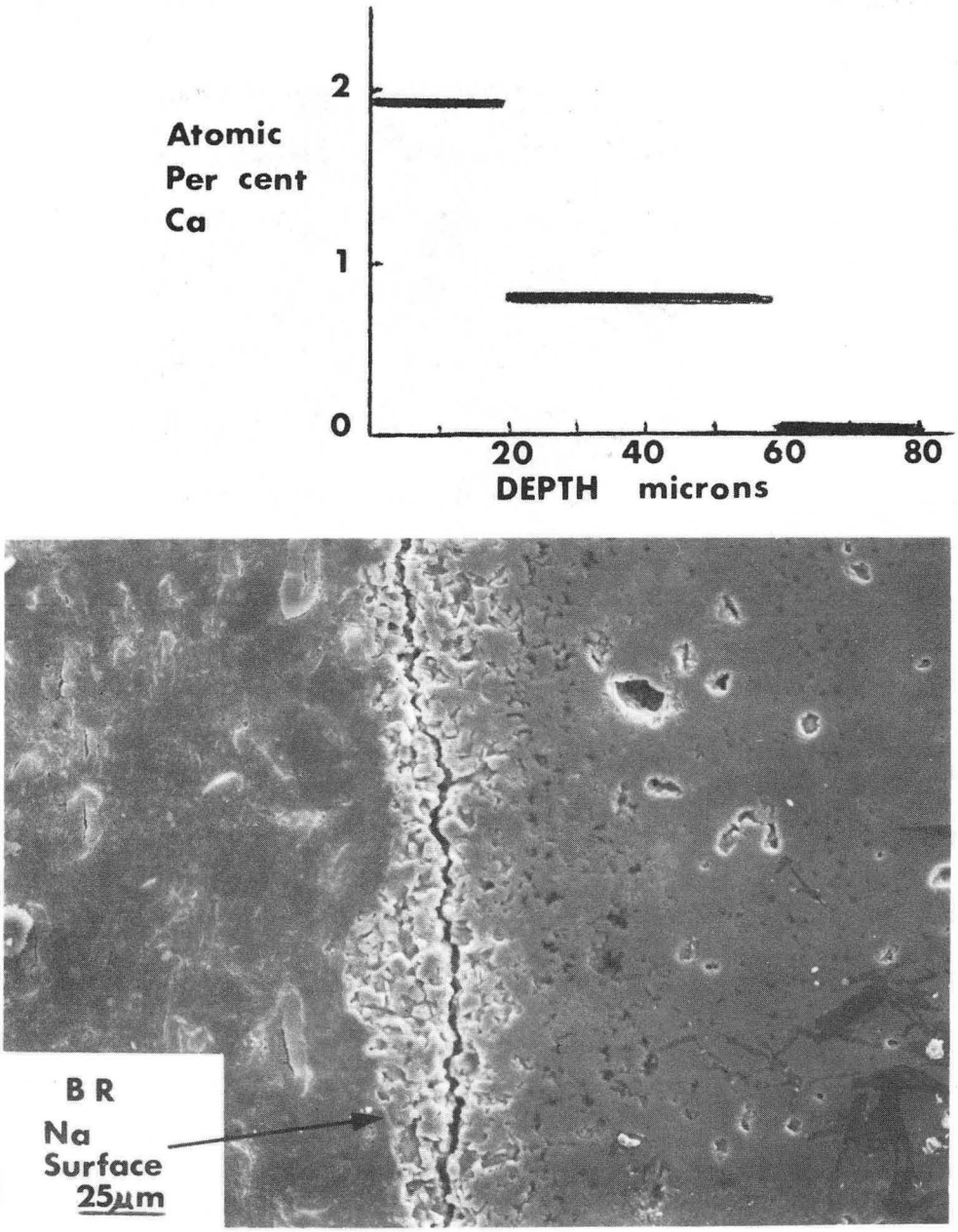

Figure 31. Scanning Electron Micrograph of Na Side Of Electrolyte First Shown In Figure 29 With Crack Parallel To The Interface, And Ca Concentration Near The Surface

Ford

The electrolytes examined from the Ford programs were free of any sign of degradation from the sodium side, even after more than a year on test. The "extra darkened" layer observed in many other used electrolytes, was absent. An example of a polished and stained cross section of used electrolyte is shown in Fig. 32. The asterisks mark the electrolyte surface, where a gap separates it from the mounting material.

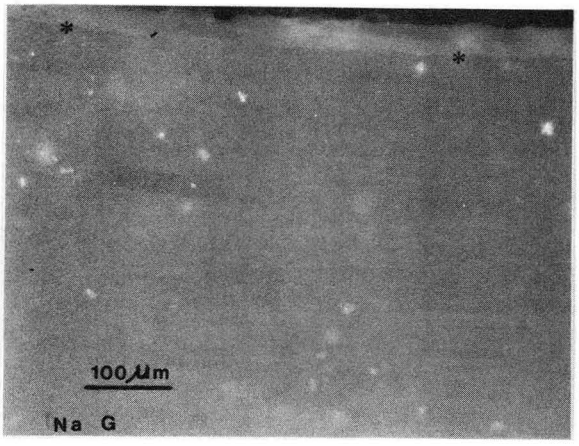

Figure 32. Polished and Stained Cross Section Of Ford Electrolyte. The sodium surface marked with asterisks shows no degradation.

EXAMINATION OF USED ELECTROLYTE:Na/Na CELLS

The features observed in sodium/sodium cells were similar to those on the sodium side of sodium/sulfur cells.

CGE

Cells from Compagnie Generale d' Electricite had been tested for 1,000 hours at 100 mA/cm^2, for a total charge passed of 100 Ah/cm^2. The tubes were operated unidirectionally with the inside as the sodium entrance surface and the outside as the sodium exit surface. Three typical results are shown in Figure 33. The crack

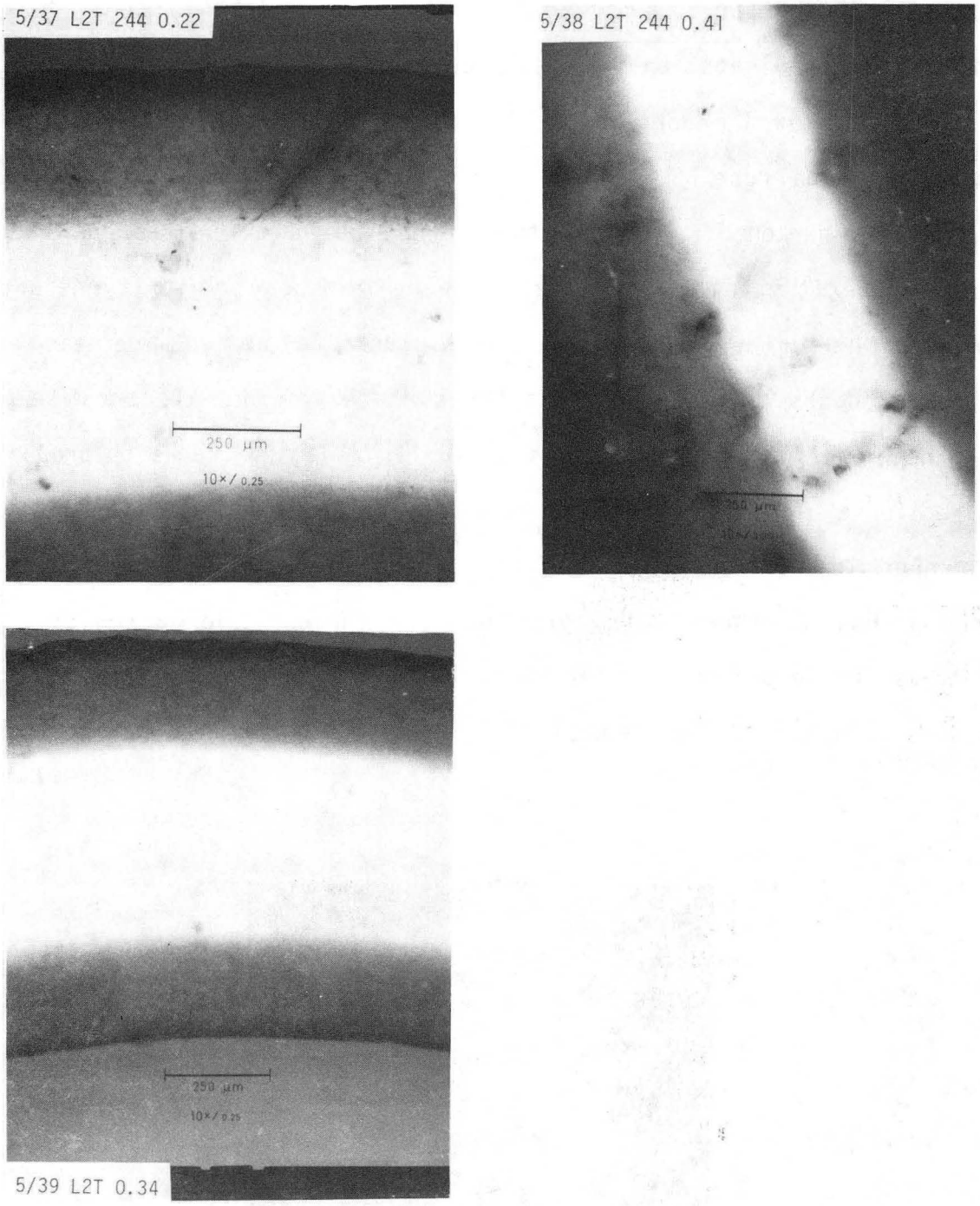

Figure 33. Polished and Stained Cross Sections of CGE Electrolyte

in cell 5/37 is similar to a mechanical crack, but the more intense darkening around the crack indicates that it was present while the cell was being tested. Cell 5/38 has several cracks penetrating throughout the electrolyte, but the staining is more diffuse. Cell 5/39 shows no evidence of mode I cracking. The cells also have darkened layers on both the entrance and exit sides, and blackened layers on the exit sides. In figure 34, there is a crack which turns and runs parallel to the surface of the cell. Such cracks may be fed more readily with sodium than cracks perpendicular to the surface, or the electrolyte may be weakened near the surface but not in the middle, allowing cracks to propagate in this direction at lower stress intensity factor. Figure 35 shows a narrow spot in the darkened layer on the sodium exit side. Figure 36 shows another uneven darkened layer in the electrolyte from cell 5/46. The darkening did not penetrate as far in one spot on the sodium exit side, and in this spot is a large crack, seem to be traversing the entire electrolyte, but without a stained region

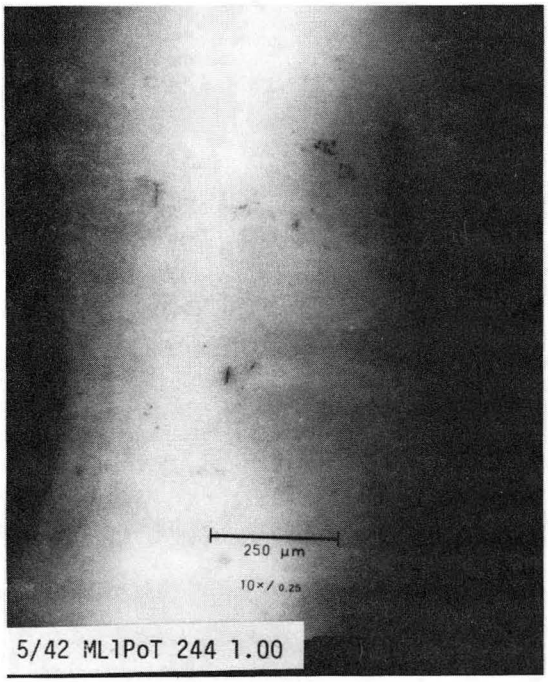

Figure 34. Mode I Crack Parallel to Surface, Cell 5/42

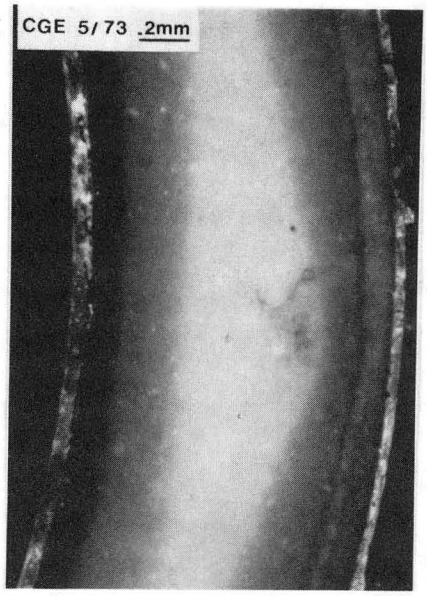

Figure 35. Polished and Stained Cross Section, Cell 5/73 With Narrow Spot In Darkened Layer

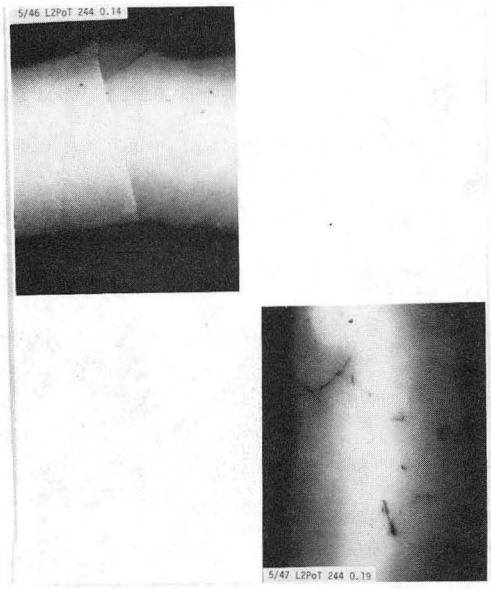

Figure 36. Polished and Stained Cross Section, Cells 5/46 and 5/47 Mode I crack in 5/46 originates in narrow spot in darkened layer.

around it, meaning that it was not exposed to molten sodium, but was formed during sectioning or grinding of the electrolyte. Thus this region is a preferential site for mode I degradation and for mechanical cracking. Cell 5/47 also shows mode I degradation in Figure 36. Near the bottom and on the upper left side of the picture a mode one crack passes through the plane of sectioning. These cracks are long and narrow, ribbon-shaped, taking an irregular path through the electrolyte. In Figure 37 another mode I crack in electrolyte 5/37 appears to end at the end of the darkened region, but it may only leave the plane of sectioning. A specimen from cell 5/37 was repeatedly ground, polished, and photographed to determine the path of cracks through the electrolyte. In Fig. 38 the upper crack appears to end in sections 1, 3, or 4, but in section 2 it penetrates entirely through the electrolyte. Fig. 39 shows the darkened layer at the sodium exit surface an a crack running through the plane of sectioning for electrolyte 5/37. Fig. 40 evidences degraded region with a few grains pulled out

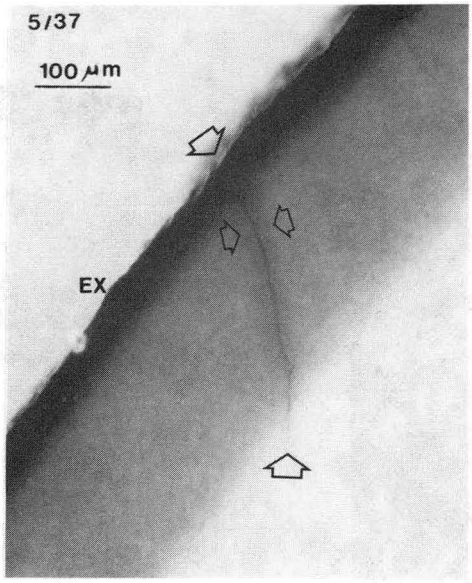

Figure 37. Mode I Crack
In Cell 5/37

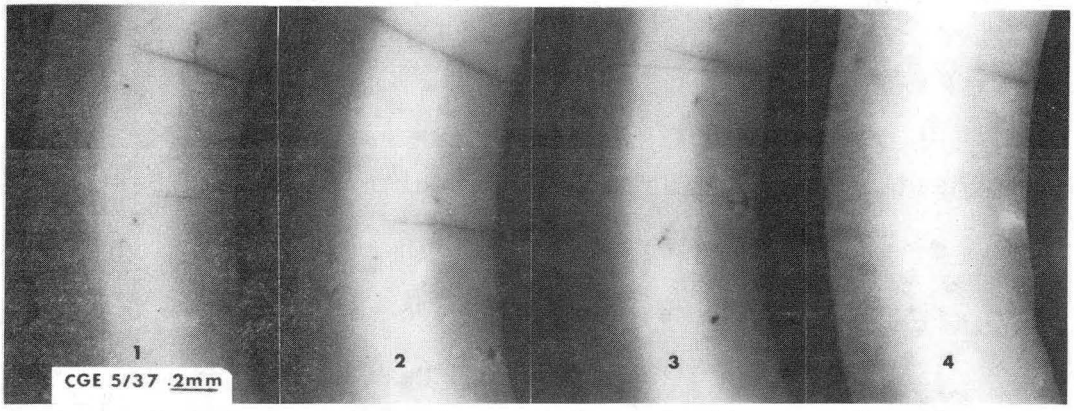

Figure 38. Polished and Stained Cross Sections, Cell 5/37
Sucessive sections show a crack extending part way through the electrolyte in 1, 3, or 4, but all the way in 2.

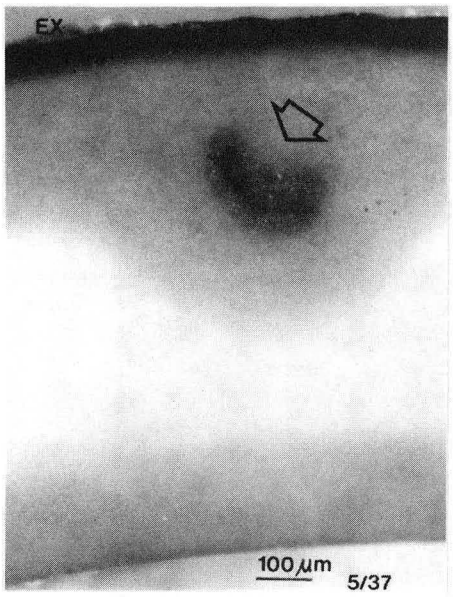

Figure 39. Mode I Crack Running Through The Plane Of Section Of Electrolyte 5/37

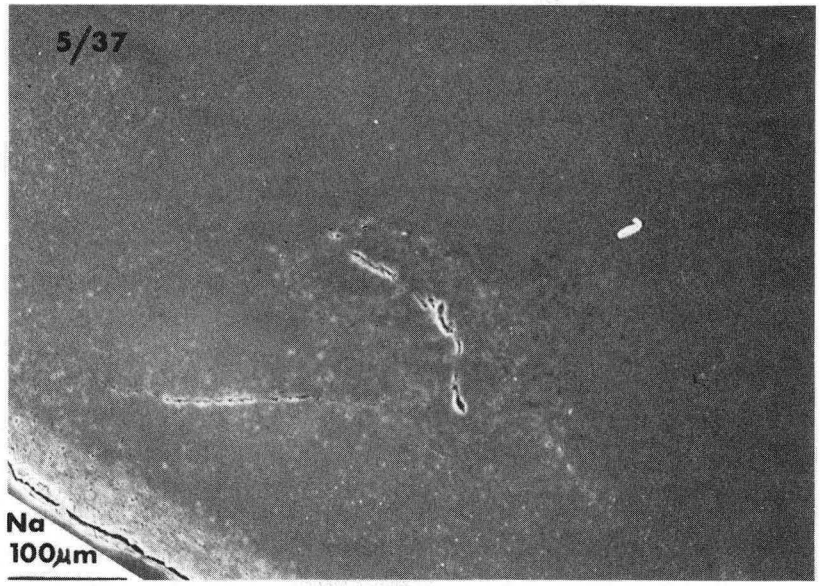

Figure 40. Scanning Electron Micrograph Of Crack First Shown In Fig. 39

polishing. The crack is shown at a higher magnificaiton in Fig. 41, and over most of its length has a width of around one micron. The lower right of the crack, Fig. 42, at higher magnification, shows clearly that material has been removed from the inside of the crack.

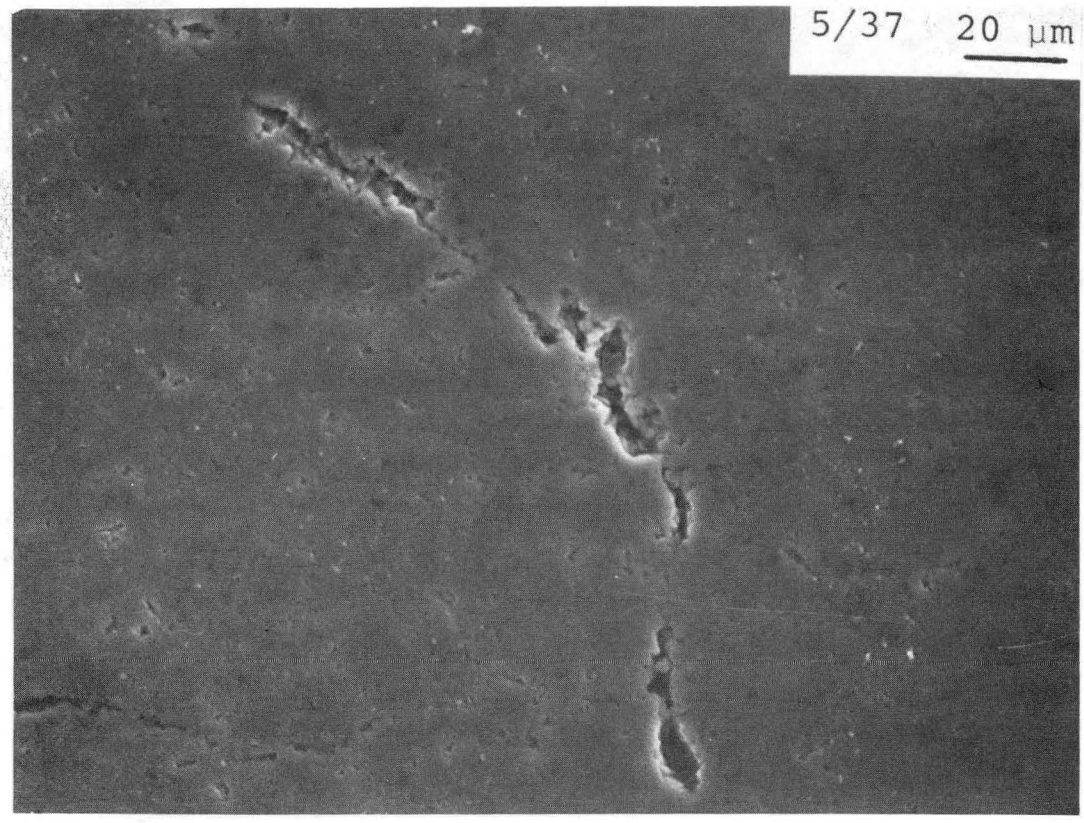

Figure 41. Higher Magnification Of Crack First Shown in Figure 39

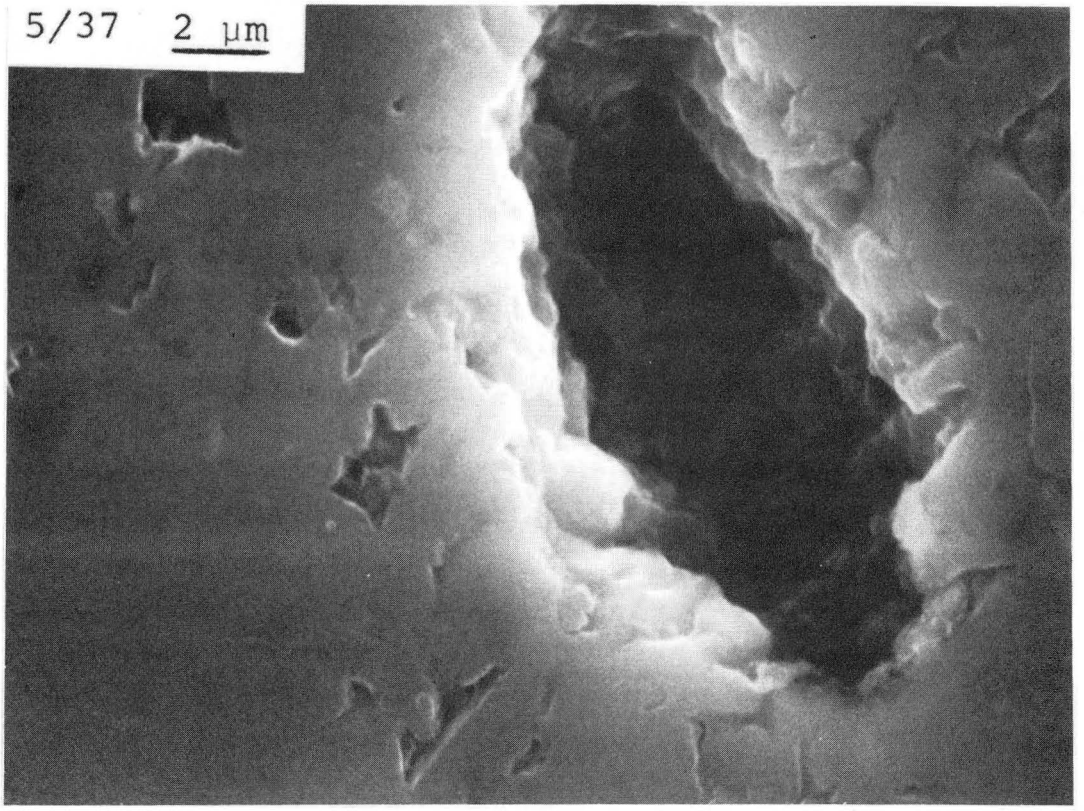

Figure 42. Scanning Electron Micrograph Of End Of Crack First Shown In Fig. 39.

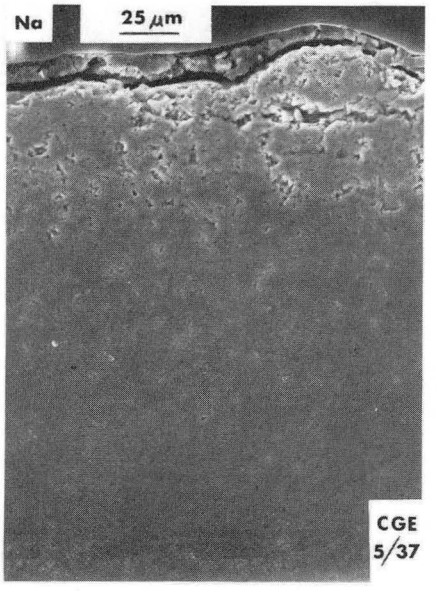

Figure 43. Scanning Electron Micrograph Of Sodium Surface Of Cell 5/37 Showing Intergranular Attack

Examination of the "extra-darkened" layer in the scanning electron microscope, Fig. 43, shows intergranular attack, as was observed in some of the sodium/sulfur cells. The sodium exit and entrance surfaces of cell 5/40, tested unidirectionally, are compared in Fig. 44. While there is substantial intergranular attack on the exit side, there is little or none on the sodium entrance side. This observation excludes the argument that atmospheric corrosion after removal of the electrolyte from the cell and subsequent storage would have caused the degraded layer, since the degradation is different for both sides.

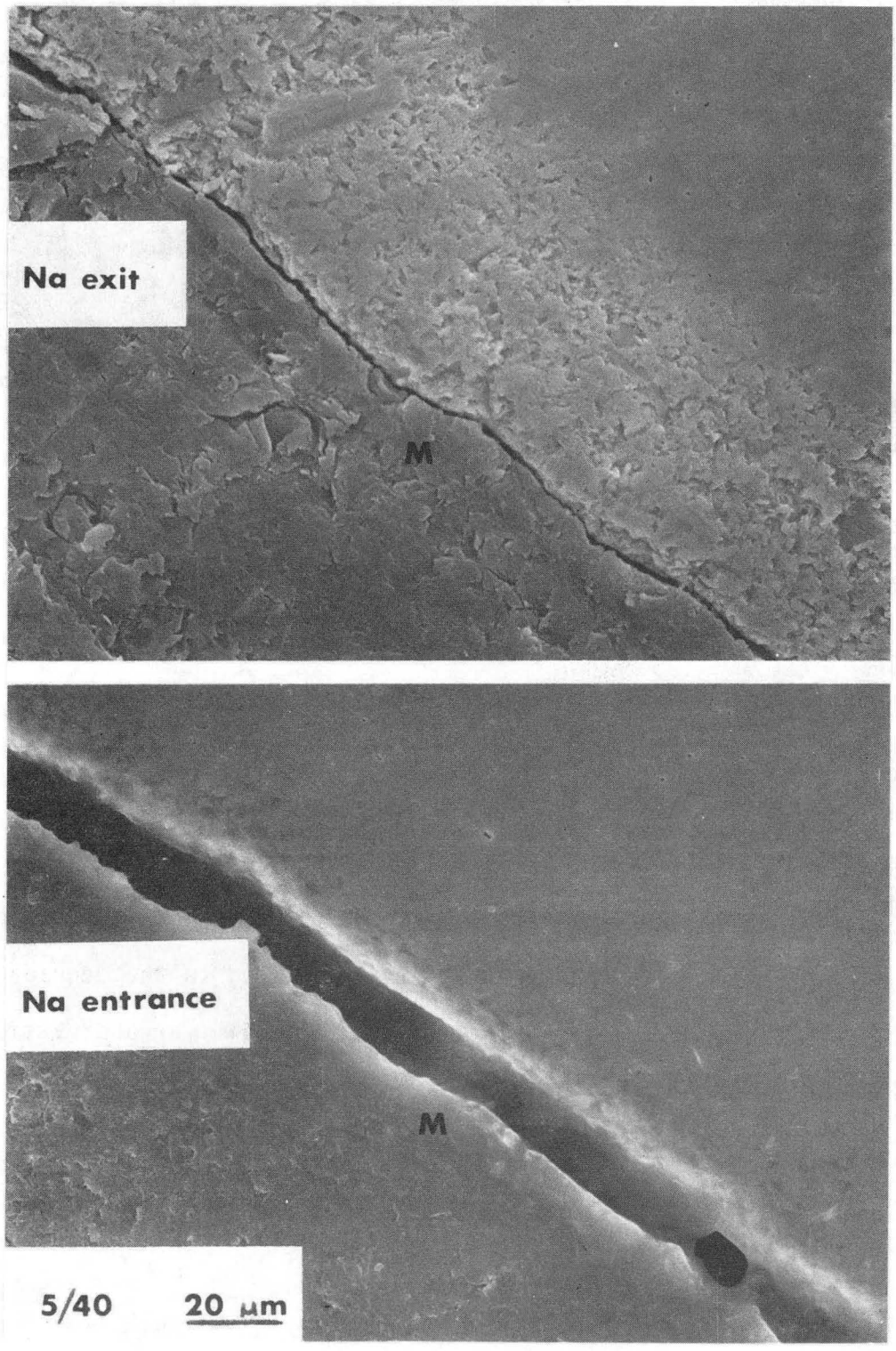

Figure 44. Scanning electron micrograph of cell 5/40 showing intergranular attack on the sodium exit side but not on the sodium entrance side.

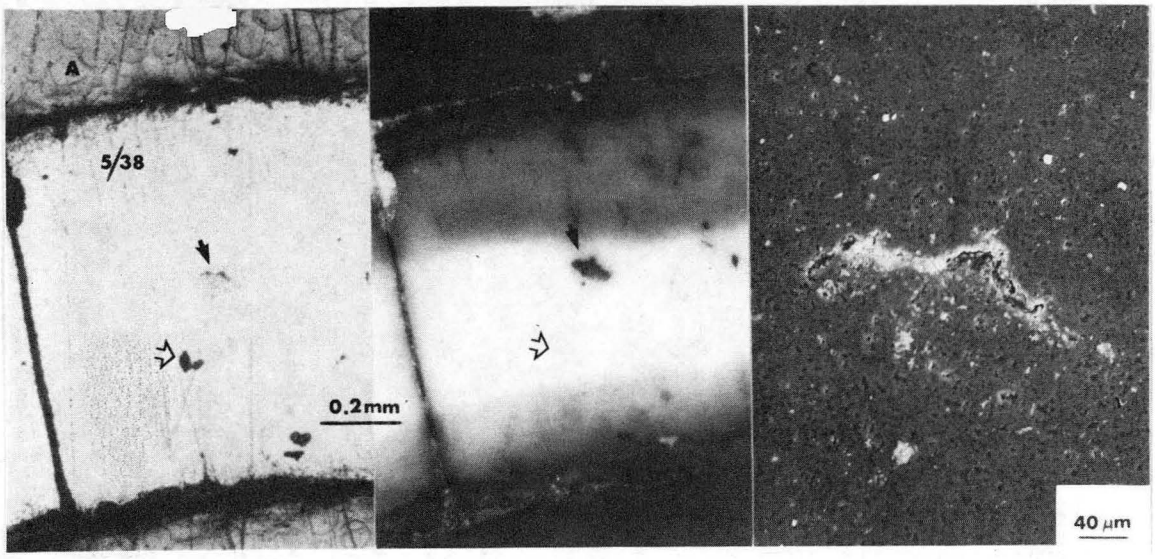

Figure 45. Cell 5/38; (a) pore (open arrow) and possible crack (solid arrow) visible in normal illumination, (b) polarized light, crack is clearly visible, pore is barely visible, (c) crack, SEM.

Fig. 45 shows a region of cell 5/38, containing a Mode I crack under different illuminations, in the optical microscope. Fig. 54A utilizes normal illumination showing pores (open arrow) and a possible crack (solid arrow). With polarized light, Fig. 45/ the crack stands out clearly. The pore is barely visible, showing that sodium penetrated into the crack during operation of the cell, but the pore remained isolated from the sodium and was not involved in the degradation of the electrolyte. Figure 45C shows the crack in the SEM. Similar observations for the electrolyte from cell 5/38 are shown in Figs. 46 and 47. It seems to have suffered severe chemical attack.

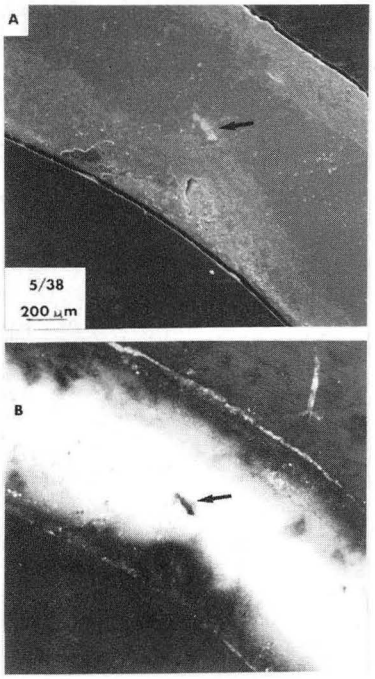

Figure 46. Crack (arrowed) passing through the plane of sectioning; (a) SEM, (b) polarized light.

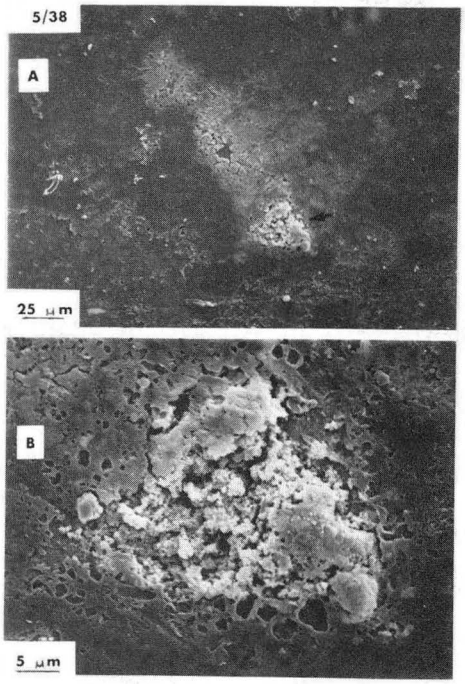

Figure 47. Scanning electron micrographs of the crack first shown in Fig. 46, (a) appears to involve chemical attack, particularly in (b) the lower portion of the crack.

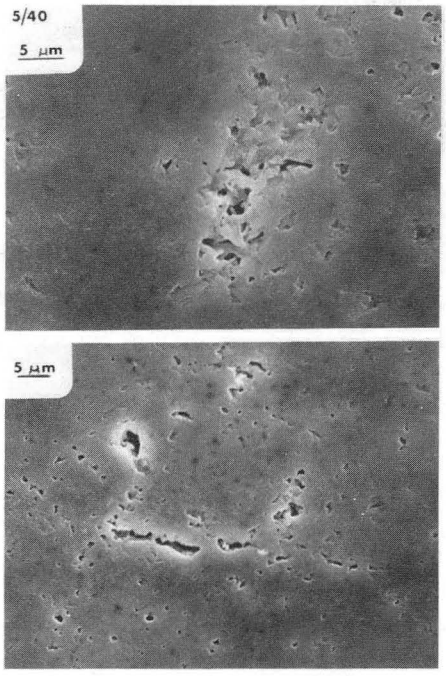

Figure 48. Porous Regions in Cell 5/40

Regions of high porosity, such as Figure 48 were found in cell 5/40 in the SEM. It was not possible to correlate these regions with degradation of the electrolyte. Figure 49 shows a silicon rich inclusion in cell 5/37, and analyses of the inclusion, the light colored ring around it, and the bulk of the electrolyte are given in Table 1. X-ray analysis indicates that the region around the inclusion contains no silver, indicating no exchange occured, and it does not appear dark in the optical microscope, Figure 50. Also there are cracks in this region connecting to the silicate phase inclusion. Thus it may be similar to the unstained regions of cells 5/73 and 5/46 in Figures 35 and 36. Further grinding of cell 5/73 revealed an inclusion similar to that in Figures 49 and 50 but much larger. Clearly, inclusions can be failure origins.

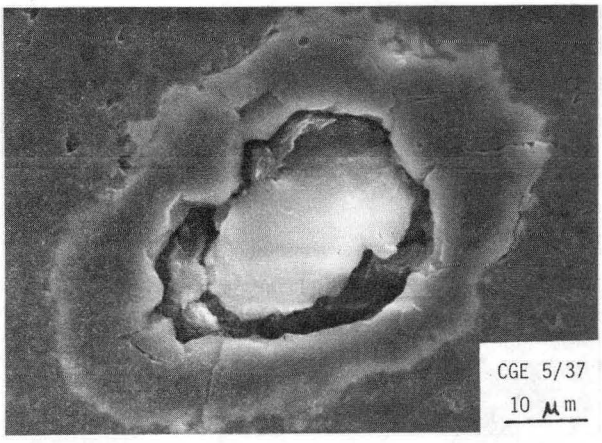

Figure 49. Silicon Rich Inclusion, Cell 5/37, SEM

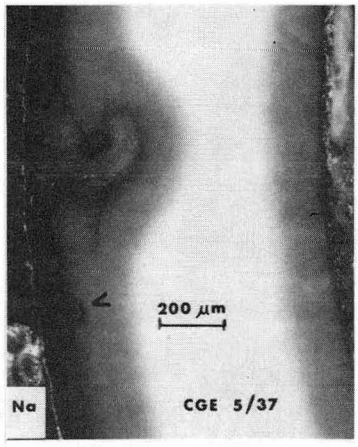

Figure 50. Silicon rich inclusion, arrowed, polarized light.

Table 3 - 1

ANALYSIS OF CELL 5/37

Region	Composition, Weight Per Cent, and (Precision, two standard deviations)					
	Al	Na	Ag	Si	Ca	Cl
Inclusion	6.31	9.40	61.12	4.67	-	18.50
	(0.54)	(1.24)	(1.22)	(0.45)	-	(0.44)
Near Inclusion	48.24	18.99	-	32.10	0.67	-
	(0.58)	(0.57)	-	(0.58)	(0.18)	-
Bulk of Electrolyte	90.90	3.25	5.85	-	-	-
	(0.73)	(0.44)	(0.61)	-	-	-

BBC

Sodium/sodium cells from Brown Boveri had been tested with a maximum current density of 0.77 A/cm^2 and a maximum temperature of 400° C, and the reported charge passed is the total for forward and backward operation. After testing the cells had been cleaned in ethanol, then water, then baked at 800° C for two hours. This baking removes the oxygen vacancies from the electrolyte, so no darkened layers are visible in these tubes. However, the silver nitrate still stains cracks in the electrolyte. The composition of the B cells is 8.7 weight % Na_2O, 2.25% MgO, balance Al_2O_3; ALCOA A-16SG alumina was used. These cells were reported to have asymmetric resistances in the later stages of testing. They had been cleaned and re-assembled during testing, and similar cells that had not undergone this cleaning had no asymmetric resistance. Thus asymmetric behaviour could be attributed to impurities accumulated at the surface. The C, D, and E cells had higher MgO contents. Figure 51 is a polished and thermally etched specimen of electrolyte V69-F206. The grains are tabular with a large variation in size.

Two cells that had no electrolyte failure, but in which glass seals in the cell failed, are shown in Figure 52. Cell B10717 had 15 Ah/cm^2 charge transfer, and cell F3209 had 920 Ah/cm^2. Neither electrolyte has cracks visible in the optical

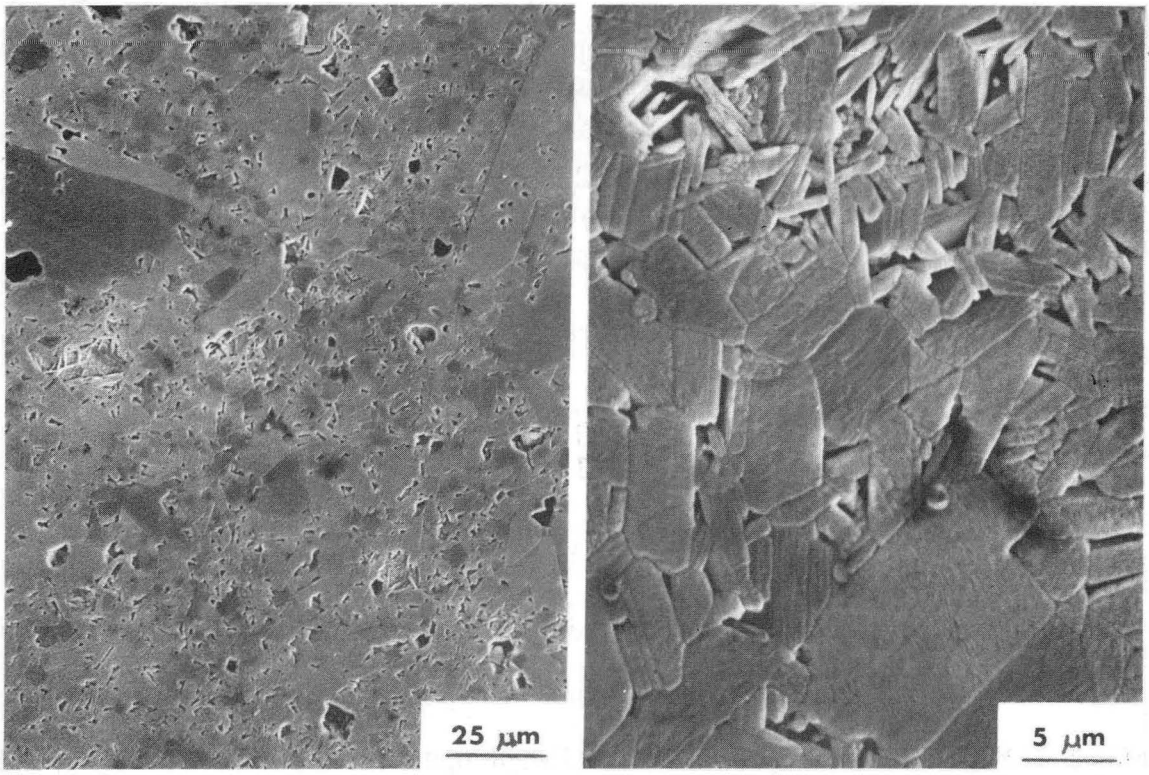

Figure 51. Thermally Etched Brown Boveri Electrolyte V69 F 206

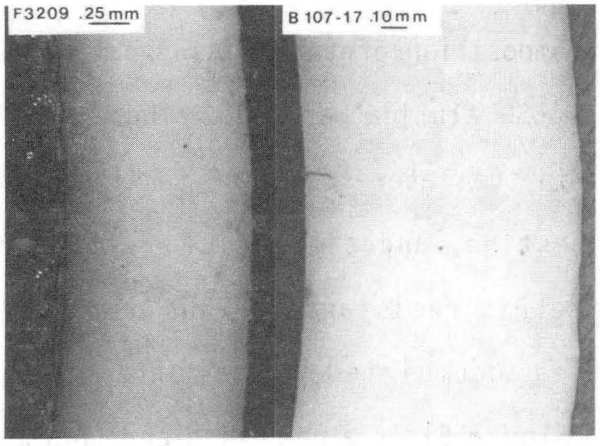

Figure 52. Polished and Stained Cross Sections, Electrolytes F3209 and B107-17

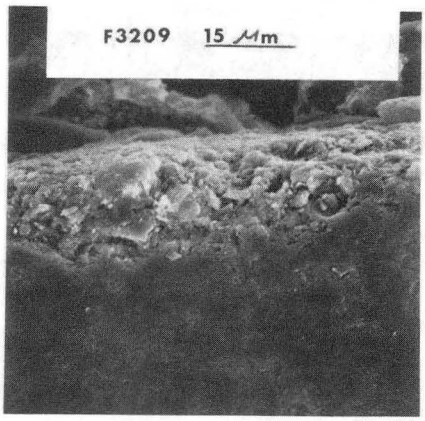

Figure 53. Degraded Layer, Cell F3209

microscope. Figure 53 shows a degraded layer at the surface of cell F3209 in the SEM. Cell D11604, Figure 54, had a total charge transfer of 3610 Ah/cm_2, and after 2200 hours of operation it was disassembled because of seal rupture. After this it was reported to have a 40% asymmetry in cell resistance. The electrolyte shows some evidence of degradation, but no mode I cracks were found. Cell E6123, Figure 55 had increasingly asymmetric resistance during operation. It was operated for a total of 1140 Ah/cm_2, and at the end of operation, the resistance during emptying was 70% higher than the resistance during filling. There is some darkening at the surfaces, indicating degradation. Figure 56 shows surface degradation in the SEM. After a charge transfer of 690 Ah/cm_2, many cracks through the electrolyte are visible in cell V69 F206, Figure 57. The surface degraded layers of electrolytes from cell F206 and E6123 have been compared in Fig. 58, It is clear that the poorer performing electrolyte, F206, had more extensive surface layer damage after 690 Ah/cm^2 than the better performing one, E6123, after 1140 Ah/cm^2. It is likely that the MgO contents had a role in this difference.

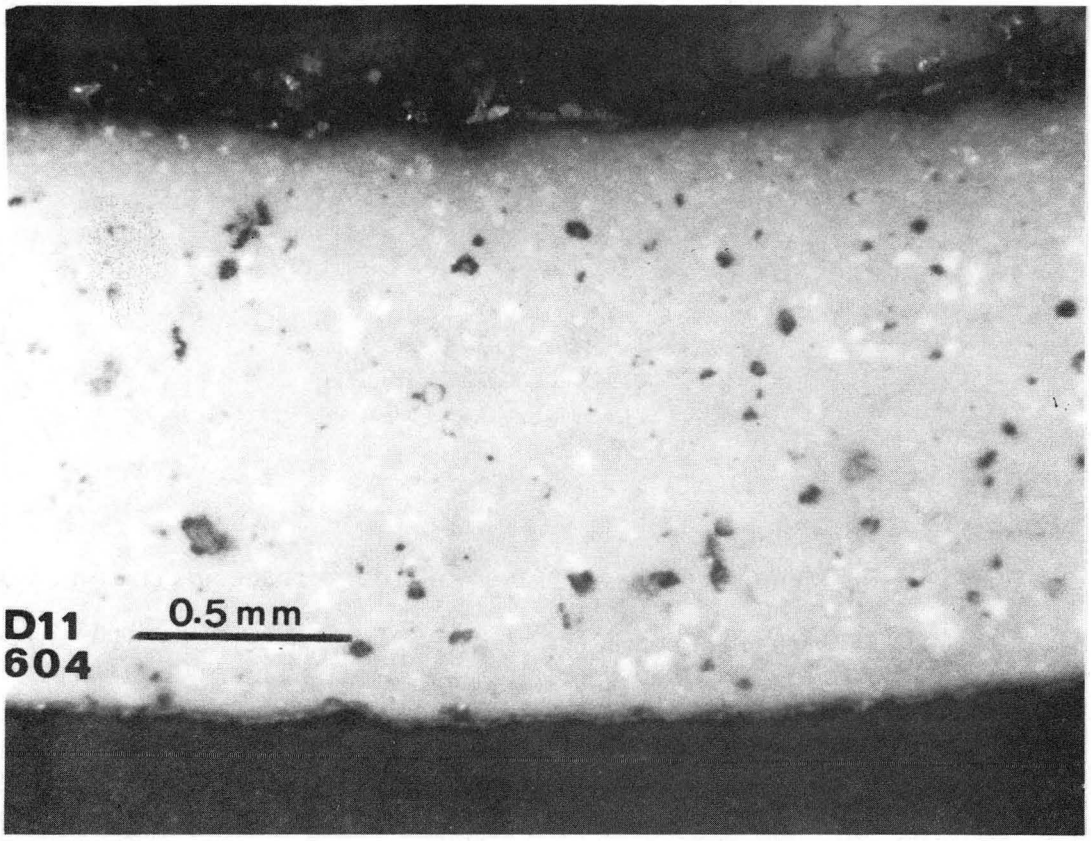

Figure 54. Polished and Stained Cross Section, Cell D11604

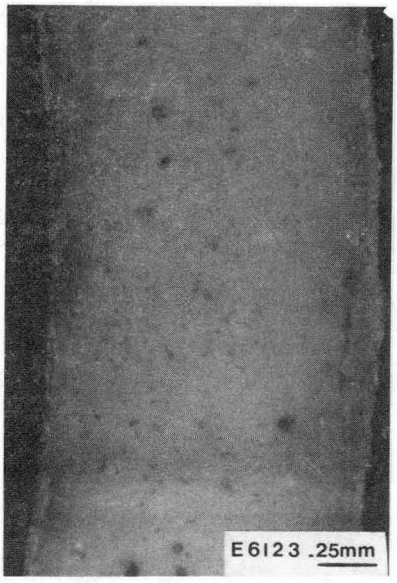

Figure 55. Cross Section of Cell E6123, Polarized Light

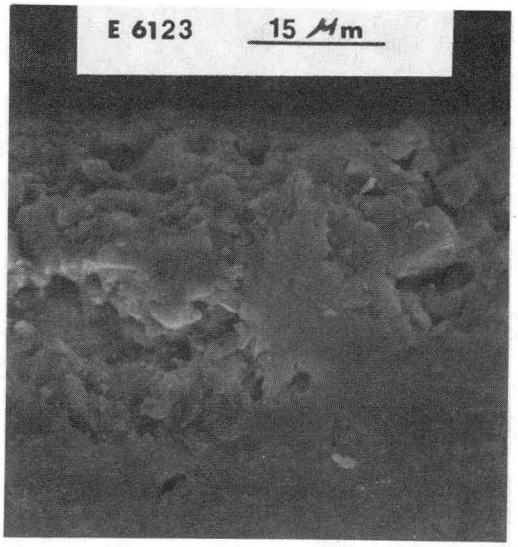

Figure 56. Surface Degradation in Cell E6123, SEM

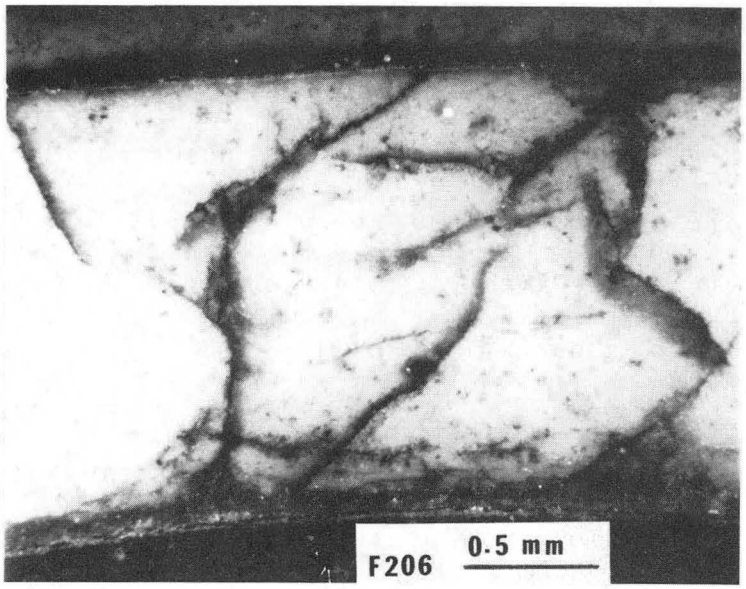

Figure 57. Mode I Cracks in Cross Section of Cell V69F206

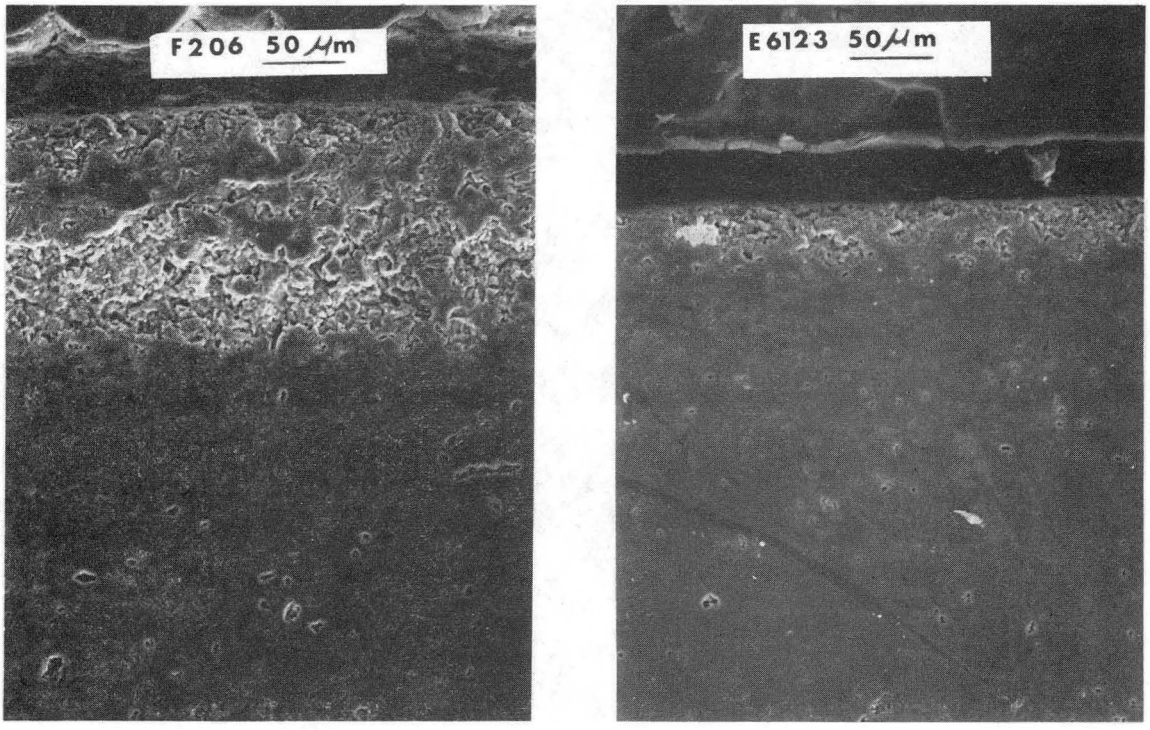

Figure Scanning Electron Micrographs of Surface Degraded Layers

MODE I CRACK MORPHOLOGY

Because of the large anisotropy of the fracture toughness of beta alumina the morphology of cracks is strongly influenced by the irregular microstructure of the electrolyte. Generally mode I degradation produces small cracks, and it is difficult to break the electrolyte along these cracks so that the surface can be investigated. For this experiment, a cell was fabricated from fine grain size electrolyte, A in Fig. 59, but no Na was plated onto the Mo rod, which formed a point contact with the electrolyte. This allowed a high current density to be passed through the electrolyte in a small spot. The current density was increased until the terminal voltage dropped drastically, accompanied by much acoustic activity. A large crack was thus produced. The electrolyte was left in the molten sodium for several days, so the exposed crack surface was darkened. It was

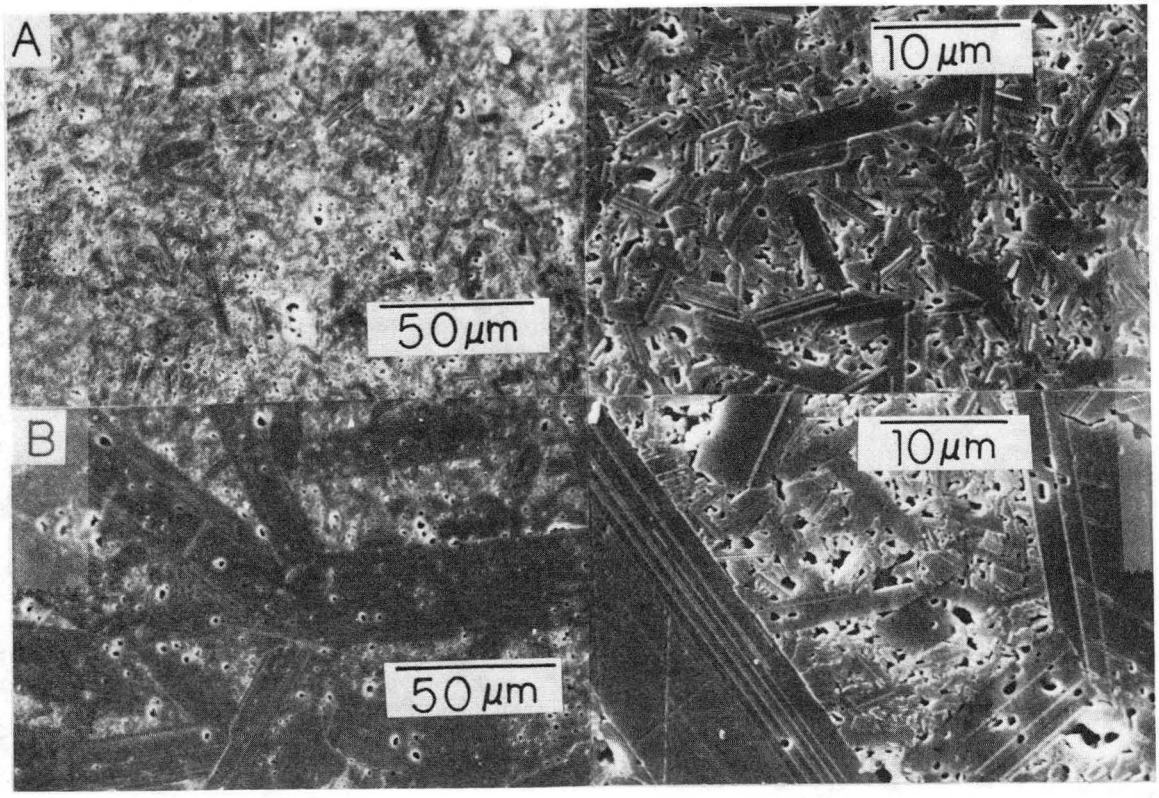

Figure 59. Comparison of Ceramatec electrolyte microstructures. Scanning electron micrographs of electrolyte etched in H_3PO_4.

then stained in silver nitrate solution, coloring the surface that had been exposed to Na dark brown. Then the electrolyte was broken, revealing stained surface that had been produced by mode I degradation, Fig. 60A and unstained surface produced by mechanical fracture, Fig. 60B. In both cases in Figure 60 fracture is largely intergranular or follows the 00.1 conduction planes of the grains, and the surface produced by Mode I degradation at high current density does not differ from that produced by mechanical fracture. It is difficult to distinguish between these two possibilities from the investigation of fracture surfaces.

Figure 60. Scanning Electron Micrographs of Surfaces Produced by (A) Electrolytic Degradation and (B) Mechanical Fracture

The crack of Figure 61 was produced by a Vickers hardness indenter in a specimen of electrolyte that had been thermally etched to reveal the microstructure. Most of the crack seems to follow the grain boundaries, but the arrowed grain in figure 62, enlarging a crack detail on the indented surface, is cleaved on the conduction plane.

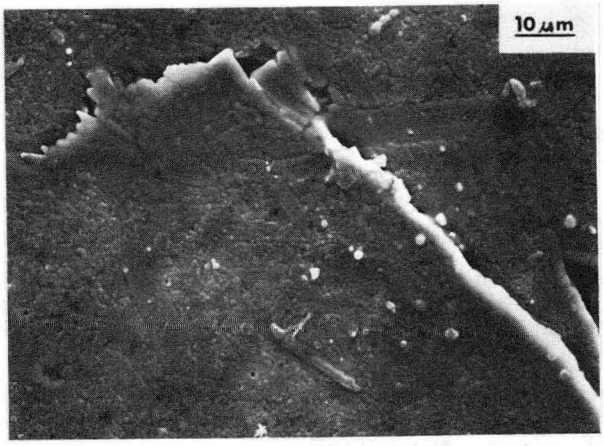

Figure 61. Scanning Electron Micrograph of Crack Produced by Vickers Hardness Indenter.

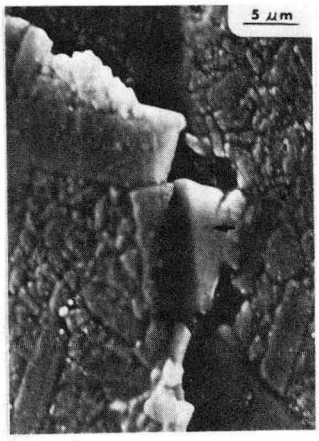

Figure 62. Higher Magnification of Grain Cleaved on the Conduction Plane

In Figure 63 a large grain is fractured in the short direction, which is typically perpendicular to the 00.1 planes. Cracks in beta alumina are mostly intergranular, but in large grains transgranular fracture may be observed, and this transgranular fracture follows the 00.1 clevage planes if they are oriented favorably.

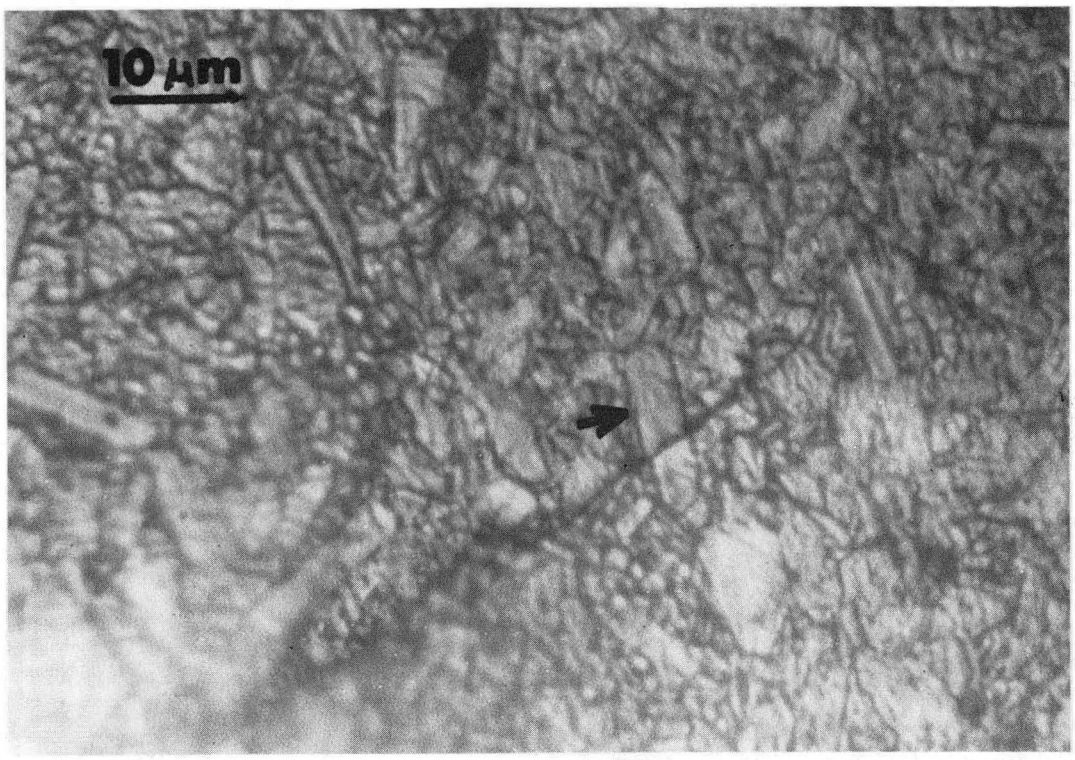

Figure 63. Large Grain Fractured in the Short Direction

MODE I FAILURE INITIATION MICROMORPHOLOGY

Grain boundaries are preferred paths for mechanical cracks, and a test was performed to determine whether they are also preferred sites for the initiation of mode I degradation.

A disc of large grain size beta"-alumina, microstructure B in figure 59, was ground and polished with one micron diamond paste on both sides, and a sodium/sodium cell was fabricated from it. This cell was operated in only one direction, with the inside electrode always acting as the cathode. It was operated at 300°C with a current density of 100 mA/cm_2 for 152.5 hours, then removed from the Na and cleaned in ethanol. The electrolyte was stained in silver nitrate solution so that any cracks that might have formed during testing would be visible under the optical microscope. No sign of degradation were seen on the

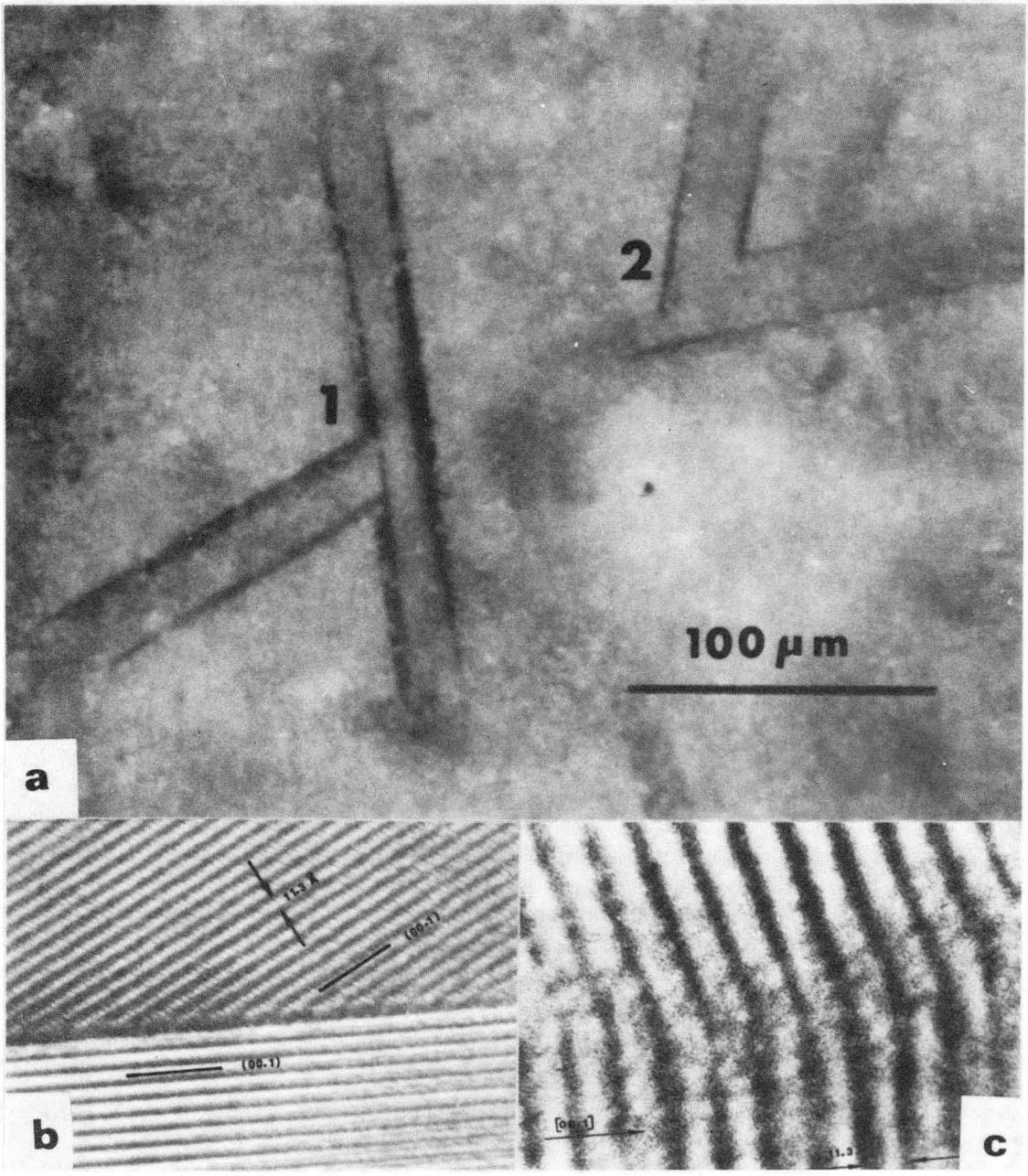

Figure 64. Grain Boundary Cracks; (a) optical micrograph of cathode surface, (b) TEM lattice image of a boundary similar to 1 in (a), (c) lattice image of a boundary similar to 2 in (a).

anode surface, but on the cathode side the cracks of Figure 64 (a) at the boundaries of large grains were observed.

The difficulty with which fracture can propagate through grain boundaries depends on grain boundary orientation and structure. Evidence for this dependence on

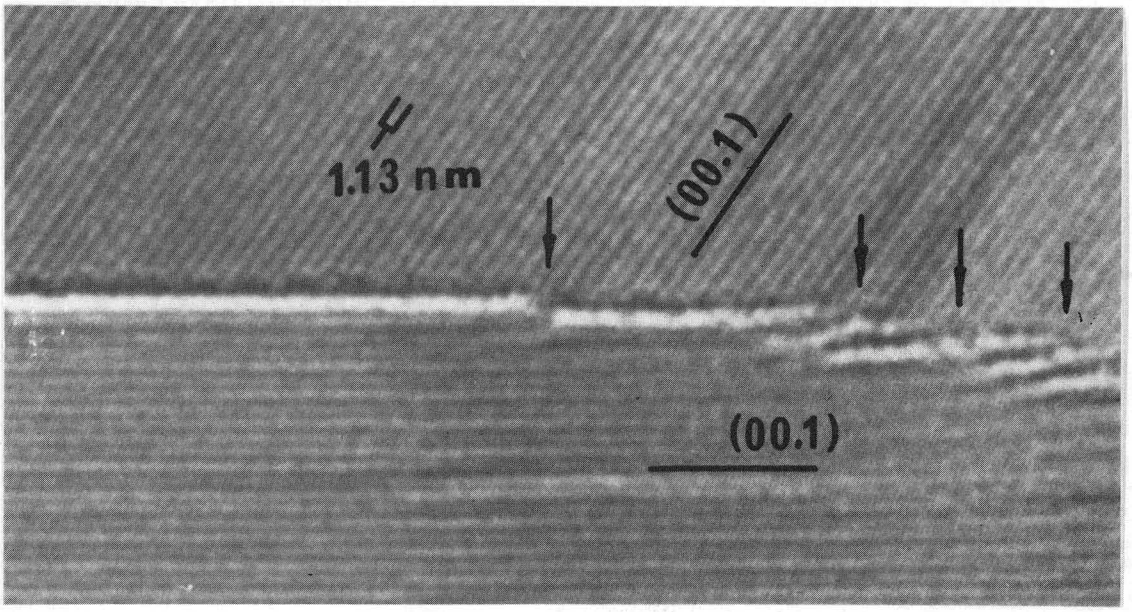

Figure 65. Transmission Electron Micrograph of Crack in Thin Foil

microstructural detail can be seen directly in fig. 65. This micrograph shows a fracture along a grainboundary that is partly faceted along a 00.1 plane. The fracture was caused during observation of the thin foil in the transmission electron microscope, as a result of stresses caused by electron beam induced soda loss and subsequent lattice collapse in an adjacent part of the foil. It is clear that where the grainboundary deviated from an exact 00.1 facet, direct spinel-spinel block bonding survived with the crack now following the conduction planes rather than the grainboundary, which is the opposite situation for the exact 00.1 faceted grainboundary. This observation shows directly that the grainboundary strength depends on the grainboundary structure. The 00.1 faceted grainboundaries are weaker than the conduction planes, while the grainboundaries that have direct spine-spinel block bonding are stronger. It may be postulated therefore that the 00.1 faceted grainboundaries have oxygen ion density related to that of the conduction planes rather than that of the spinel blocks. This would make such grainboundaries chemically different from the average electrolyte composition, an inference which would imply that grainboundaries are soda-rich, or alumina poor

compared to the average electrolyte composition and might account for the preferential attack of various forms of degradation along the grainbondaries or large, 00.1 facted grainboundaries.

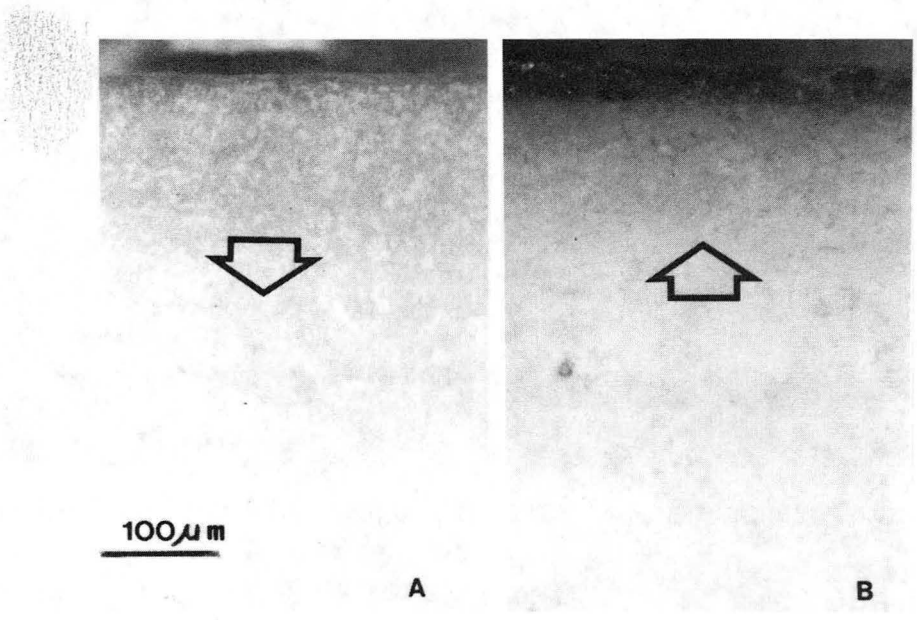

Figure 66. Polished and Stained Cross Section of (A) Anode and (B) Cathode

A cross section of the electrolyte has a chemically darkened layer at both the anode, Figure 66A and the cathode, Figure 66B but only the cathode has a thin, extremely dark layer with a high density of microcracks. Mode I degradation has propagated through this layer, but the cracks have not yet reached critical length to penetrate rapidly through the electrolyte.

From Figure 65, the strength of a grain boundary can be seen to depend on its orientation. The lattice image of Figure 64b shows a boundary similar to the boundary between two large grains labeled 1 in Figure 64a, while the boundary labeled 2 in Figure 64a is similar to that of Figure 64C, with the spinel blocks of one grain joining the spinel blocks of the other. Grain boundary 1 is cracked, but grain boundary 2 is not, indicating that 00.1 faceted boundaries are

preferred sites for the initiation of mode I degradation. Although they are stronger, the second type of boundaries can also undergo mode I failure. A mode I crack has penetrated a grain boundary with joining spinel blocks in Figure 67, and the dark material in the crack is sodium carbonate.

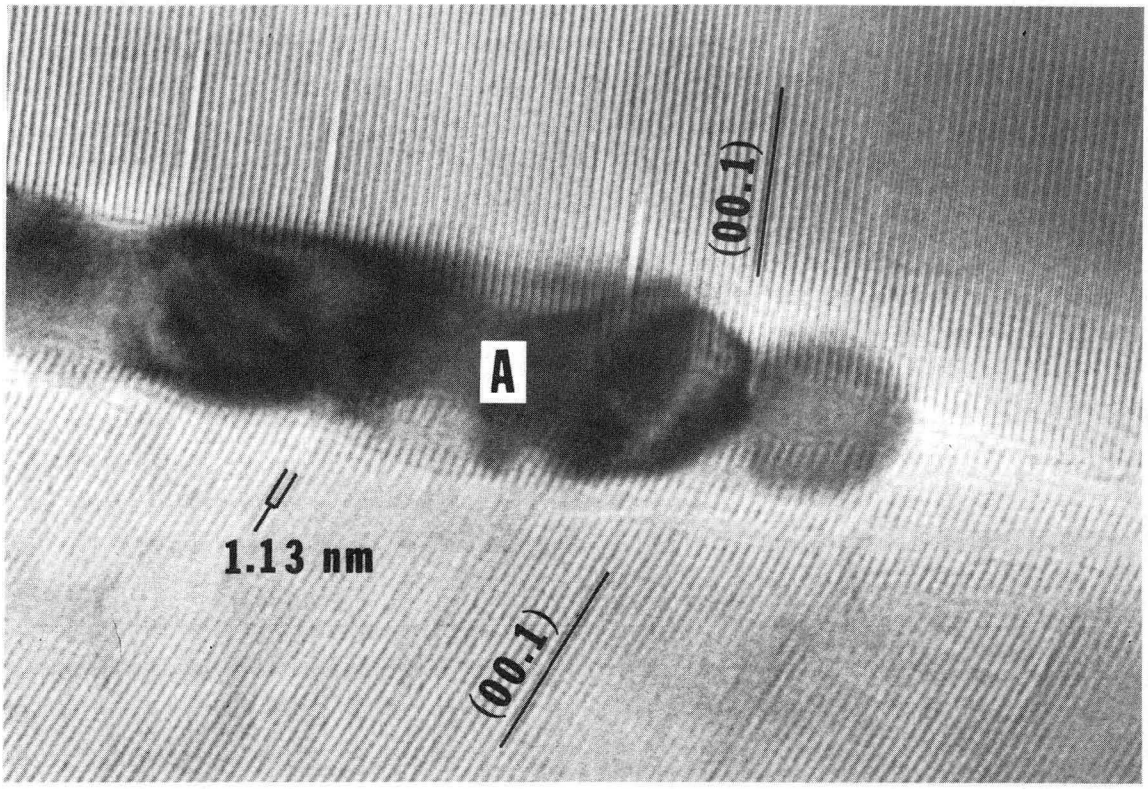

Figure 67. Transmission Electron Micrograph of a Mode I Crack on a Grain Boundary

ACOUSTIC EMISSION DETECTION STUDIES OF CRITICAL CURRENT DENSITIES

A study of the dependence of the critical current density at which degradation begins on temperature, surface condition, and time was performed on fine grain size beta"-alumina, microstructure A in figure 59, prepared by Ceramatec, Inc. Sodium/sodium cells were run overnight at 25 mA/cm^2 with the inside electrode acting as the cathode, and then the current was reversed for 30 minutes to insure good wetting of the outside surface of the electrolyte. The current was again

reversed for another 30 minutes, then the cells were tested. A current ramp was generated with a programmer and galvanostat (Princeton Applied Research Corporation, Princeton, New Jersey, Model 175 Universal Programmer and Model 371 Potentiostat-Galvanostat) so that the current through the cell started at zero and increased linearly with time as the stress or strain would in a mechanical strength test. The current vs the terminal voltage was plotted on an x-y recorder.

As the cell current increased, first a few intermittent signals were detected, and then at a higher current density the acoustic activity became continuous. Finally the cell voltage recorded on an x-y recorder, dropped slightly. Thus three parameters were obtained for each cell; the current densities at which acoustic emission began and then became continous, and the current density at which the terminal voltage dropped.

Propagation of Mode I cracks depends on the distribution of surface flaws, and on the distribution of surface flaws, and on the distribution of local current densities at these flaws, and on the microstructure of the materials around the flaws. When these factors are combined, a critical current density exists for each flaw. These flaws are distributed at random over the surface of the electrolyte, so there is a random distribution of critical current densities on this surface, and the electrolyte will fail when the lowest of these critical current densities is exceeded. Then assuming that the critical current densities of flaws or elements of electrode area close to each other may be dependent, but any dependence weakens with distance, the critical current densities of electrolyte specimens can be described by Weibull statistics (8). Then the probability of survival, P_s , of a specimen of area A tested to current density i is:

$$P_s = \exp \{ -\int_A [(i - i_u)/i_o]^n \, dA \} \qquad (3\text{-}1)$$

where i_u, i_o, and n are materials parameters. Eqn. 3-1 follows from the mechanical analogue for a sample subjected to a non-uniform stress σ, for which

$$P_s = \exp \left[- \int_A (\sigma - \sigma_u) / \sigma_o)^m dA \right] \qquad (3\text{-}2)$$

where σ_u and m are materials parameters and σ_o is a normalization factor.

Then, if the variations in current density over the electrolyte surface are random and have only short range interactions, as should be the case with the variations in local current density caused by variations in electrolyte microstructure, these variations can be ignored for the purpose of integrating equation (3-1), so

$$P_s = \exp (- A[(i - i_u)/i_o]^n) \qquad (3\text{-}3)$$

It will be assumed here that the current density below which $P_s = 1$, i.e., i_u, is zero. This assumption has the effect that extrapolation of data to electrode areas many times larger than the test area leads to a vanishing survival probability at finite current densities. Since large electrolyte tubes are known to survive finite current densities, the assumption that $i_u = 0$ is not justified as it would lead to significant errors upon extrapolation. From the tests reported here, i_u could not be determined, an the data should, therefore, not be used to extrapolate to large electrolyte tubes; they can, however, be used for mutual comparison and for putting an upper bound on i_u.

The current density at which acoustic emission began can be associated with the first crack extension of the lowest critical current density flaw, and thus the above analysis is appropriate. A flaw may begin to propagate in a region of low K_c, and then be arrested when it reaches a stronger region of the electrolyte.

This is to be expected because the critical current density depends strongly on K_c, as follows from the relation (4)

$$i_{crit} = C\, K_{Ic}/\ell \qquad (3\text{-}4)$$

where C is a constant depending on the crack geometry and l is the flaw size. When the current density becomes great enough so that a flaw continues to propagate through the electrolyte, continuous acoustic emission is observed. Thus continuous acoustic emission involves not only the surface flaw distribution, but also the strength of volume elements inside the electrolyte, so the treatment above is not strictly correct, but the data has been treated in the same manner as the initial acoustic emission data. Finally, the current density for a drop in cell resistance, which indicates that a crack has propagated through the electrolyte, was also plotted on a Weibull plot. For purposes of plotting, the log of equation (3-) was taken twice, giving

$$\text{Log Log } (1/P_s) = \log(A) + n \log (i) - n \log (i_o) \qquad (3\text{-}5)$$

The Weibull modulus, n, is then the slope of the plot, and it is related to the variability of the data, a small Weibull modulus corresponding to much variation in the critical current density. The data are ranked, and the mean rank position of the jth ranked specimen from a total of N specimens is

$$P_s = 1 - j/\,(N+1) \qquad (3\text{-}6)$$

Cells were tested at 200°C, 300°C, and 350°C, with as sintered and with ground surfaces, and at rates of increase of current density of 1 mA/cm^2 sec and 10 mA/cm^2 sec. The data for the current density and terminal voltage at which a drop in cell resistance occured for fine grain size cells with as sintered surfaces are plotted in Figures 68 and 69. For these tests, the critical current density was not clearly related to temperature, and the corresponding voltages differed because the resistivity of the electrolyte varied with temperature. For this

reason, the rest of the data were plotted vs. current density. Figures 70, 71, and 72 show that the critical current density for initial and continuous acoustic emission and for a drop in cell resistance all increased when the rate of increase of current density in the test was higher. The effect was greater for initial than for continuous acoustic emission, and was least for the drop in cell resistance. This indicates that the time dependence for the initiation of mode I degradation is greater than that for the propagation of the cracks. They probably propagate by mechanical cracking due to pressure of the sodium in the crack, as first described by Armstrong et al. (1), but the initiation stage may involve some chemical or electrochemical attack, and the mechanism may also be responsible for the formation of the degraded layer observed in used electrolytes.

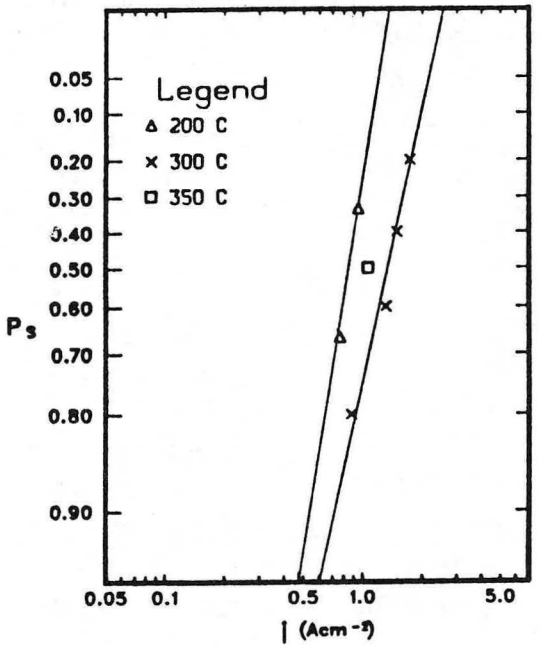

Figure 68. Current Density at Which Cell Resistance Dropped at Various Temperatures

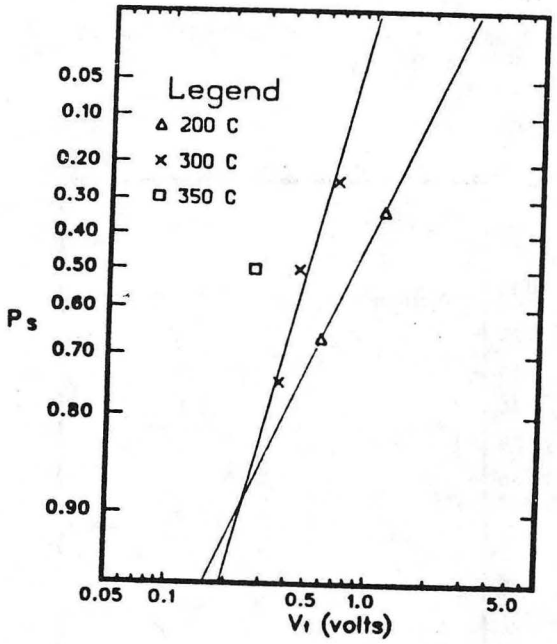

Figure 69. Terminal Voltage at Which Cell Resistance Dropped at Various Temperatures

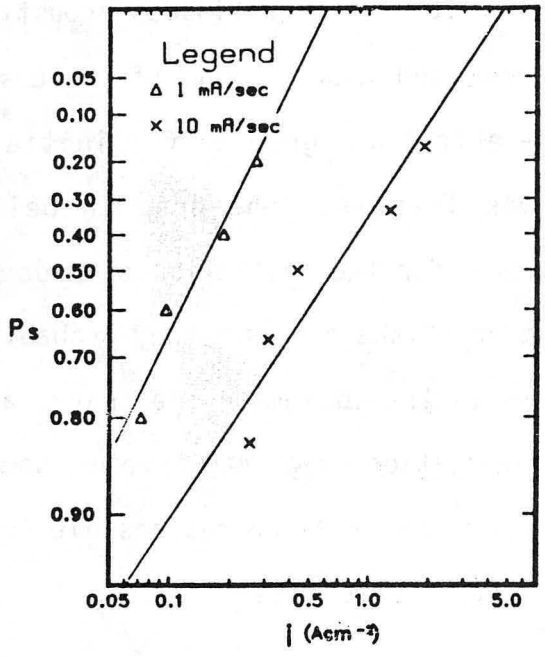

Figure 70. Initial Acoustic Emission for Various Rates

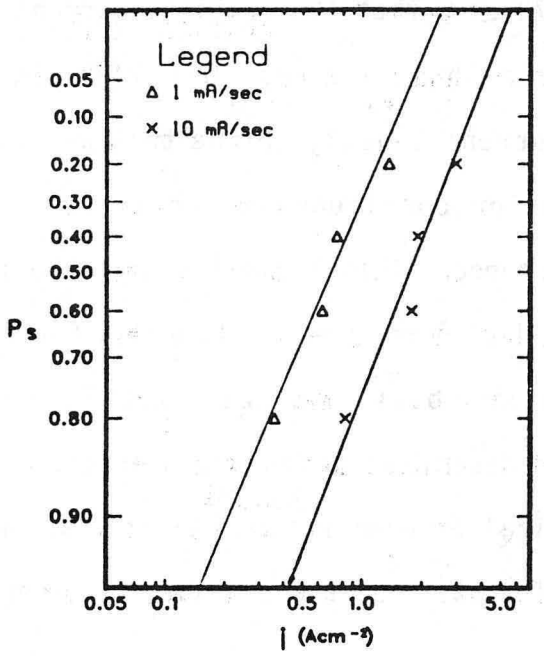

Figure 71. Continous Acoustic Emission for Various Rates

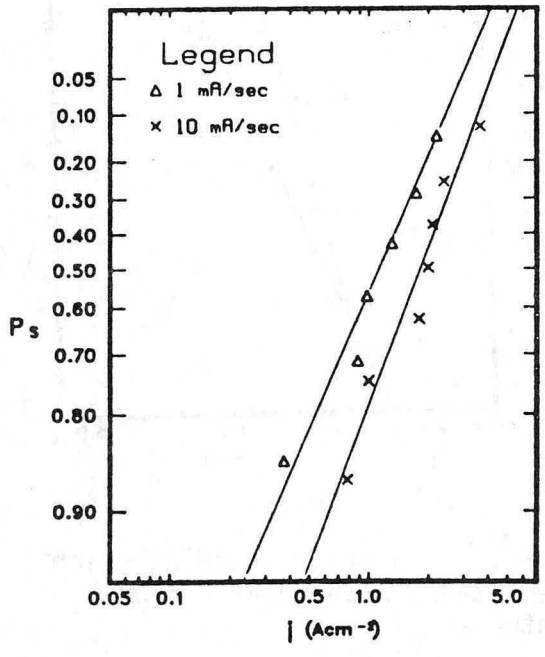

Figure 72. Terminal Voltage Drop for Various Rates

STRENGTHENED ELECTROLYTES

A limited amount of testing of the criticalcurrent densities for failure initiation was performed on beta" alumina that was toughened by a dispersion of metastable zirconia particles. The strengthening effects of such dispersions have been well documented for a variety of ceramics, including alumina and mullite. It was therefore resonable to expect that similar mechanical strengthening effects might beneficially affect the performance of the electrolyte. Testing of such electrolytes for critical current densities would, at the same time, be a test for the qualitative aspects of failure initiation theories predicting that the critical current densities depend on the fracture toughness raised to the fourth power.

The zirconia dispersed electrolytes were prepared by Rockwell International, Thousand Oaks, California. As received beta"-alumina powders (supplied by Ceramatec, Inc.), were prepared into slips using 1 butanol, and ultrasonically dispersed. Fine zirconia particles (2.2 mole% yttria) were mixed in up to 20 vol%. Large agglomerates were removed by a sedimentation technique, and specimens were prepared in disk form by a pouring them in teflon molds on plaster of paris forms. The fired specimens were tested in the acoustic emission detection set-up, in a manner identical to the usual specimens, at a current increase rate of $1mA/cm^2$ sec. The results are plotted in a Weibull statistical plot in Fig. 73. Clearly, there is a very significant increase in the average failure current densities.

The average failure current density for the reference material, the usual Ceramatec product, is 700 mA/cm^2 while that of the toughened ceramic is 2600 $mA/cm2$. The ratio of the average critical current densities for failure is thus 3.7. The Weibull slopes do not appear to be affected very significantly by the strengthening process, although the Weibull modulus for the toughened electrolyte

appears somewhat larger, 4.54 versus 4.2 for the single phase electrolyte. It is worthwhile to note that the strengthening process has improved a 10% survival probability to an 80% one. clearly, this effect would have far reaching consequences, possibly improving the performance of the sodium/sulfur cells dramatically, if the lifetimes would be similarly affected. Lifetime tests are, however, outside the scope of this work.

The ratio of the fracture toughnesses of the Ceramatec single phase electrolyte to the toughened electrolyte was about 1.25, as determined by microhardness indenting, for electrolyte containing 15 vol% zirconia (9). Electrolyte resistance was reported to be about 6-8 Ωcm at 300°C.

FRACTURE TOUGHNESS ANISOTROPY

Beta and beta" alumina crystals cleave easily along the 00.1 conduction planes. The fracture toughness for cracks should thus depend significantly on the crack habit plane. This anisotropy was investigated on single crystals of sodium-beta alumina. The microhardness-indenter fracture toughness method had to be used since only small single crystals were available.

A single crystal of sodium-beta alumina and polycrystalline sodium-beta" alumina were heated for 24 h at 900°C in beta-alumina packing powder and were then mechanically polished. Polishing was necessary to enable accurate measurement of the crack length after indentation. The 00.1 cleavage surface of the single crystals was smooth and needed no further preparation. The prismatic planes of the single crystals could only tolerate minimum prepartion since, however carefully the sanding and polishing were performed, several 00.1 cleavage cracks would result. The few cracks that were produced did not interfere with the measurements since indents could be made on unflawed prismatic plane segments, and the crystals could be viewed in transmitted light. After the surfaces were prepared, the

samples were annealed in packing powder of the appropriate Al_2O_3/Na_2O composition for 3 h in air at 1500° C. This treatment healed many cracks and roughly corresponded to a sintering cycle. The polycrystals showed considerable thermal etching, but the indent cracks could still be measured with accuracy under oblique illumination in the optical microscope. Indentations were made with a Vickers diamond indenter, with loads between 19.6 and 49.0 N. For indents on the prism planes, one diagonal of the indenter was aligned to within 0.2 with the basal planes of the crystal. This alignment produced a basal-plane crack and a crack normal to the basalplane, for prismatic-plane indents, as shown in Fig. 74. During indentation, the surfaces were covered with immersion oil to prevent possible crack extension resulting from ambient moisture. After indentation, the immersion oil was removed with acetone, and the crack dimensions were measured immediately.

Theoretical consideration of the critical current densities for mode I failure initiation predict that the critical current density is proportional to the fracture toughness to the fourth power, according to eqn. (3-3). For reasonable flaw lengths, and using the fracture toughness measured on polycrystalline electrolytes by macroscopic fracture-mechanics methods (10), the calculated i_{cr} is found ot be several orders of magnitude above the observed one. However, for materials that are as anisotropic as the beta aluminas, macroscopic fracture toughness should not be used when flaws are on the order of the grain size. In the early stage of growth, small cracks should advance through regions of low critical stress intensity, with the fracture toughness increasing to the value appropriate for macroscopic fracture mechanics as the crack gets larger.

In sodium-beta and beta" aluminas, microstructural features can lower the strength of the electrolyte very significantly. The layered crystals cleave easily along the 00.1 conduction planes and may show spontaneous fractures when

left in ambient moist air. Grain boundaries with 00.1 habit planes are also known to be mechanically weak (11). Since 00.1 cleavage is most likely to be involved in the initial crack configuration and growth, it is necessary to determine the K anisotropy. The K_c values were found from cracks produced by a microhardness tester on basal and on prismatic planes of sodium-beta alumina single crystals. The expression used to calculate K_c was (13):

$$S = K_c(H/E)^{1/2}/(P/c^{3/2})$$
$$= 0.016+/-0.004 \qquad (3\text{-}7)$$

where S is a material-independent constant for radial cracks produced by a Vickers diamond indenter, H the hardness, E Young's modulus, P the load on the indenter, and c the measured length of the radial cracks. The Young's modulus for polycrystalline sodium-beta alumina is reported to be 200 GPa. For indentaiton fractures in elastically anisotropic crystals, the modulus E used in Eq. (3-7) should be that for the direction perpendicular to the crack-habit plane, provided that the indenter axes were aligned to within a few degrees with the principal axis of the elasticity tensor. Measurements of the elastic anisotropy were not available, but a fair estimate can be made from the shape of Knoop indents. Knoop indents were made on basal-plane surfaces and on prism-plane surfaces with the long axis of the indenter in the 00.1 plane. In the fully loaded state, the ratio of the length of the long axis, a, to the length of the short axis, b, of the indent is 7.11. When the load is removed, the length of the long axis of the indent remains constant, but the length of the short axis decreases by an amount depending on H/E, the ratio of the hardness-to-elastic modulus. The ratio H/E was found from:

$$b'/a = b/a - kH/E \qquad (3\text{-}8)$$

where b' is the length of the short axis after the load has been removed, and k is a constant equal to 0.45. Hardness, H, was calculated from Vickers indents and

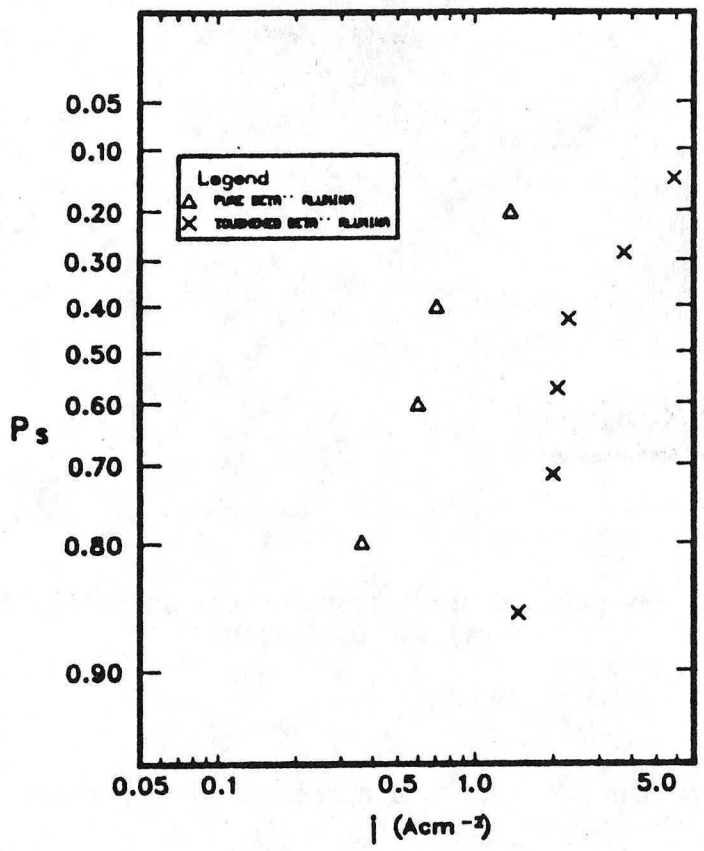

Figure 73. Continuous Acoustic Emission for Normal and Toughened Electrolytes

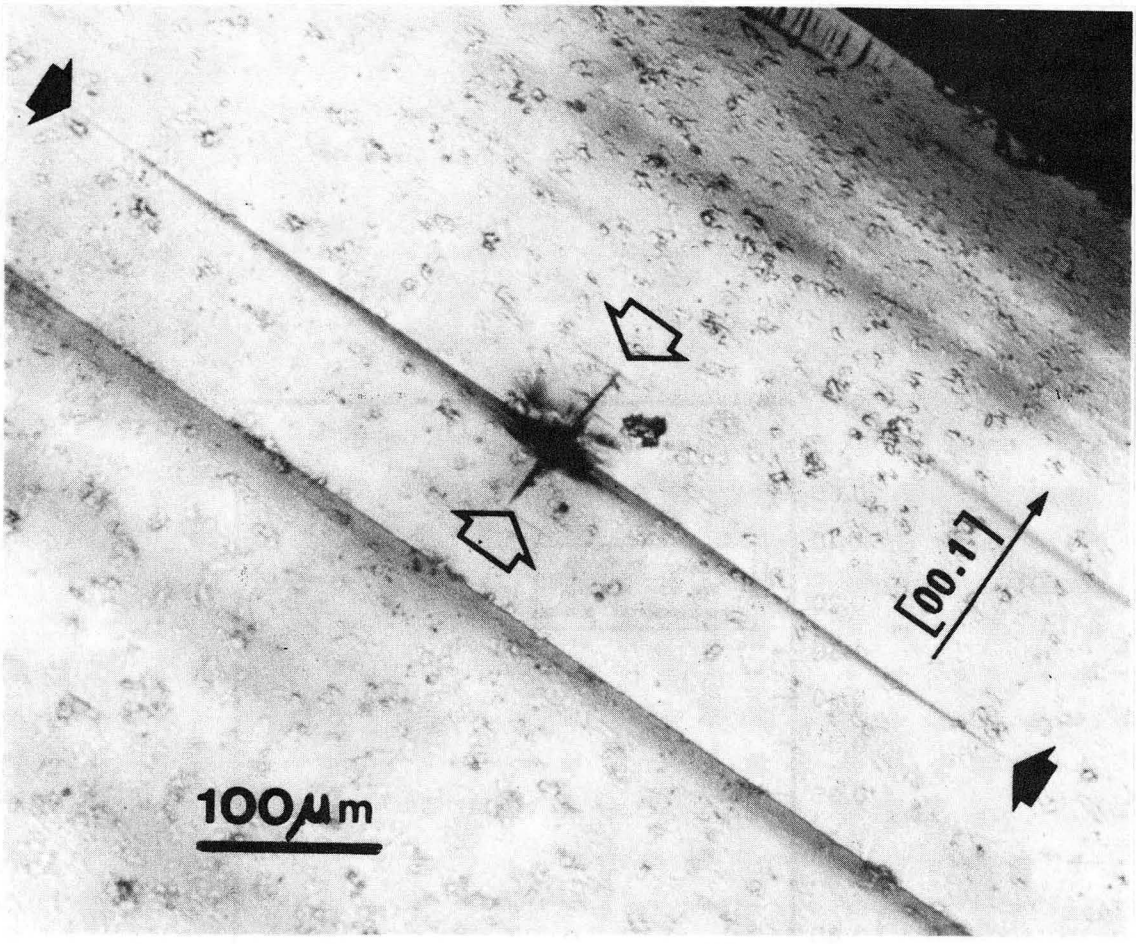

Figure 74. Vickers Hardness Indent and Cracks on (solid arrows) and Perpendicular to (open arrows) the 00.1 Plane

then E was derived from the H/E values and from H. The various values of H/E, H, and E so determined from the prismatic plane surface indents are listed in Table 3-2. The values found for basal-plane-surface indents were about half those found from cracks formed normal to the basal planes-the short cracks in Fig. 74. Because the basal-plane-surface indents exhibited subsidiary cracking, it was felt that the indents on the prism-plane surfaces yielded the significant values of the fracture toughness anistropy. The ratio, E1/E2, of the elastic moduli parallel, E1, and perpendicular, E2, was 1.23. The fracture toughness values were then determined from the measurements of the Vickers indenter cracks produced on prism-plane surfaces and from the values for E1 and E2 listed in Table (3-2); they are

given in Table (3-3). The K_c values for cracks running in the 00.1 direction of the single crystals (Table (3-3) and for polycrystals measured by macroscopic fracture-mechanics methods (10). The K_c values for cracks in the 00.1 planes are a factor of ten lower than these values. When these 00.1 crack values are inserted into the expression describing initial mode I crack growth, values for the critical current dnesities for failure initiation are obtained that agree reasonably well with those reported by Buechele et al (12). It is therefore concluded that mode I crack initiation in sodium-beta and beta" aluminas can occur well below the average values observed for rapid, catastrophic electrolyte failure.

Table 3-2

Values of Hardness and Elastic Modulus
Determined from Surface Indents

Plane of Indention	H/E	H(GPa)	E (GPa)
Basal	0.0632	13.59	215 (E1)
Prismatic	0.0465	8.1	174 (E2)

Table 3-3

Fracture Toughness Values

Material	Plane of indentation	K_c (MPa*m$^{1/2}$)	Std. deviation
Beta Single crystal	Prismatic	0.162	0.067
Beta single crystal	Basal	1.973	0.232
Beta" polycrystal		1.984	0.226

GALVANOSTATIC AND POTENTIOSTATIC MEASUREMENTS

The purpose of the electrochemical measurements was to assess the role of various impurities in the behaviour of the sodium/electrolyte interface. The influence of sodium oxide, water, calcium and potassium were examined. Generally, little effect was noticed at 300° C. At lower temperatures, however, the impurities altered the electrochemical behavior of the Na/electrolyte interface more noticeably.

Acoustic emission studies have evidenced a lower bound of about 150 mA/cm^2 on critical current density for the initiation of Mode I failure. Thus, the 30-50 mA/cm^2 current density region seemed to be a reasonable range to explore first as the phenomena that may occur then could be attributed uniquely to the effect of impurities, without interaction with a possible crack propagation. Nevertheless, tubes needed to be tested up to 100-150 mA/cm^2 in order to observe interesting deviations from the ohmic behavior at higher current densities.

The normal operating temperature of the battery is between 300 and 350° C. However, most experiments were conducted at a lower T (160°C) since lower temperature experiments provided more information regarding the kinetic of the interface processes.

Cells were tested containing added Na_2O, and compared to cells in which no intentional impurities were present. The tests were performed at 350°C and at 160° C. In addition, the effects of H_2O, Ca, and K were examined.

Na/Na tests at 350°C

Pure Sodium: Sodium was electrolysed into the beta-"alumina tubes. The main potential contaminants were oxygen and water. Possible sources of oxygen contamination were the following: H_2O molecules adsorbed on the surface of the

beta-"Al_2O_3 tube, O_2 from the argon atmosphere of the glove box, and Na_2O contained in the sodium of the counter electrode. This latter contribution was negligible compared to the two others because the oxygen partial pressure is very low and therefore the transport of oxygen from the outside to the inside of the tube through the gas phase should be negligible.

In the low current density range (30/40 mA/cm^2) the behavior was strictly Ohmic. For higher current density only two tubes have been tested and will be called α and β in the following. At high scan rates (100 mv-20/sec) the behavior is Ohmic. Fig. 75 and 76 show some deviations from this Ohmic behavior and hysteresis at slower scan rate (1 mV/sec), especially in the case of cell β.

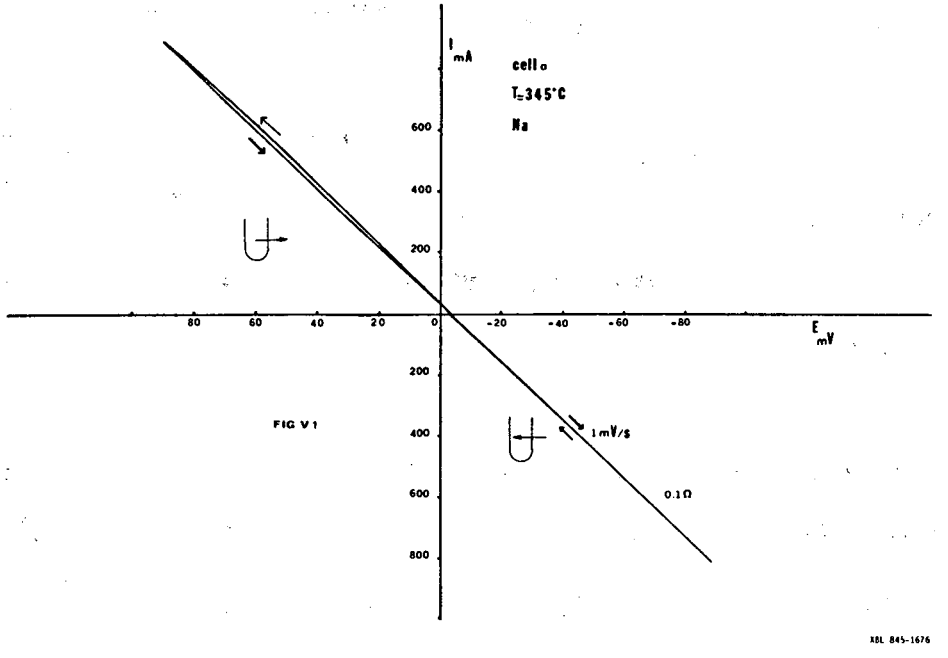

Figure 75. Cell α
Voltammetry Curve at 345°C Electrolytic Sodium

These deviations correspond to a decrease in the interface resistance for fresh sodium flowing in the tube and to an increase in the resistance for sodium flowing out. The range of resistance changes was between 0.04 Ω and 0.06 Ω . It is interesting to point out that the hysteresis, where it appeared, also corresponded to an increase in resistance during discharge (sodium entering the beta "Al_2O_3) as well as to a decrease in the resistance during charging (fresh sodium flowing into polarization or severe asymmetry.

Sodium with sodium Oxide Na_2O (Cell γ): Some anhydrous Na_2O_2 was added at the bottom of the tube prior to any electrolysis. Na_2O_2 converts to Na_2O during the experiment, since $Na_2O_2 + Na = 2Na_2O$. This should result in an increase of the overall resistance, but the shape of the voltammetry curves remained fairly similar to the ones obtained in the case of pure sodium and exhibited less asymmetry than cell β, as shown in Fig. 77.

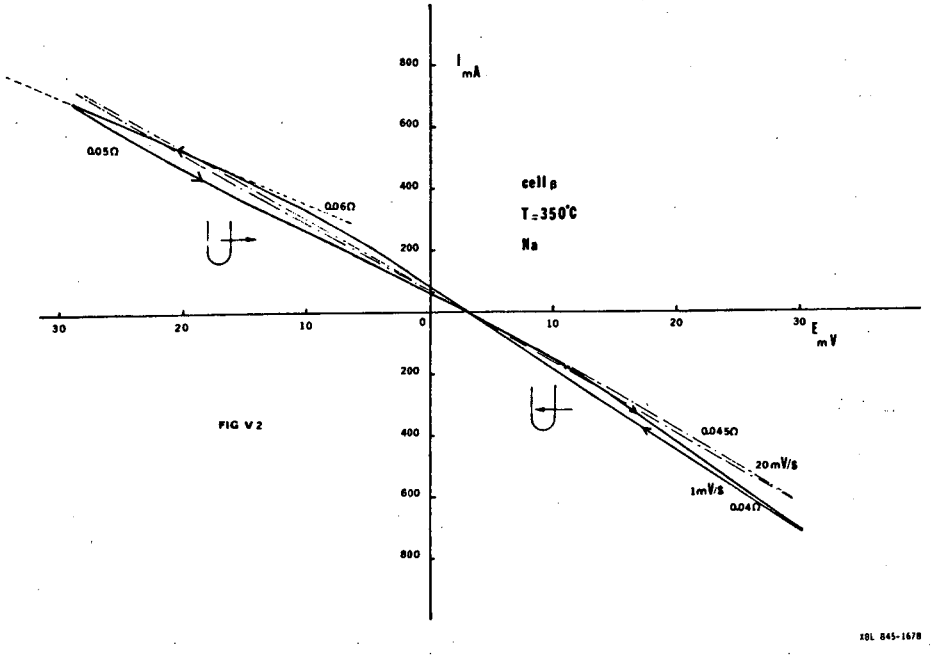

Figure 76. Cell β
Voltammetry Curve at 350°C Electrolytic Sodium

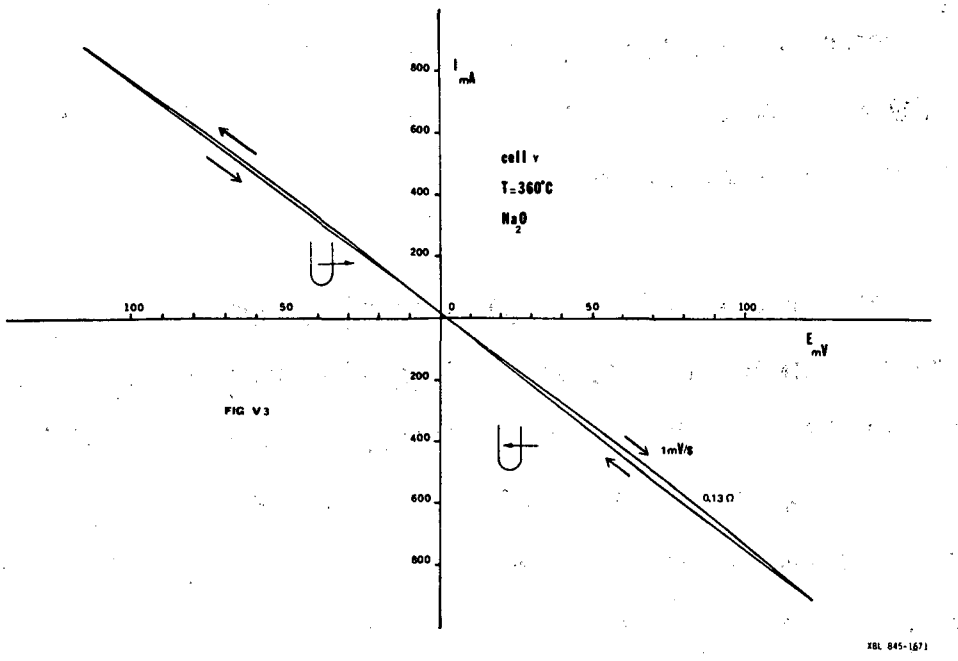

Figure 77. Cell γ
Voltammetry Curve at 360° C Sodium contaminated with Na_2O

In conclusion, at 350°C the shape of the I/E curves did not reveal big differences between Na and Na_2O. The deviations from Ohmic behavior, either hysteresis or asymmetry were slight.

Na/Na Tests at 160°C

The current/voltage relationships obtained in the cases of pure Na, and Na + Na_2O exhibited much higher deviations from Ohmic behavior at 160°C than at 350°C.

"Pure" Sodium: Cells α and β behaved differently from each other. Cell β exhibited the expected behavior: large asymmetry, with the resistance lower when fresh Na flowed out of the tube (for a scan rate of 2mV/sec, R_d = 0.5Ω and R_c =

0.38 Ω), Fig. 78. A time dependence was also observed: the asymmetry is larger for slower scan rates and the resistance for sodium flowing out the tube is higher than the resistance for fresh sodium entering the tube.

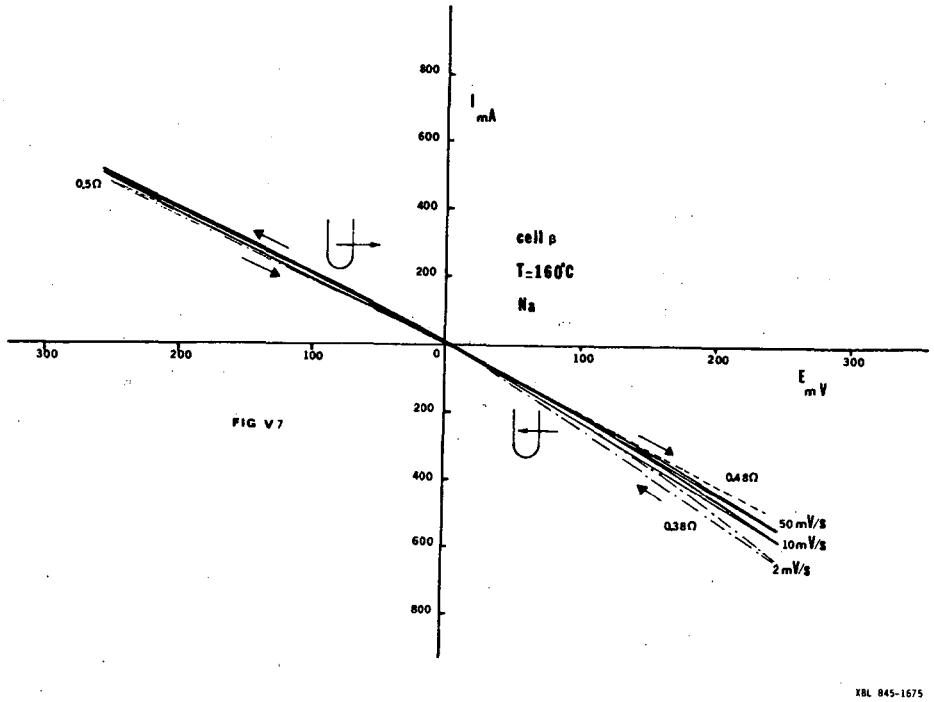

Figure 78. Cell β
Voltammetry curve at 160°C Electrolyte sodium

Cell α exhibited an unexpected behavior (Fig. 79): an increase in the resistance for fresh sodium flowing in the tube, and a decrease (slighter) of the resistance for sodium flowing out. Constant potential pulse measurements with the current recorded as a function of time (Fig. 80), showed that two effects were, in fact, superimposed. While at first, when fresh sodium was flowing in, the resistance increased, it decreased for a higher number of coulombs passed, which was the

expected normal behaviour. When sodium flowed out, the resistance first decreased and then increased again which was also the normal behavior (the curve 500mV(a) corresponds to sodium flowing in the tube, curve 500mV (b) corresponds to sodium flowing out of the tube). The initial decrease is, at present, not understood.

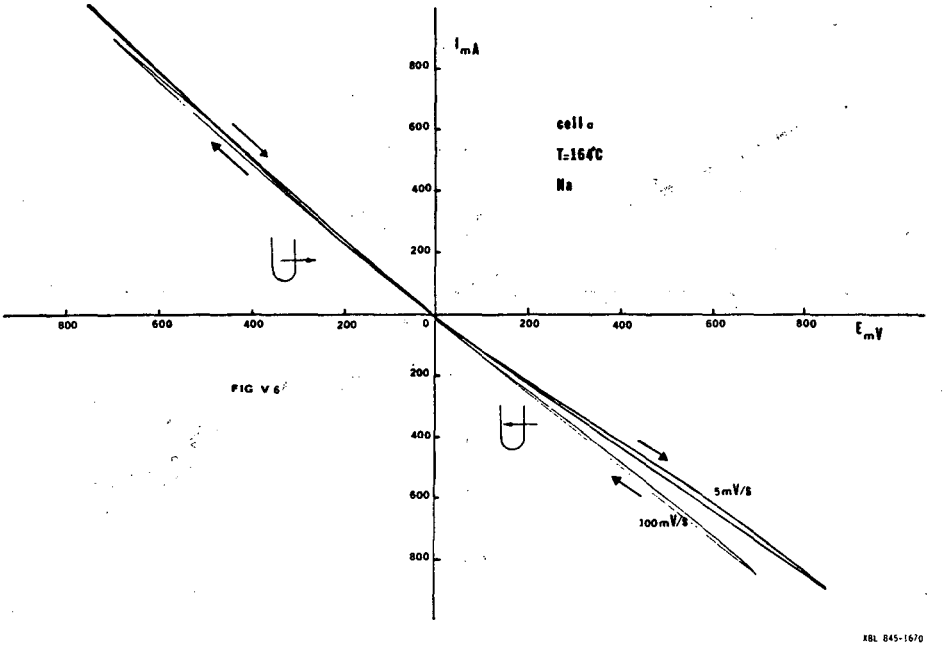

Figure 79. Cell α
Voltammetry Curve at 164°C
Electrolytic Sodium

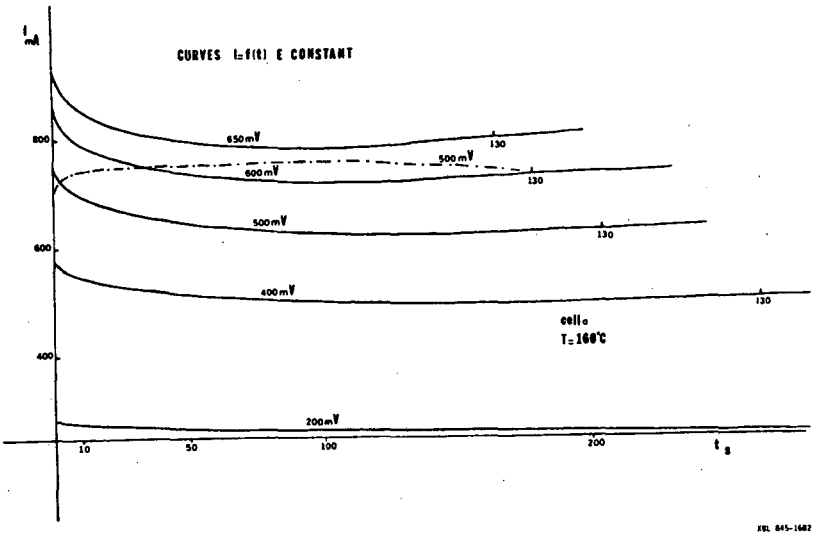

Figure 80. Cell α
Constant Potential Pulse Measurements

Na_2O: The presence of Na_2O first accentuated the asymmetry already encountered with "pure sodium". The resistance was higher for Na flowing towards the interface than for sodium flowing away from it. Here, a time dependence, was observed with larger asymmetry for slower scan rates, Figure 81, 82 and 83. The ratio R_d/R_c was equal to 1.9 at 240°C and 2.6 at 160°C. Thus, Na_2O causes a significant asymmetry.

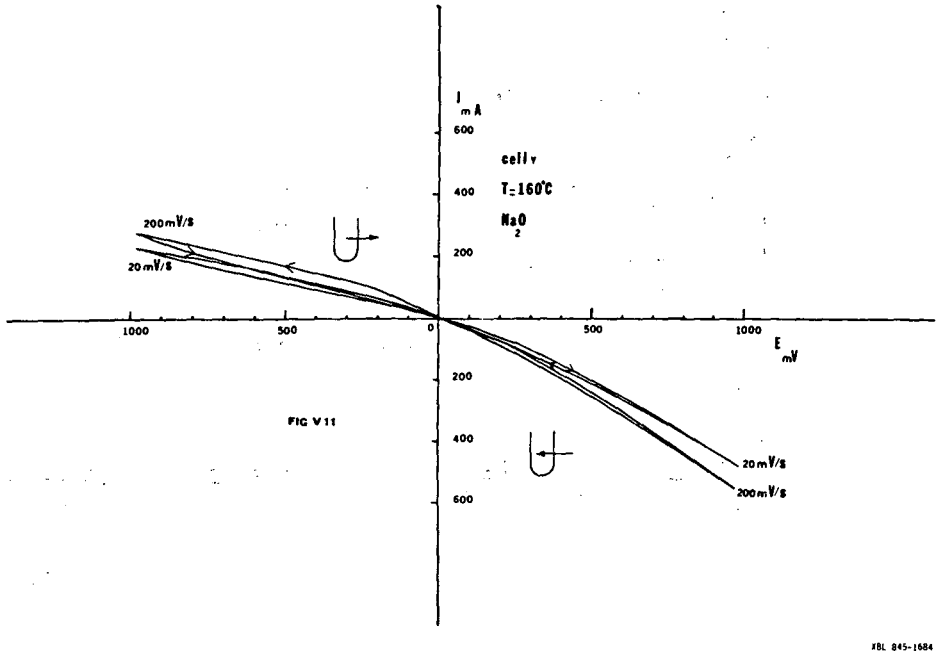

Figure 81. Cell γ
Voltammetry Curve at 160°C Sodium Contaminated with Na_2O

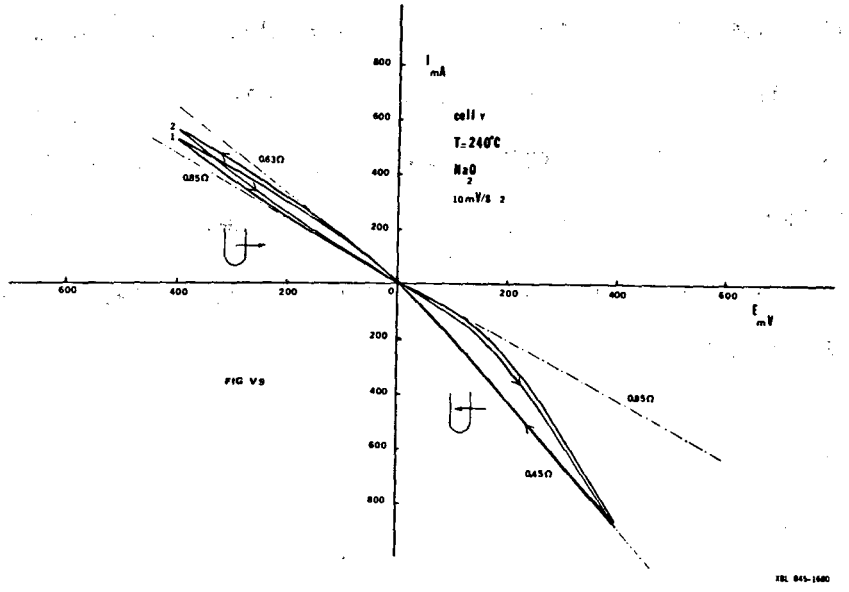

Figure 82. Cell γ
Voltammetry Curve at 240°C
Sodium Contaminated With Na_2O
(to be compared to 83)

The curve showing $\Delta I = f(E)$, Fig. 83, obtained by suppressing the main Ohmic contribution, evidences even more clearly the asymmetry and the time dependence effect, compared to Fig. 81 showing data for the same cell (cell γ) at the same T.

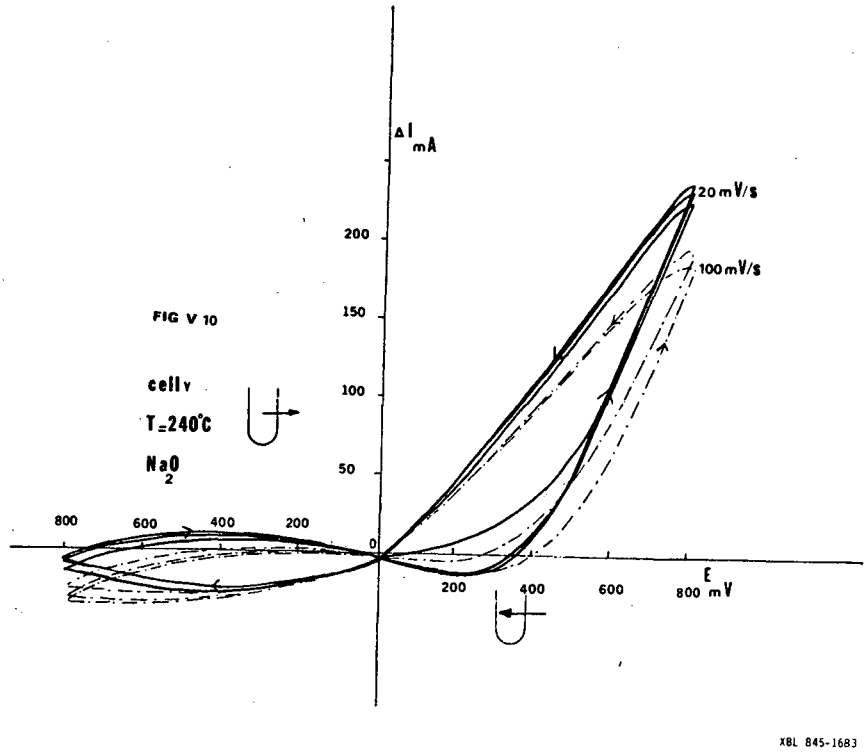

Figure 83. Cell γ
ΔI vs E Curve at 240°C
The Main Ohmic Contribution is Suppressed

Water: To study water contamination, the usual three electrode electrochemical setup was used. This procedure introduced an ohmic drop of the order of 0.03Ω was was at the working electrode, which may have concealed slight deviations from the ohmic behaviour. Nevertheless, the study at low T is valid as the resistances involved were much higher (1-2Ω).

The Na-beta"-Al_2O_3 tube was exposed to air for three weeks. Some problems were encountered with the reference electrode which seemed to suggest a partial failure or dendritic penetration by Na on the inside interface, in a Mode I fashion, had occurred. However, after dismantling the cell, no cracks could be found.

At 350°C, an Ohmic behavior was observed for both interfaces. At about 160°C deviations very similar to the ones obtained in the case of the oxygen alone were evidenced on the outside interface, Figure 84.

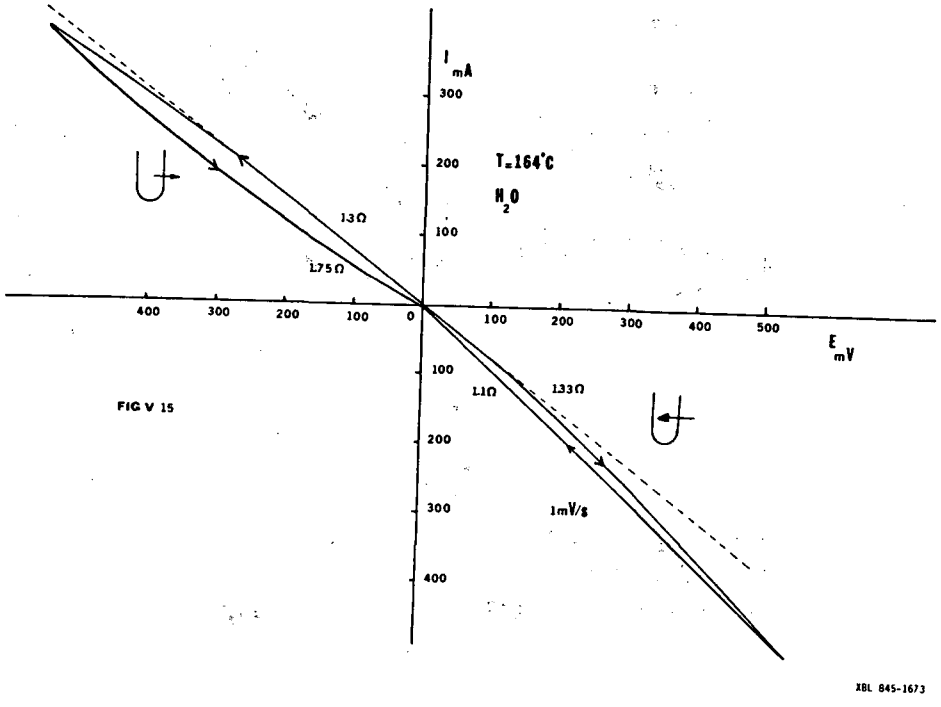

Figure 84. Voltammetry Curve at 164°C
Water Contaminated Tube

With the restriction that only the outside interface could be studied, the low T experiments show a type of polarization very similar to the one due to Na_2O only, Fig. 83. The sodium of the outside compartment contains some Na_2O, therefore the only conclusion that can be drawn is that the presence of water doesn't introduce

very significant changes with respect to Na_2O alone as far as the polarization curves are concerned.

However, the severe darkening undergone by the tube shows that a significant degradation process has taken place. Fig. 85 shows beta-"Al_2O_3 tubes of cells contaminated by KCl, H_2O, CaO, $CaCl_2$ and Ca. The tube that has been water contaminated appears almost black without staining with $AgNO_3$. The cross section of the tube shows that a more intensely darkened layer has also developed near the surface, Fig. 86.

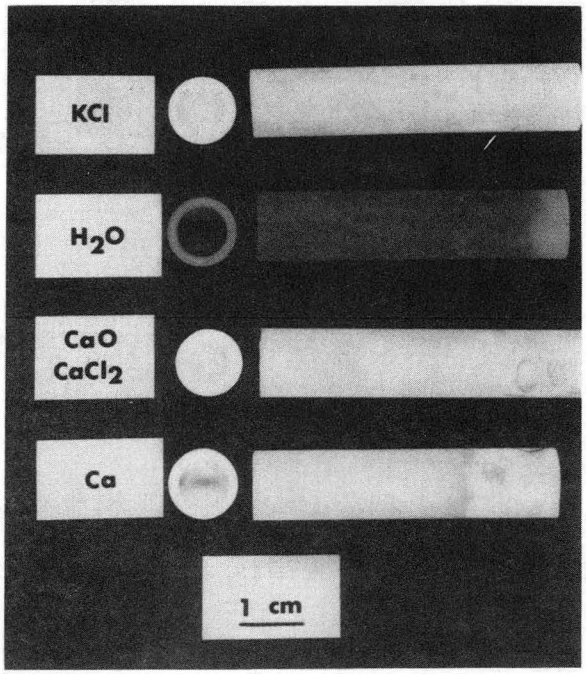

Figure 85. Beta" Alumina Tube After Testing

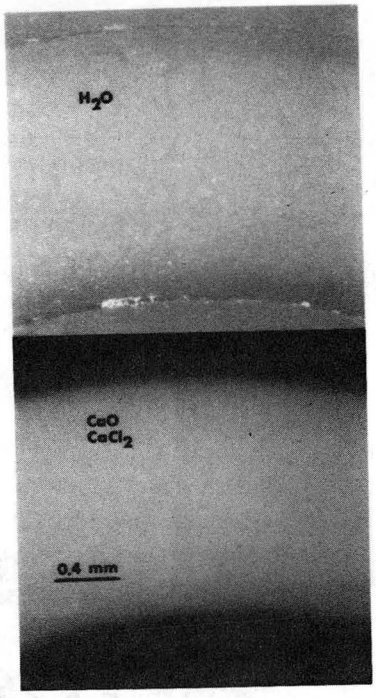

Figure 86. Cross Section of Beta" Alumina Tubes Contaminated Respectively by H_2O and CaO $CACl_2$

Other Impurities - Ca, K: The influence of Ca in different forms was investigated: CaO, $CaCl_2$ and Ca metal. Potassium was introduced in the form of KC . Only partial can results be reported here.

CaO: CaO was added at the bottom of the tube prior to any electrolysis. I/E curves at 350°C showed an ohmic behavior, the expected larger increase in the resistance was not observed, even when the cell was left several days without passing any current or was cycled at low current density. The tube didn't fail.

CaCl : As CaO didn't prove to have any noticeable effect, some CaCl was added in the same cell. No increase in resistance was evidenced. The same kind of problem

with the reference electrode as for the water contaminated cell was encountered. No cracks were found on the tube, Fig. 86.

Ca Metal: Some pellets of Ca metal were added with chunks of sodium of the same purity as the Na used in the outside compartment. The tube was not filled electrolytically. No significant increase in the resistance was observed while the cell was cycled and the tube did not fail. At 350°C the cell exhibited an Ohmic behavior.

KCl: Some KCl was added inside the tube but also in the outside compartment so that its influence can still be studied on the outside interface in case of a problem with the reference electrode, which appeared to be the case. At 350°C, an ohmic behavior was observed on both interfaces. At 160 C I/E curves presented an asymmetric behavior very similar to the one observed in case of water contamination.

MOBILE OXYGEN INTERSTITIALS

Sodium-beta alumina single crystals with dimensions of about 2x2x5mm were immersed in molten sodium at 350°C for 165 or for 266 hours. This experiment was carried out in a glove box, under purified argon with less than 5 ppm oxygen. The molten sodium showed formation of an oxide layer, indicating that the oxygen fugacity in the metal melt should be at the Na_2O/Na equilibrium of about 10^{-55} atm. After this exposure to molten sodium the chemical coloration extended throughout the samples.

The chemically colored samples were bleached in air at 250, 300, 350, and 400°C. Due to the very limited availability of large single crystals only a limited set of experiments could be performed. After the bleaching treatment, the Na ions in the crystals were exchanged with molten $AgNO_3$, 300°C, for about 20 minutes. The

silver exchange strongly enhanced the remaining coloration thus facilitating the optical measurement of the bleached layer thickness. Some samples were given a dual bleaching treatment: 24 hours at 350°C followed by 72 hours or 125 hours at 250 or 300°C.

An example of a partly bleached single crystal is shown in Fig. 87. The crystal coloration has been enhanced by silver staining. The c axis is normal to the paper. The bleached layer is very discrete. Such discrete layers are typically formed as a result of the elimination of color centers when the recombination rate of the neutralizing defect with the color center is fast compared to its transport rate. The bleaching kinetics are parabolic as shown earlier (7).

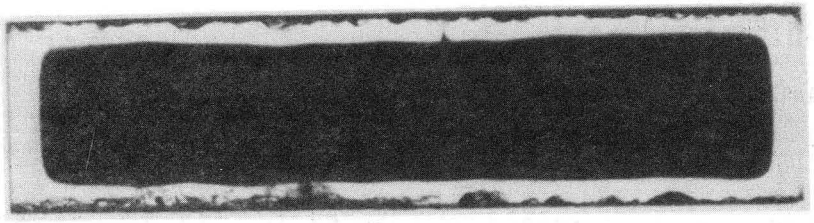

1.0 mm

Figure 87. Partly Bleached Single Crystal
Formation of a Discrete Bleached Layer

The anomaly in the bleaching kinetics is evident from a comparison of the reaction rate constant k, calculated with Eq. 3-14, from isochronal bleached layer thicknesses as a function of temperature, Fig. 88. The bleaching rate is maximum around 250°C and minimum around 350°C.

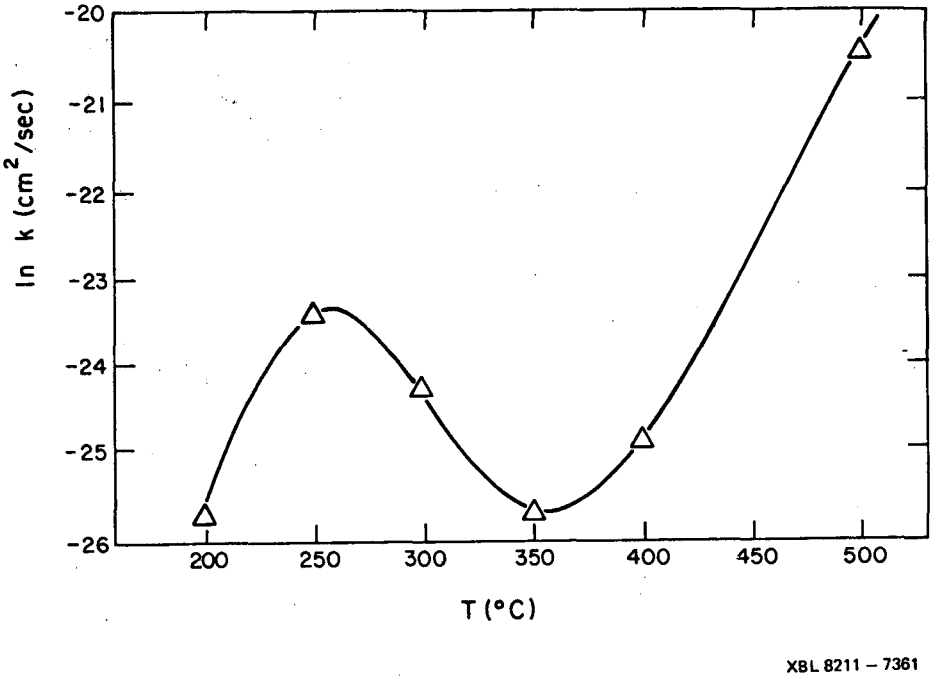

Figure 88. Rate Constant of Bleaching vs Temperature

The bleaching kinetics appear to be dependent on the chemical coloration treatment: crystals immersed in sodium for a longer time bleach slower. This is shown in Fig. 89, where bleaching rates after a 165hr coloration treatment (solid lines) are compared to those after a 265hr treatment (dashed lines). This result is expected if the equilibrium coloration defect concentration is not achieved rapidly, possibly due to a slow surface step.

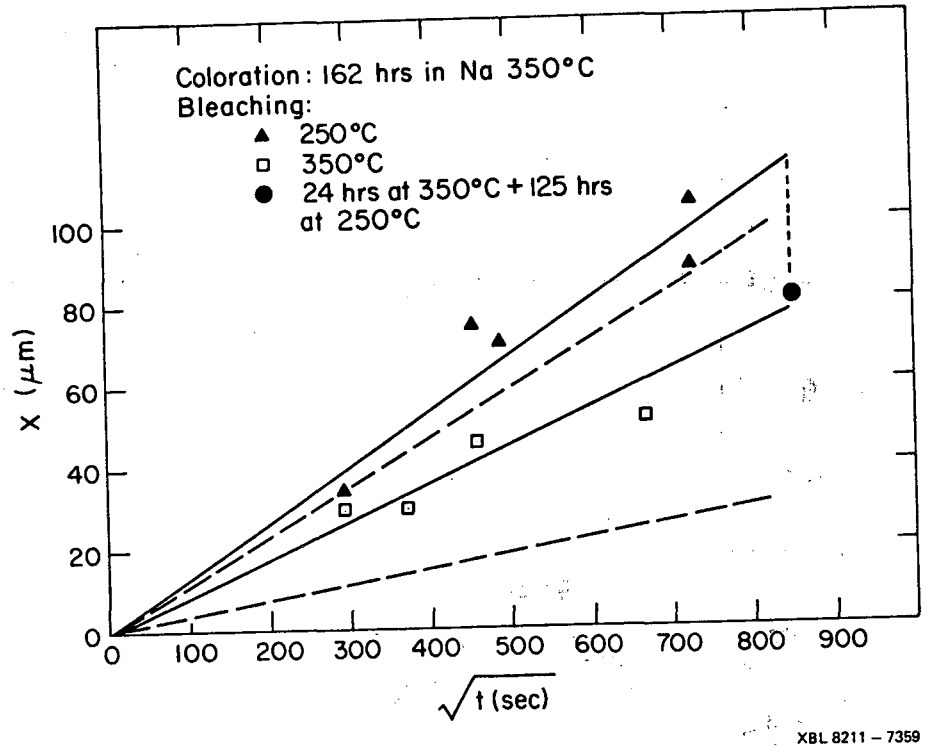

Figure 89. Bleached Layer Thickness vs Time
162 hrs in Na at 350°C

As discussed earlier (7) the bleaching is a reoxidation process. Thus, during bleaching, oxygen ions diffuse into the crystal while electrons are transported out. Electroneutrality requirements will couple the fluxes. Additionally, highly mobile Na^+ ions will screen completely the electrical field that would otherwise arise. To find which species dominates the bleaching kinetics, the transport equations need to be considered and reasonable estimates of the coloration defect density need to be made. The transport equations describing the coupled fluxes of electrons and oxygen ions are in the absence of an electric potential gradient:

$$J_e = -1/2\ J_i = -\ (\sigma_e/F^2)\nabla\mu_e \qquad (3\text{-}8)$$

and

$$J_i = -(D_i C_i/RT)\nabla\mu_i \qquad (3\text{-}9)$$

where J_e = electron flux, J_i = oxygen ion flux, σ_e = electronic conductivity, F = Faraday constant, D_i = oxygen ion diffusion constant, R = gas constant, T = absolute temperature, μ_e and μ_i = chemical potentials of electrons and oxygen ions, C_i = mobile oxygen ion concentration.

Remembering that

$$\frac{1}{2}\mu_{O_2} = \mu_i - 2\ \mu_e\ , \qquad (3\text{-}10)$$

Eqns. 3-8, 3-9 and 3-10 lead to:

$$J_i = -\ [\sigma_e D_i C_i/(D_i C_i F^2\ +\ 2\ RT\ \sigma_e)]\ \nabla\mu_{O_2} \qquad (3\text{-}11)$$

This flux will be controlled by the oxygen ion transport rather than by electrons, if:

$$D_i C_i F^2\ \ll \sigma_e RT \qquad (3\text{-}12)$$

Here, C_i is the concentration of all mobile oxygen which, in the bleaching below 400°C, is confined to the conduction planes (7). This puts C_i at about 3.3×10^{-4} moles O_2/cm^3 for the present crystals that have an overall composition of 1.25 Na_2O.11 Al_2O_3. The value of σ_e is about 10^{-15} $(cm)^{-1}$ at 300°C (16). Thus, for Eq. 3-2 to be valid, one should satisfy

$$D_i \ll \sigma_e\ RT\ C_i F^2 = 1.6\times10^{-10}\ cm^2/sec \qquad (3\text{-}13)$$

An estimate of the upper bound on D_i can be obtained from the scaling constant, k. From the parabolic bleaching rates one may write:

$$dx/dt = k/x \tag{3-14}$$

where x is the bleached layer thickness. Also,

$$J_i = C_D dx/dt \tag{3-15}$$

where C_D is the total concentration of coloration defects. Since a weight change could not be detected after coloration or bleaching, the maximum value of C_D is about 10^{-3} weight fraction, or about 1×10^{-5} moles O_2/cm^3. Thus, with $k = 2 \times 10^{-10}$ cm^2/sec at 250 C:

$$J_i \; x \leq 2 \times 10^{-15} \text{ moles/cm sec.} \tag{3-16}$$

Integration of Eq. (3-14) over the bleached layer thickness, ℓ, assuming that Eq. (3-15) is valid and further assuming that σ_e, D_i and C_i are about constant within the bleached layer leads to:

$$D_i = - \frac{J_i \ell RT}{C_i} (\Delta\mu_{O_2})^{-1} \tag{3-17}$$

where $\Delta\mu O_2$ is the oxygen chemical potential difference between the surface and the coloration interface at $x = \ell$. This $\Delta\mu O_2$ should corespond to the oxygen fugacity difference between air and the Na/Na_2O melt. Thus

$$\Delta\mu = RT \; \ell n \frac{P_{O_2}^{\,x = \ell}}{P_{O_2}^{\,x = 0}} = RT \; \ell n \; 10^{-55} \tag{3-18}$$

Putting the values of the respective parameters into Eq. 3-17, it is found that

Thus, the upper estimate to D_i is 3 to 4 orders of magnitude lower than required by Eq.3-13 for oxygen ion diffusion controlled bleaching kinetics. The anomalous

bleaching kinetics must therefore be understood in terms of changes in the transport mechanism of the oxygen ions in the conduction planes.

The results of the dual bleaching treatments are also shown in Figs. 89 and 90. After bleaching for 23 hrs at 350°C in air followed by bleahing for 72 hr at 250° C, the total equivalent time at 250°C, t_{250}, is obtained from:

$$t_{250} = 72 \text{ hr} + t_{250}\, k_{350}/k_{250} \qquad 3\text{-}20$$

Where t_{350} = 24 hr, and k_{350} and k_{250} are the scaling constants at 350 and 250°C in Eq. (3-14). It is seen that the bleached layer thickness is significantly less than expected from a reversibility postulate. Similar results of dual bleaching experiments are included in Figs. 89 and 90. It must thus be concluded that the changes in the bleached layers above 300°C are irreversible.

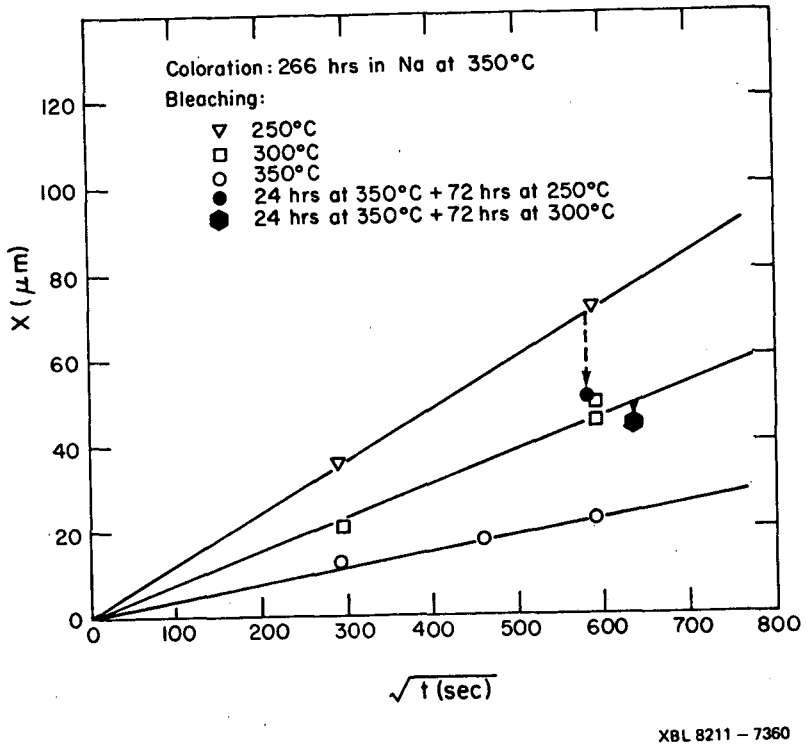

Fig 90 Bleached Layer Thickness vs Time
266 hrs in Na at 350°C

The above results can all be interpretated simply if it is assumed that the transported species are oxygen interstitials. In the coloration process a number of these interstitials get removed, permitting the recombination of the $V_{Al}''' - Al_i'''$ defect pairs associated with the Roth oxygen interstitial configuration (17). When oxygen interstitials are reintroduced in the bleaching process, they should have a high mobility if they are not bound by the $Al_i''' - V_{Al}'''$ Frenkel pair. The bleaching rate anomaly data would then indicate that in sodium-beta alumina the conversion of free oxygen interstitials to bound oxygen interstitial occurs between 300 and 350°C.

It is interesting to note that in Na-beta"-alumina conduction plane oxygen interstitials are not present, and one should therefore expect slower bleaching kinetics. This is indeed observed (11).

INTERFACE RESISTANCE

The surface overpotential, derived from the measured difference of the low frequency AC measurements and the DC conductivity, was plotted versus the current, and the slope of this plot gave the Na/ electrolyte overpotential. A value of 9.5×10^{-7} ohm.m^2 was measured with a rather large experimental uncertainty of (+/-) 5×10^{-7} ohm.m^2. This low value of the interface resistance is not in agreement with what has been reported elsewhere. It is possible that the frequency of the AC measurements was insufficiently high to exclude all interface contributions, since the AC method could not be used above a few hundred Hz due to line inductances. Furthermore, the method would not detect a surface layer that behaves purely ohmicly in the frequency domain tested. The measured surface resistance is probably due to accumulation of impurities, such as Na_2O, at the Na/electrolyte interface, and the reduction-oxidation reaction of sodium at this interface is not expected to lead to any measurable interface effects.

Section 4

DISCUSSIONS AND INTERPRETATIONS

EVIDENCE FOR SLOW DEGRADATION

In various experiments, as well as in practice, it is observed that electrolyte failure does not occur instantaneously, but rather develops after some incubation period. The evidence found in the present work is most clearly seen in the dependence of the critical current density for failure initiation on the rate at which the current density is increased. Such tests are equivalent to the application of an increasing mechanical stress in fracture mechanics experiments, where a dependence can be interpreted as an indication of slow crack growth. The same interpretation applies here. Occasionally, microstructural features are found in used cells suggesting that a crack has propagated at subcritical velocities. This can be deduced from the darkening profile that surrounds a crack in an electrolyte. The darkening is known to proceed with a parabolic time dependence, although the rate constant is material specific. If the darkening rate constant has been determined for the specific electrolyte and temperature, then analysis of the discoloration profile around a crack can both indicate when the crack started during the cell operation, and what its approximate velocity was. An example of a crack that apparently did not propagate at a uniform rate is shown in Fig. 21 observed in an electrolyte tested by BBC. The staining profile is clearly wider on the sodium side of the crack. This cell was tested at a charging current density of 75mA/cm^2. The crack velocity derived form the staining profile is shown as a function of crack length in Fig. 88. It can be seen that at constant current density the crack velocity was not uniform. Apparently, the crack moved forward, and then was arrested for some time, and then moved again.

A second slow degradation process is evident in the "extra-darkened" layer that is observed to develop on the sodium exit side of many tested electrolytes, as described in this report.

Attempts were also made to get cracks to grow subcritically in laboratory tests. Cracks could be initiated by drawing a small current through the electrolyte with the touching molydenum electrode, below the melting point of sodium. Attempts were then made to extend this crack subcritically above the melting point of sodium. The experiments proved to be difficult, and only incomplete data on crack rate extension could be collected. Part of the difficulty is the locating of the crack by cutting and polishing of the electrolyte. The results of these tests were inconclusive. So far, all the experiments point to the crack spending most of its slow growth process in the very early stages, the initiation stage, when it is still very small.

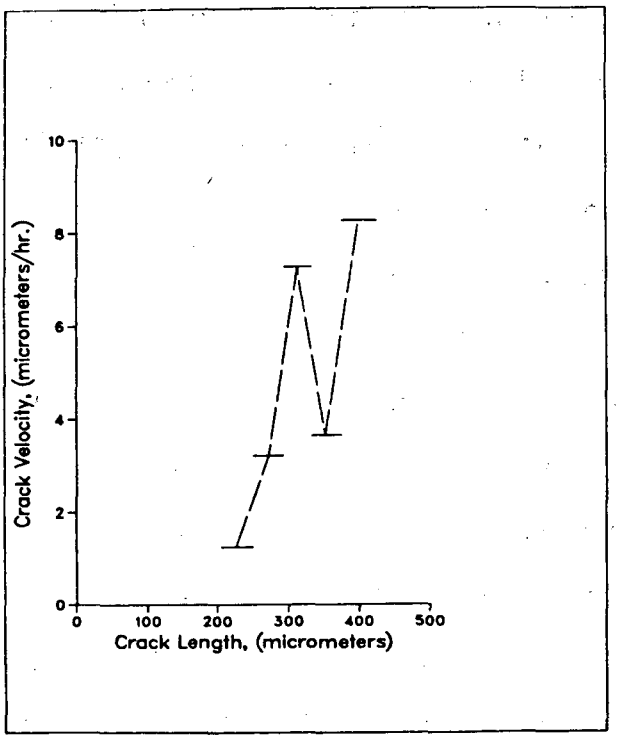

XBL 845-2003

Figure 91 Crack Velocity vs. Crack Length

EFFECT OF APPLIED STRESS

It is expected that mechanical stresses may be superimposed on the electrolyte tubes during the cell functioning. These can arise from cell assembly or from cell operation. Therefore, the sensitivity of the critical current density for failure initiation in the presence of an applied stress needs to be considered.

In a first approximation one can consider the crack opening displacement to be constant, for a given electrolyte, when the stress intensity factor has reached the critical value, for a fixed flaw length. If the crack opening displacement is fixed, then the stress intensity generated by the Poiseuille flow of sodium through it is simply proportional to the first power of the current density, i

$$K_I = fr^{-3}\, i \qquad (4\text{-}1)$$

where K_I is the stress intensity due to the Poiseuille flow, f is a constant for fixed flaw length, and r is the crack opening displacement. For a given stress intensity generated by sodium flow in this crack, the remaining stress intensity is then provided by the mechanical stress, to reach the critical condition. This leads to the equation

$$K_{Ic} = K_I = K_I \qquad (4\text{-}2)$$

where K_I is the stress intensity due to mechanical stress. Combining equation (4-1) with (4-2), gives

$$K_{Ic} = i_{cr}(S/i_{cr}(0) = K_I \qquad (4\text{-}3)$$

where $i_{cr}(S)$ is the critical current density in the presence of an applied stress, and $i_{cr}(0)$ is the critical current density with no stress. Applied stress is therefore reduce the critical current density of the electrolyte. It can be seen that statistically frozen-in, local stresses, such as result from the anistropy of

the thermal expansion of the electrolyte grains, could strongly affect the local condition for failure initiation. This would lead to a requirement of fine, equiaxed grain size and for a careful post-sintering stress annealing procedures to achieve high Weibull moduli for failure initiation.

CURRENT DISTRIBUTION ON A SODIUM-FILLED CRACK

The primary current distribution on a Na-filled crack in the electrolyte has previously been calculated,(12) but for small objects the current distribution tends to be uniform, so the primary current distribution is not a good approximation. The secondary current distribution was calculated numerically for a crack 10 microns long, with a surface resistance of 10^{-6} ohm.m^2 and electrolyte resistivity of 0.04 ohm.m by a method similar to that used by Parrish and Newman. (14) The results are compared to the primary current distribution in Figure 89. The current density at the crack tip is 1.1 times the average current density on the electrode, compared to about 10^4 for the primary current distribution. The total flux of Na in the crack is 0.84 times the flux for the primary current distribution.

It is thus clear that consideration of the actual current distribution on the sodium filled crack, taking into acccount the effects of interface overpotentials, lead to significantly larger deviations of the actual and the calculated critical current densities based on the simple, unmodified Poiseuille pressure argument. Although some recent three-dimensional calculations by Virkar et al. (3) have moved the calculated critical current densities to values comparable to those that are actually observed, taking the secondary current distribution into account would again lead to a much higher calculated critical current density. This consideration as well as the observation of the evidence for additional chemical

interface that appear to lead to degradation, strongly suggest that the Mode I models need to be modified to include such effects.

PROOF TESTING

Acoustic emmission testing where the rate of the current density is varied, and microstructural examination of used electrolytes indicated that some form of electrochemical attack is involved in the electromechanical failure, (12) while strictly mechanical tests of beta" alumina in molten sodium do not indicate the presence of subcritical crack growth. (10) Thus, mechanical and electromechanical failure are not equivalent. Nevertheless, it is useful to discuss briefly the significance of Eqns. 3-1 and 3-2 in the context of the present finding on the statistical distribution of the failure initiation current densities.

The particular dependence of i_{crit} on K_{IC}, (4) permit a comparison of the mechanical reliability, expressed by m in Eq. 3-2 and electrical reliability expressed by n in Eq. 3-1. It follows from Eq. 3-1, 3-2 and 4-4 that m = 4n. If, for example, one would operate a tube at a current density i_{op}, which is a factor B below the 50% failure probability current, i_{50}, then one could specify n, and, hence, m, for a particular level of required survival: P_R. Assuming that the survival probabilities, P_s, pertain to tests for which the electrode current distribution is uniform and $i_u = 0$, manipulation of Eq. 3-1 leads to

$$n = \left(\ln \ln \frac{1}{P_R} - \ln \ln \frac{1}{0.5} \right) / \ln B \qquad (4\text{-}5)$$

Table 4-1 lists some examples for m and n, calculated with Eq. 4-5, when B is 10, 5, or 2, and P_R is 0.95 or 0.99. It is evident from this table that the requirements on reproducibility of mechanical properties of large electrolyte tubes would become very stringent if $B = i_{50}/i_{op}$ becomes less than 5, and an

initial crack initiation level of less than 5% cannot be tolerated. Alternatively, one might eliminate the weaker electrolyte tubes by subjecting them to a uniform mechanical proof stress, σp, related to the average fracture strength, $\bar{\sigma}$, by

$$\left(\frac{\bar{\sigma}}{\sigma p}\right)^{4n} = -\ln P_R / \ln 2 \qquad (4\text{-}6)$$

The considerations are analogous to those of mechanical proof testing (8) and follow from combining Eq. 3-1, 3-2, and 4-5 with the assumption that = 0. Proof stress testing of electrolytes has also been proposed by Virkar (15). The present discussion clearly points out what is required of the electrolyte tubes if mechanical and electrical failure were identical. In the case where n, B, and P_R are fixed by materials and economic operating conditions, then a mechanical or electrical proof testing would be a necessity when as follows from Eq. 4-5.

$$|\ln B| < \left| \ln \ln \frac{1}{P_R} - \ln \ln \frac{1}{0.5} \right|^n \qquad (4\text{-}7)$$

Equation 4-7 is represented graphically in Fig. 92 for survival probabilities between 0.800-0.999. Each line of constant P_R separates domains of n and B values in which proof testing is or is not necessary. Since actual ceramics have m (Eq. 3-2) range between 5-20, with m = 10 a common value for reasonably well prepared ceramics, one should expect n to be in the neighborhood of 2 or 3, as appears to be the case in the present tests. For a 99% absence of crack initiation events, Fig. 92 then indicates that B should be between 5 and 10. Since the Na/S batteries are usually operated around 80-100 mA/cm^2, this would have to put the average Mode I failure initiation around 1 A/cm^2. The experiments, showed an average Mode I initiation threshold near this value. Requirements of a low incidence of crack initiation event probability would, therefore, appear to require either electrical or mechanical proof testing. The most reliable method for proof testing would in fact be one in which the Weibull parameters n and m, and the average failure current density, i_{50}, and average fracture stress, σ, are

determined on electrolyte specimens that are indentical to those used in the batteries. The mechanical testing would be one in which the entire tube is stressed uniformally, so that extrapolation of data is minimal.

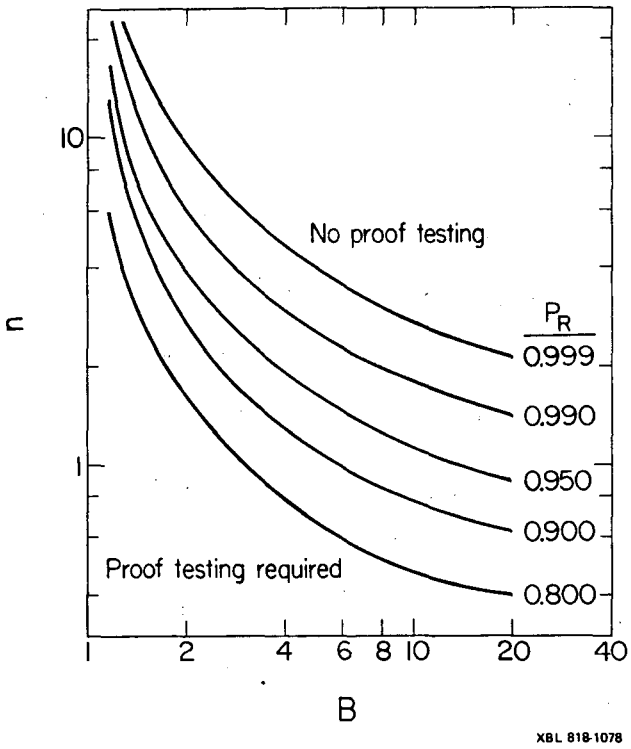

Figure 92. Proof Testing

Table 4-1

B	P_R = 0.95		P_R = 0.99	
	n	m	n	m
10	1.1	4.4	1.8	7.2
5	1.6	6.4	2.6	10.4
2	3.75	15.0	6.1	24.0

A first point that must be emphasized is that the above considerations are only valid under the conditions of strict equivalence of mechanical and electrolytic failure. While all our observations seem to indicate that such equivalence does not fully prevail, it should be stressed that the mechanical properties strongly affect the electrical ones. Since the exact correspondence has not yet been established, we should take the above considerations only as a possible worst case, underscoring the necessity for collecting statistical data on full or nearly full scale cells.

A second point that needs some discussion is the definition of electrolyte failure. While the electrolytes used in Na/S cells and so far examined in this laboratory nearly all showed some Mode I cracks, even after relatively short use (~20 A-hr cm^{-2}), many are known to function with virtually no detectable deterioration in cell performance for extended periods. Thus, the critical current density thresholds reported here use a different failure initiation definition than a battery developer would. Typically, a technological definition uses the appearance of a specified level of nonfaradaic behavior as a failure criterion. Non-faradaic currents in Mode I failure are the result of electronic shorting through the sodium filled crack. In laboratory Na/Na cell tests, this is manifested by an abrupt voltage drop at constant cell current. These abrupt voltage drops were also observed in the present experiments but they occurred at average current densities of around 1-1.5 A cm^{-2}. The electronic shorting was in most cases only partial, and the apparent cell resistance change in many cases would be no more than 10%. The correlation between Mode I initiation in laboratory test such as reported here and technologically meaningful electrolyte failure in an Na/S cell is, therefore, not yet established. However, the present experiments could be considered suitable for comparison of the effects of microstructure, and for the evaluation of the adequacy of models proposed for the initiation current density thresholds of Mode I degradation.

Section 5

CONCLUSIONS

Most electrolytes tested in Na/S cells for 600Ah/cm^2 showed evidence of sulfur side degradation. This degradation did not penetrate through the electrolyte, but could be important when long cell lifetimes are required.

Some, but not all used electrolytes exhibited Mode I cracks penetrating through the electrolyte. At high current density, Mode I cracks resemble mechanical cracks. In some cells, operated for longer periods of time, material appears to have been removed chemically from inside Mode I cracks.

A degraded layer forms in many cases on the sodium exit surface of electrolytes. Grain boundaries are attacked, and electrolytes with a degraded layer at the surface tend to have more Mode I cracks. Microcracks in this surface layer, particularly at the boundary of large grains, are likely sites for Mode I initiation.

Acoustic emission studies indicate that some degradation occurs at low current densities, on the order of a few hundred mA/cm^2. The current densities at which degradation begins are lower if the rate of increase of current density is less, indicating the occurrence of a slow crack propagation phase.

Because of the large fracture toughness anisotropy of beta" alumina, cracks can propagate through favorably oriented grains or grain boundaries at low stress intensity or current density.

Toughening of the electrolytes by a dispersion of fine zirconia particles enhances the critical current density for Mode I failure initiation.

Oxygen interstitials can be transported, as shown by coloration/bleaching experiments. A rate anomaly in the bleaching rate may be attributed to a change in the nature of the interstitials.

Oxygen and water appear to lead to high Na/beta" electrolyte interface resistances. These become more significant at temperatures below 300° C.

Section 6

REFERENCES

1. R. D. Armstrong, T. Dickinson and J. Turner, Electrochem. Acta, Vol. 19, 187 (1974).

2. D. K. Shetty, A. V. Virkar and R. S. Gordon, "Electrolytic Degradation of Beta"-Alumina", 651-665 in Fracture Mechanics of Ceramics Vol. 4, ed. R. Bradt, D. P. H. Hasselman and F. F. Lange (Plenum, 1977).

3. L. Viswanathan and A. V. Virkar, J. Mater. Sci., vol. 17, 753-59 (1982).

4. A. V. Virkar and L. Viswanathan, J. Mater. Sci., vol. 18, 1202-1212 (1983).

5. Breiter and B. Dunn. Time Dependence of the Asymmetric Resistance of Polycrystalline B"$Al_2O_3$3. Electrochem. Acta vol. 26, no. 9, p. 1247, (1981).

6. Electrochemistry of solid electrolytes, 1978. Izdatel ' stvo "khimiya" Moscow.

7. L. C. De Jonghe and A. Buchele, J. Mater. Sci., vol. 17, 885-92 (1982).

8. B. R. Lawn and T. R. Wilshaw, "Fracture of Brittle Solids" (Cambridge University Press, 1975).

9. D. J. Green, "Improved Beta"-Aluminum Oxide Electrolytes Through Transformation Toughening," Final Report Draft for the period July 1, 1983 through June 30, 1984, subcontract no. 4523010, Rockwell Science Center, May, 1984.

10. A. V. Virkar and R. S. Gordon, J. Amer. Ceram. Soc., vol. 60, no. 1-2, 58-61, (1977).

11. L. C. De Jonghe, A. Buechele and K. H. Yoon, Lawrence Laboratory Report

12. A. C. Buechele, L. C. De Jonghe and D. Hitchcock. J. Electrochem. soc., vol. 130, no. 5, 1042-9 (1983).

13. D. B. Marshall, T. Noma and A. G. Evans, J. Amer. Ceram. Soc., vol. 65, no. 10, C-174-C-176 (1982).

14. W. R. Parrish and J. Newman, J. Electrochem. soc., vol. 117, no. 1, 43-48 (1970).

15. A. C. Buchele and L. C. De Jonghe, Amer. Ceram. Soc. Bull., Vol. 58, No. 9, 861-4 (1979).

TECHNICAL INFORMATION DEPARTMENT
LAWRENCE BERKELEY LABORATORY
UNIVERSITY OF CALIFORNIA
BERKELEY, CALIFORNIA 94720